Defects, Thermal Phenomena and Design in Photonic Crystal Systems

by

David Lik Chin Chan
M.Phys. (Hons.) University of Oxford, United Kingdom (2001)

Submitted to the Department of Physics
in partial fulfillment of the requirements for the degree of

Doctor of Philosophy

at the

MASSACHUSETTS INSTITUTE OF TECHNOLOGY

September 2006

Author .....
Department of Physics
July 28, 2006

Certified by .....
John D. Joannopoulos
Francis Wright Davis Professor of Physics
Thesis Supervisor

Accepted by .....
Thomas J. Greytak
Associate Department Head for Education

Defects, Thermal Phenomena and Design in Photonic Crystal Systems

by

David Lik Chin Chan

M.Phys. (Hons.) University of Oxford, United Kingdom (2001)

Submitted to the Department of Physics
on July 28, 2006, in partial fulfillment of the
requirements for the degree of
Doctor of Philosophy

Abstract

The physics of blackbodies has been an ongoing source of fascination and scientific research for over a hundred years. Kirchhoff's law states that emissivity and absorptivity are equal for an object in thermal equilibrium. Coupled with the Second Law of Thermodynamics, one can show that no object can emit more than a blackbody at any given frequency, direction or polarization. While this provides a theoretical maximum to the intensity of thermal emission from an object, few come even close to the level of emission exhibited by a blackbody. Thus, there is much room for research into enhancing thermal radiation from many different types of materials.

The ability to modify or tailor the thermal emission profile of an object is of great importance and interest in many areas of applied physics and engineering. It turns out that thermal emission spectra can be changed by altering the geometry of the system or the materials used. For instance, nanoscale patterning can enhance emission at certain frequencies, while point defects can localize light at microcavities. General periodic electromagnetic structures, also known as photonic crystals, are therefore a natural medium in which to carry out such investigations, since they are metallodielectric systems that lend themselves relatively easily to sub-wavelength scale patterning and design.

This research program aims to study, through both theoretical and computational means, physical phenomena that drive thermal emission in photonic crystals and the design of point defects in the presence of fabrication constraints.

First, we explore point defect geometries in inverted opal photonic crystals that can be fabricated by colloidal self-assembly. We identify and study substitutional point defects that introduce a usable defect band into the photonic band gap. It is found that a silica sphere of radius between $0.33a$ and $0.35a$ (where a is the lattice constant) introduces a triply degenerate state into the band gap. Reflectance and local density of states calculations are performed to verify the existence and frequency of this defect. Such a defect can be used as a microcavity for localizing light at a point,

with a quality factor Q that is limited primarily by the proximity of the defect to the surface of the photonic crystal and other such defects.

Second, we present a useful framework within which we can understand some of the physical phenomena that drive thermal emission in one- and two-dimensionally periodic metallic photonic crystals, emphasizing phenomenology and physical intuition. We find that polarization and periodicity play key roles in determining the types of physical phenomena that can be excited in these systems. Promising structures in both 1D and 2D systems are identified as good candidates for thermal design. We discuss how the emissive properties of these systems can be tailored to our needs.

Third, we establish that the significant enhancement of thermal emission via Q-matching, which has been possible in 1D systems only, can be extended to 2D systems by means of Fano resonances in the 2D system. We demonstrate through detailed numerical and analytical studies that the Fano resonances characteristic of 2D-periodic photonic crystal slabs can be understood in terms of a 1D-model, thereby showing the existence of essentially 1D behavior in a 2D system. Moreover, we show how properties of these spectra can be controlled by changing the geometrical parameters of the photonic crystals. This work provides a path to the creation of graybodies that have tailored thermal emission spectra, with highly anomalous behavior.

Fourth, we perform direct thermal emission calculations for 2D- and 3D-periodic photonic crystal slabs using stochastic electrodynamics following the Langevin approach, implemented via an FDTD algorithm. We demonstrate that emissivity and absorptivity are equal, and thereby numerically verify Kirchhoff's law, by showing that such photonic crystal systems emit as much radiation as they absorb, for every frequency, up to statistical fluctuations. This has been an issue of great controversy because of experimental work indicating the violation of Kirchhoff's law. We also study the effect of surface termination on absorption and emission spectra from these systems.

Thesis Supervisor: John D. Joannopoulos
Title: Francis Wright Davis Professor of Physics

Acknowledgments

I remember an exchange I had with my parents at the age of six, when I was just about to begin primary school in Hong Kong. As I embarked on this new phase of my life, I wanted to know what lay ahead, so that I could have something to look forward to. They told me there was secondary school. A little deflated, I asked them what happened after that. They said, university. That sounded more interesting. I asked again, and got a response along the lines of 'a Masters degree' — whatever that was. Determined to get to the end of this seemingly interminable road, I persisted. 'After a Masters degree, you can do a doctorate, and then people will call you Dr. Chan.' By this time, I was quite excited, because being called Dr. Chan sounded really cool.

'What is a doctorate?' I asked, with burning curiosity.

My parents looked at me, smiled, and said, 'It's the highest academic degree the world has to offer.'

It was like the first glimpse of Everest. My life changed that very moment. I knew I would not rest until I had achieved that goal. The subject did not matter, neither did my career choice. All that mattered was to pursue that dream; everything else I could worry about later. There are people who see the Ph.D. as a means to an end, whether that end be a career in research, teaching or industry; for me, the Ph.D. was the end.

Thus began the long road that would eventually lead to my doctoral studies, and this thesis, some twenty years later. What I did not anticipate, and is the *raison d'être* of these acknowledgments, is that a Ph.D. is not an individual endeavour. None of this work would have been possible without the kind, generous and selfless help and support I received from many people.

First and foremost, I would like to thank my research advisor, Prof. John Joannopoulos, who has taught me far more than any individual I have encountered, save my parents. John is one of the most intelligent and charismatic people I know, and possesses the wonderful qualities of integrity, diligence and charm. He has been, and will continue to be, my professional and personal example. John does nothing half-

heartedly; every challenge and responsibility he takes upon himself he will execute with the utmost dedication, flair and attention to detail. As a result, he is the best scientist, teacher and mentor I have come across.

Yet his talents do not end here. He is a gifted manager of both time and people; the first to foster efficiency and productivity, and the second to promote harmony and collaboration within the research group. In the words of Dr. Oscar Alerhand, a former member of the group, 'John could run Goldman Sachs and Morgan Stanley in the morning, and still have time to do research in the afternoon!'

I am grateful to John for his help with practical matters also. He gave me interesting and challenging projects to work on, helped me get unstuck countless times, taught me the difference between apples and oranges, and gave me great leeway in pursuing other interests and commitments outside academics. (In the last five years, I took up sailing, swimming, skiing, figure skating, tennis, golf, singing, ballroom dancing, and to top it all off, I ran a marathon.) I am particularly grateful to John for his understanding of my career choice, his indispensable help in my job search, and his glowing recommendations that have enabled me to be fellowship-funded these five years.

I would like to acknowledge my research collaborators, without whose help none of this work would have been possible. It has been a great pleasure to work closely with Prof. Marin Soljačić, whose laid-back demeanour and good humour were particularly welcome during periods of frustration and lack of progress; thankfully, these periods were never long, because Marin, with his razor-sharp insight, would invariably put me on a new trajectory towards a solution. I also thank Prof. Steven Johnson, Dr. Elefterios Lidorikis and Ivan Celanovic for their help with many aspects of my research. I am grateful to Prof. Xiao-Gang Wen and Prof. Erich Ippen for serving on my thesis committee, and to the Kennedy Memorial Trust, MIT and the Croucher Foundation for providing me with fellowship funding.

It goes without saying that the graduate school experience is not one shaped by professors alone; my time at MIT has been enriched by the graduate students and post-docs I have interacted with. It has been a privilege to be part of John's research

group and to work with such brilliant colleagues; I can't think of any one in the group to whom I have not turned for help or just for a quick chat. In the midst of the somewhat monastic life of a graduate student, one source of simple and daily social sustenance was to have lunch with my CMT peers who are now my good buddies: Peter Bermel, Michael Levin, Cody Nave and Bas Overbosch. The daily ritual of deciding on a lunch venue, going there together, and talking about anything and everything under the sun created a strong sense of camaraderie and we really became a support network for each other. In particular, I'd like to give special thanks to Peter for being such a patient and helpful officemate. He was always willing to drop whatever he was doing to help me with the myriad computational and research problems I ran into, and it was delightfully reassuring that a computer guru was never more than three feet away!

My acknowledgments would not be complete without mentioning my good friends Tyler VanderWeele, Chris Lee and Olumuyiwa Temitope Ogunnika, who have been with me through thick and thin during my time in Cambridge. They were always glad to lend a listening ear and would go out of their way to cheer me up when I was down. My gratitude goes also to the many friends I have made through the MIT Graduate Christian Fellowship and Park Street Church in Boston.

I will close by dedicating this thesis to my loving parents, Ming Lee Chan and Stella Chan, who have given up so much for me. In addition to showering me with love, attention and encouragement, and teaching me never to be complacent and to always strive for excellence in everything I do, they gave me the two most important things in life: a world class education and a living faith in the Lord Jesus Christ. I praise God for saving my physical and spiritual life, for giving me strength and endurance to get through five years of graduate school, for surrounding me with wonderful friends during my time in Boston, and for giving me a reason to live and Someone to live for. Soli Deo Gloria!

Contents

List of Figures

List of Tables

Chapter 1

Introduction

Ever since the discovery of an electromagnetic band gap in certain periodic dielectric structures[82] some twenty years ago, research into photonic band gap materials has taken off, creating a whole new subfield of physics. Lying at the intersection of solid state physics, materials science and electrical engineering, these fascinating materials are characterized by their possession of a photonic band gap, a range of frequencies in which light is forbidden from propagating. As such, these materials, also known as *photonic crystals*, can be thought of as the electromagnetic analogue of semiconductors, which possess electronic band gap regions where electrons are forbidden to propagate. If the semiconductor revolution, which forever changed the landscape of electronics research, is anything to go by, many believe that photonic crystals will usher in a similar revolution in the fields of optics, telecommunications and optical computing. Some believe it already has.

Prior to the advent of photonic crystals, a researcher in the field of optics had at her disposal a few important ideas from geometrical and wave optics, which were sufficient for most problems related to refraction, reflection, diffraction and interference[29]. In telecommunications, optical fibers were all the rage; they could trap light in a cylindrical tube and even bend it around a corner (though not too sharp a corner). Consequently, a fiber optic infrastructure has been built in many places around the world, carrying far more information with much lower losses than conventional electric coaxial cables.

Versatile as these fibers are, their operation is based on a very simple physical idea: total internal reflection. As such, they are limited in two ways. Total internal reflection occurs when the angle of incidence exceeds a critical angle; below this threshold, refraction occurs. A fiber, therefore, cannot be bent into too small a radius of curvature before the light in the inner core starts leaking out. The second problem arises from the design of optical fibers. Total internal reflection occurs when light from a high dielectric medium meets a low dielectric medium. It cannot occur the other way around. Thus, the light necessarily travels in a region of high dielectric, surrounded by a low dielectric cladding. It so happens that most materials have at least some absorptive losses, so that the high index core ends up absorbing a sizable fraction of the power over long distances, leaving a weakened signal at the other end. Furthermore, nonlinearities, which are present in most materials, put a limit on the maximum power that can be transmitted.

Both these problems can be avoided by using photonic crystals. A multilayer film can be wrapped into an omnidirectional waveguide with superior confinement (no critical angle). A one-dimensional line defect in a material with a complete photonic band gap can serve as a waveguide, also with no critical angle; if two such line defects meet to form a corner, a resonant cavity can be placed at that corner and tuned so as to promote 100% transmission and 0% reflection around the bend. All these configurations can be designed so that the light travels in a region of air surrounded by bulk material. Thus, photonic crystals can overcome the limitations associated with optical fibers by offering omnidirectional confinement and light transmission in an air core. Moreover, as an illustration of the power and versatility of photonic crystals, one can design a channel drop filter consisting of a resonant cavity connecting two parallel waveguides, such that an input signal in one waveguide can be passed to the output channel of the other waveguide with minimal losses.

We have extolled the virtues of photonic crystals in the realm of optical design, but their merits do not end here. Far more than being a better technology, photonic crystals embody a new *paradigm*, a fundamentally new way of thinking about electromagnetism in solid state systems. Because Maxwell's equations can be recast into the

form of a Hermitian eigenvalue problem involving vector differential operators (see section 1.2), we can plot dispersion curves, or bandstructure, for these systems, which give us great insight into the eigenmodes allowed by the system. What was previously understood as total internal reflection above a critical angle of incidence can, in the new paradigm, be understood as a region in $\omega - \mathbf{k}$ space that permits guided modes to propagate. This new way of thinking has much in common with semiconductor physics; in fact, an extensive analogy may be drawn between the three-dimensional scalar eigenvalue problem in semiconductor physics and the three-dimensional vector eigenvalue problem in solid state electromagnetism.

Computational calculations for such systems are of great importance because they can serve as a pre-laboratory where novel geometries and structures can be tested and refined. One can have faith in relatively accurate correspondence between calculation and experiment because Maxwell's equations are essentially exact in the linear regime of low photon-photon coupling, the regime in which photonic crystals are used. Reverting to the analogy with semiconductor physics, we expect computational calculations for photonic crystals to be *more* accurate than those for semiconductors, because electron-electron coupling is stronger in semiconductors than photon-photon coupling is in photonic crystals. As a result, bandstructure calculations and time-domain simulations have become indispensable tools in driving the field forward. In fact, these tools have become so standardized that they are freely and widely available to researchers in the field (e.g. MIT Photonic Bands).

1.1 Overview of this work

The goal of the present research is to shed light on a few important questions in the field of photonic crystal research today, namely,

1. How do fabrication constraints affect the design of defects in photonic crystals?

2. How can photonic crystals be used to modify and enhance thermal radiation?

3. Does Kirchhoff's law hold for a general photonic crystal, given recent contro-

versial experiments that suggest the contrary?

With regard to the first question, recently, there has been much interest in fabricating photonic crystals by means of colloidal self-assembly. Such a method is attractive because it offers a simpler and cheaper way of making three-dimensionally periodic photonic crystals, compared with conventional semiconductor nanofabrication techniques, which, while being more precise, are significantly more expensive. However, the lower cost of manufacture comes with trade-offs. There is the problem of disorder and structural defects in the photonic crystal, which plague many such methods of self-assembly. This is especially important since disorder can destroy the photonic band gap in such materials. But even if we were to set aside this problem as an essentially experimental one, we would run into another, more theoretical, constraint: that put on the *design* of the photonic crystal by the method of fabrication itself. For instance, Vlasov *et al.*[76] use a method of colloidal self-assembly that requires etching out self-assembled silica spheres in order to produce air gaps inside a background of silicon. However, the method of wet-etching necessitates a connected structure of silica spheres through which the wet-etching agent can permeate. Given the utility of point defects as microcavities for localizing light (we will discuss this further later in this chapter), there is, therefore, a need to identify a class of point defects that can be made using this method. This was the motivation for the work described in chapter 2.

The second question concerning the modification and enhancement of thermal radiation has been around for well over a century now. Ever since Planck[59], the physics of blackbodies has been a source of fascination and scientific research; properties of their thermal emission provided one of the most important clues for the discovery of quantum mechanics. Kirchhoff's law states that emissivity and absorptivity are equal in thermal equilibrium. Coupled with the Second Law of Thermodynamics, it is possible to show that no object can emit more than a blackbody at any given frequency, direction or polarization. While this provides a theoretical maximum to the intensity of thermal emission from an object, few come even close to the level of emission exhibited by a blackbody. In fact, uniform slabs of material are found to

be relatively poor emitters. Thus, there is much room for research into enhancing thermal radiation from many different types of materials.

The ability to modify or tailor the thermal emission profile of an object is of great importance and interest in many areas of applied physics and engineering. It turns out that thermal emission spectra can be changed by altering the geometry of the system or the materials used. Photonic crystals are therefore a natural medium in which to carry out such investigations, since they are metallodielectric systems that lend themselves relatively easily to sub-wavelength scale patterning and design. In light of this, a clear and physically intuitive understanding of the mechanisms that drive thermal emission in such systems is of great value in guiding thermal design.

Because of important inherent differences between one-dimensional (1D), two-dimensional (2D) and three-dimensional (3D) periodicity in photonic crystals, it is best to analyze crystals of different dimensionality separately. We focus on some of the most important physical phenomena that drive thermal emission. We do this with the intention of developing physical intuition and understanding of features of emission spectra. Once we have this intuitive understanding, we show how one can tailor the thermal emission properties of these structures to achieve one's design needs. We do this for both 1D- and 2D-periodic metallic photonic crystal slabs, covering a multitude of physical phenomena, including waveguide cut-offs, waveguide resonances, surface plasmons, slab resonances and diffraction peaks.

From the literature, it is clear that the idea of matching the radiative Q-factor of a system with its absorptive Q-factor in order to enhance emission is fundamentally a one-dimensional one. It is reducible to the problem of having one input channel, a resonant cavity, and one output channel. In such a setup, light emitted by the resonant cavity and the incident light interfere in such a way as to extremize the net outgoing wave. This complete cancellation of waves from the cavity and the incident/outgoing beam is unique to the one-dimensional world. However, it turns out that enhancement of thermal emission via Q-matching, which is usually observed in 1D systems only, can be extended to 2D systems by coupling into Fano resonances[19] in the 2D system. In other words, we demonstrate the existence of essentially 1D behavior in a 2D

system — a case of reduced dimensionality. We show through detailed numerical and analytical studies that the Fano resonances characteristic of 2D-periodic photonic crystal slabs can be understood in terms of a 1D-model based on Q-matching.

The third and final question we asked concerns the validity of Kirchhoff's law when applied to a general photonic crystal structure. This was originally proven analytically for a 1D uniform slab. One may well wonder whether such a law, which makes sense intuitively given the principle of detailed balance, holds for the more general case of a photonic crystal. But the question took on a new relevance in 2003, when intriguing experiments by Lin *et al.*[45, 42] seemed to indicate that the thermal radiation from metallic photonic crystals might even exceed that of a blackbody in free space. The possibility of thermal nonequilibrium during the measurement process has been acknowledged[46]. The controversy was partly addressed by Luo *et al.*[48], who performed a direct emission calculation for a 2D-periodic array of circular rods, and showed that thermal emissivity was equal to absorptivity, apart from statistical fluctuations. However, Lin's work was done on 3D-periodic photonic crystal structures. In the final part of this thesis, we extend the work of Luo *et al.* by applying the same methodology of stochastic electrodynamics to two fully 3D-periodic photonic crystal structures: a woodpile[74] (similar to that studied by Lin *et al.*) and a diamond metallodielectric structure[20]. We also consider the role of surface termination in determining the emission spectrum of a woodpile structure. As a bonus, we find that certain 3D-periodic structures have much higher thermal emission compared with a uniform slab; these high-emission structures should be very useful in thermophotovoltaic and incandescent lighting applications, where luminous efficiency is paramount.

The outline of the thesis is as follows: the rest of this chapter describes the basic physics of photonic crystals and introduces important ideas that will come up later in this work. Chapter 2 investigates point defect geometries in inverted opal photonic crystals fabricated by colloidal self-assembly. In Chapters 3 and 4, we study thermal emission and design in 1D- and 2D-periodic metallic photonic crystal slabs, respectively. Chapter 5 applies a 1D-model of thermal emission enhancement based

on Q-matching to Fano resonances in a 2D-periodic system, with intriguing results. In Chapter 6, we present a direct calculation of thermal emission in 3D-periodic photonic crystals, using the methodology of stochastic electrodynamics previously developed by Luo *et al.*[48], and demonstrate the validity of Kirchhoff's law in 3D-periodic photonic crystals. Finally, in Chapter 7, we summarize the important ideas of this thesis, and conclude our exposition.

1.2 A Whirlwind Tour of Photonic Crystals

The laws of classical electromagnetism were first presented to the Royal Society in London by James Clerk Maxwell in 1864. These four equations governed the behavior of electric and magnetic fields and their interactions with materials. As long as materials could be modeled by their dielectric permittivity (ϵ) and magnetic permeability (μ), one could, in theory, work out the electric and magnetic fields generated by the system for a given set of boundary conditions. These coupled three-dimensional vector differential equations were not trivial to solve in general. Nonetheless, the description of electromagnetism in the form of a classical field theory was complete.

In the early twentieth century, quantum mechanics was being developed, and one of the most important mathematical frameworks being used in that field was that of the eigenvalue problem. The time-independent Schrödinger equation, which governs the behavior of a particle of mass m moving in a potential well $V(\mathbf{r})$, can be written

$$H\Psi_i(\mathbf{r}) = E_i\Psi_i(\mathbf{r})$$

where $H = -\frac{\hbar^2}{2m}\nabla^2 + V(\mathbf{r})$ is the Hamiltonian (a scalar differential operator), $\Psi_i(\mathbf{r})$ is the wavefunction (a complex scalar field), and E_i is the energy eigenvalue (a real scalar). The wavefunction $\Psi_i(\mathbf{r})$, when operated on by the Hamiltonian H, is simply the wavefunction itself multiplied by a constant E_i. There are generally many solutions (labeled by i) to this eigenvalue equation, each of which has an *eigenfunction* $\Psi_i(\mathbf{r})$ and an *eigenvalue* E_i. Because H is Hermitian ($\int \phi^* H\psi dV = \int (H\phi)^*\psi dV$),

the eigenvalues E_i are all real, and the eigenfunctions $\Psi_i(\mathbf{r})$ are mutually orthogonal.

It turns out that Maxwell's equations can be combined in such a way as to take the form of a Hermitian eigenvalue equation. The magnetic field $\mathbf{H}$ at position $\mathbf{r}$ is given by

$$\Theta \mathbf{H}_i(\mathbf{r}) = \left(\frac{\omega_i}{c}\right)^2 \mathbf{H}_i(\mathbf{r})$$

where $\Theta = \nabla \times \frac{1}{\epsilon(\mathbf{r})} \nabla \times$ is a real vector differential operator, ω_i is the frequency eigenvalue, and c is the speed of light. The similarity is obvious between the electromagnetic eigenvalue problem and the quantum mechanical eigenvalue problem. It turns out the Θ, as defined above, is a Hermitian operator, so we can expect the eigenvalues ω_i to be real and the eigenfunctions $\mathbf{H}_i(\mathbf{r})$ to be orthogonal. Because of the similarities between quantum mechanics and electromagnetism, many of the ideas and theorems from the former field, such as Bloch's theorem for periodic potentials and bandstructure calculations, may be applied to the latter.

In their most general form, photonic crystals are periodic structures made of metal or dielectric. This periodicity may be in one, two or three dimensions. It is fair to say that photonic crystals create the electromagnetic equivalent of the periodic electronic potentials one sees so often in solid state physics. Out of these periodic potentials arise electronic (photonic) band gaps, which are ranges of energy (frequency) in which electrons (photons) are forbidden from propagating. One interesting feature of electromagnetism in dielectric media is that there is no fundamental length scale, unlike Schrödinger's equation, for which the natural length scale is the Bohr radius. Therefore, it is possible to take an existing solution for a particular photonic crystal system, and scale it up or down in physical size and frequency. It is also possible to take advantage of mirror plane symmetry in photonic crystal systems and separate the eigenmodes into transverse magnetic (TM) and transverse electric (TE) modes.

What makes photonic crystals truly versatile as building blocks for optical systems is the possibility of introducing deliberately designed defects. A point defect can localize light at a point; a line defect can be used as a waveguide. The basic principle is the same: light of a particular frequency is forbidden from propagating in the

surrounding bulk material because of the photonic band gap that exists in the bulk; as a result, the light is confined to the region of the defect, where a defect mode exists. Furthermore, just as one can suppress absorption of light by using a band gap, so one can suppress emission of light by the same method. The ideas and tools that are available for designing absorption are equally applicable to thermal emission, because of Kirchhoff's law. There is, therefore, much room for creativity and research in using photonic crystals to tailor thermal emission to one's needs, and indeed, it is with this topic that the greater part of this thesis will be concerned.

Chapter 2

Point defect geometries in inverted opal photonic crystals

In this chapter, we study point defect geometries in inverted opal photonic crystals that can be easily fabricated by means of colloidal self-assembly. Two broad classes of defects are considered: substitutional and interstitial. Substitutional point defects are found to introduce a usable defect band into the photonic band gap. This can be done by using a silica sphere of radius between $0.33a$ and $0.35a$ (where a is the lattice constant). The state is triply degenerate. Reflectance and local density of states calculations are performed to verify the existence and frequency of this defect. The point defect can be made by pre-coating shrunk silica spheres with a thin layer of silicon. Such a defect can be used as a microcavity for localizing light at a point, with a quality factor Q that is limited primarily by the proximity of the defect to the surface of the photonic crystal and other such defects.

2.1 Introduction

Recently, there has been much interest in fabricating photonic crystals by means of colloidal self-assembly[32, 76, 30, 77, 57, 65, 8, 47]. Such a method is attractive because it offers a simpler and cheaper way of making three-dimensionally periodic photonic crystals, compared with conventional semiconductor nanofabrication tech-

niques. Work has been done to show that self-organizing systems that self-assemble into large-scale photonic crystals can have photonic band gaps (PBGs) or pseudo-gaps in the near-visible frequency regime[9, 6, 67, 4, 78, 85, 49, 60, 33, 37, 34, 71, 40]. Natural assembly of colloidal microspheres yields irregular, polycrystalline photonic crystals with many structural defects that can destroy the PBG. However, it turns out that strong capillary forces at a meniscus between a substrate and a colloidal sol can induce crystallization of spheres into a 3D array of controllable thickness. Sweeping this meniscus slowly across a vertically placed substrate by solvent evaporation leads to the deposition of thin planar opals. This technique has been used by Vlasov *et al.*[76] to produce inverted opal photonic crystals with bandgaps at around 1.3 μm.

Deliberately designed defects are desirable features in photonic crystals[62, 27]. A point defect, for example, with a mode localized within a complete PBG would give rise to a microcavity, while a line defect can be used as a waveguide[32, 35]. Microcavities and waveguides can be used as building blocks for optical devices and all-optical integrated circuits. There is, therefore, a need to design defects that can exist in the gap and be easily introduced into the bulk structure. Since colloidal self-assembly appears to be a promising and economical way of fabricating photonic crystals, we would like to identify a class of point defects that can be made using this method. This was the motivation for the work described in this chapter. Computational calculations for such systems are of great importance because they can serve as a pre-laboratory where novel ideas of possible defect geometries are tested and refined. One can have faith in relatively accurate correspondence between calculation and experiment, since Maxwell's equations are essentially exact in the linear regime of low photon-photon coupling, the regime in which such crystals are used.

2.2 Point defect geometries

We consider an inverted opal structure, which is a face-centered cubic lattice of air spheres in a silicon background. Such a structure can be thought of as the *inverse* of the more familiar f.c.c. crystal of silicon spheres in air. Experimentally, synthetic

opals can be made by colloidal crystallization of an f.c.c. lattice of silica spheres, backfilling interstitial spaces with silicon, and then wet-etching out the silica spheres, leaving air spheres behind. However, the infiltration of the background with silicon is usually imperfect, leaving some air gaps in between the silica spheres. We take this imperfection into account in our simulations by building up the structure using air spheres with a $0.06a$ (where a is the lattice constant of the f.c.c. lattice; in all that follows, length scales will be given in units of a) coating of silicon, which leaves air gaps in the diagonal spaces between spheres. In the structure under study, the air spheres have a radius of $0.354a$, so the silicon coating is about 17% of the radius of the air spheres. The air spheres are overlapping because the critical radius for the overlap of spheres in f.c.c. crystals is $a/(2\sqrt{2}) = 0.354a$. We terminate the surface using a plane that cuts the spheres in half, because this appears to be more similar to what is produced in experiments by Vlasov *et al.*

In general, one can create a defect by adding or removing dielectric. The former method produces a *dielectric* defect while the latter gives an *air* defect[31]. Both are effective ways of introducing defects to a photonic crystal system, though there are connectivity issues that make the two methods different, depending on whether the crystal itself is dielectric- or air-connected (or both). It should also be noted that the orientation of the crystal can affect the reflectance measurements. It turns out that, for inverted opals, samples of higher quality can be obtained with surfaces normal to the [111] direction than the [100] direction. For this reason, most of our work involves studying crystals with [111] surface orientation. Furthermore, in experimental measurements, the wafer was placed on top of a silicon substrate. It was thought that the presence of the substrate could have a non-trivial effect on reflectance measurements. However, having performed calculations with and without the substrate, we find no significant differences.

Fig. 2-1 shows the two different defect geometries that we considered. An interstitial defect is designed to fit into the spaces between the larger spheres. A substitutional defect replaces an existing sphere.

In the interstitial case, it is necessary that these interstitial spheres be sufficiently

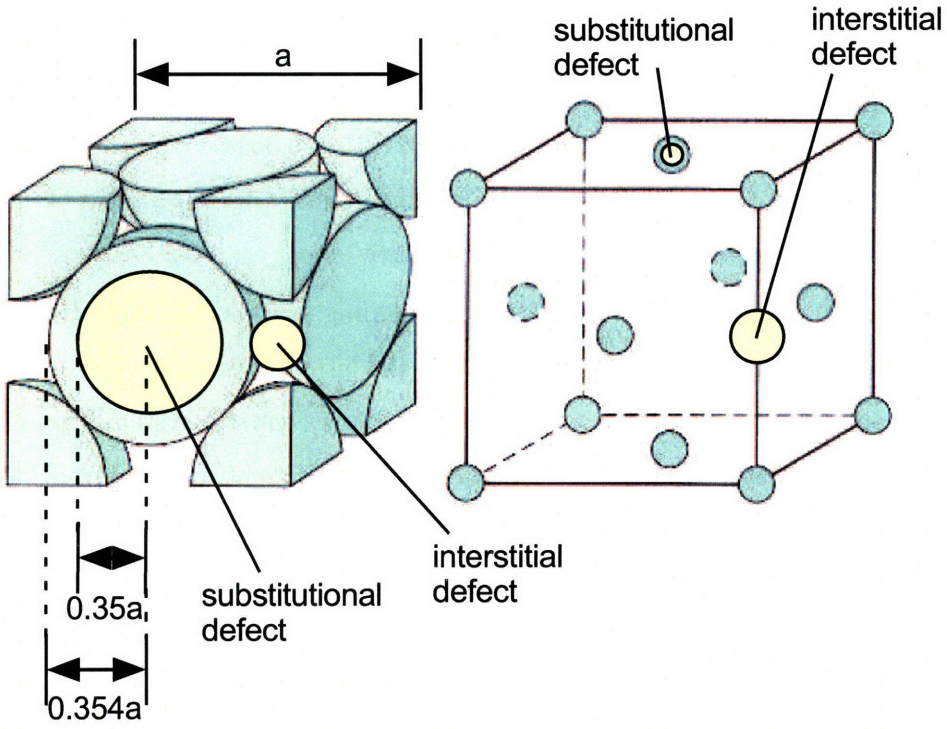

Figure 2-1: (Color) Two different styles of point defects (adapted from [10]).

small; otherwise, their presence in the colloidal self-assembly process would disrupt the structure of the rest of the crystal. The upper bound on the radius of the small sphere is $\frac{1}{2}(1-\frac{1}{\sqrt{2}})a \approx 0.146a$. Single interstitial air and dielectric defects can be implemented by having small silica or silicon spheres, and were tried in our calculations. We also considered clumps of 7 or 8 such air and dielectric defects. The presence of interstitial air defects changes the connectivity of the system, since new air channels have been created joining non-adjacent large air spheres. Interstitial dielectric spheres, however, only affect the system insofar as they fill in the 'holes' that were not completely backfilled with silicon. In any case, our results for these interstitial defect geometries revealed no particularly useful change in the bandstructure of these systems that could lead to the existence of a defect band in the gap. The change tended to either pull down some states from the upper bands into the gap, but only for certain wave vectors, or it destroyed the photonic band gap altogether. In the remainder of this chapter, we will restrict our attention to substitutional defects.

In the substitutional case, the outer radius must lie between $0.146a$ and $0.354a$: if less than the former, then the sphere will slide into an interstitial space; if greater than the latter, it will disrupt the packing of the structure. A relatively easy modification would be to reduce the size of the silica spheres used to create the structure. Note, however, that if the radius of the silica spheres is decreased below $0.354a$, the defect sphere will no longer be touching adjacent, normal spheres. This means that after backfilling, the defect sphere will be completely enclosed by silicon, and the silica material inside will *not* be etched away by the wet-etching process. We have effectively created a defect sphere with silica ($\epsilon = 2.1025$) inside instead of air, amounting to a dielectric substitutional defect. We study this class of defects for different radii of silica spheres, and identify some useful properties.

2.3 Characteristics of the defect state

To determine the properties of a photonic crystal structure, it is important to be able to calculate its bandstructure and reflectance spectrum, since the first tells us about

the modes the structure supports, and the second allows us to make direct comparison with experimental results. We calculate bandstructure using the MIT Photonic Bands (MPB) program, which uses a variational method to solve the Maxwell eigenvalue equation[35]. For reflectance, we perform a time domain simulation of the fields using a finite difference technique. Note that in both our frequency and time domain calculations, we did not allow frequency to go above 1.0 (in units of c/a) because we did not wish to concern ourselves with diffraction. By working with frequencies below 1.0, a normally incident light wave would produce a transmitted wave that is also normal. For frequencies above 1.0, several diffracted beams are possible, corresponding to different wave vectors, which are conserved by the scattering of the photonic crystal only up to a reciprocal lattice vector. Thus, we have reduced the problem to a one-dimensional one. Such a simplification is acceptable, given that the experimental measurements of Vlasov *et al.* were mostly at 1.0 or below.

Fig. 2-2 shows the bandstructure of a system with a shrunk silica sphere of radius $0.35a$. The bands for the bulk structure were calculated using a basis set ranging from (8,8,8) to (256,256,256), and (16,16,16) was found to be effectively converged. The defect band was calculated by introducing the defect into the system and performing the calculation with a 3x3x3 supercell and a basis set of (48,48,48). A supercell calculation was required in this case because the presence of the defect *reduced* the periodicity of the structure, and resulted in an *increase* of the size of the repeating cell. Ideally, we would use an isolated defect in an otherwise periodic crystal, but it turns out that having a periodic system simplifies the calculations enormously, as it allows us to impose periodic boundary conditions and apply Bloch's theorem. The choice of the size of the supercell involves striking a balance between preventing excessive coupling between defects in adjacent supercells (this is equivalent to requiring a high Q cavity), and computation time. The first consideration leads us to increase the size of the supercell while the second leads us to decrease it. It was found that 3x3x3 gave good results for bandstructure calculations without incurring unacceptably long computation times. We see from the figure that the presence of the defect pulled down some of the upper bands to the middle of the gap while maintaining the overall

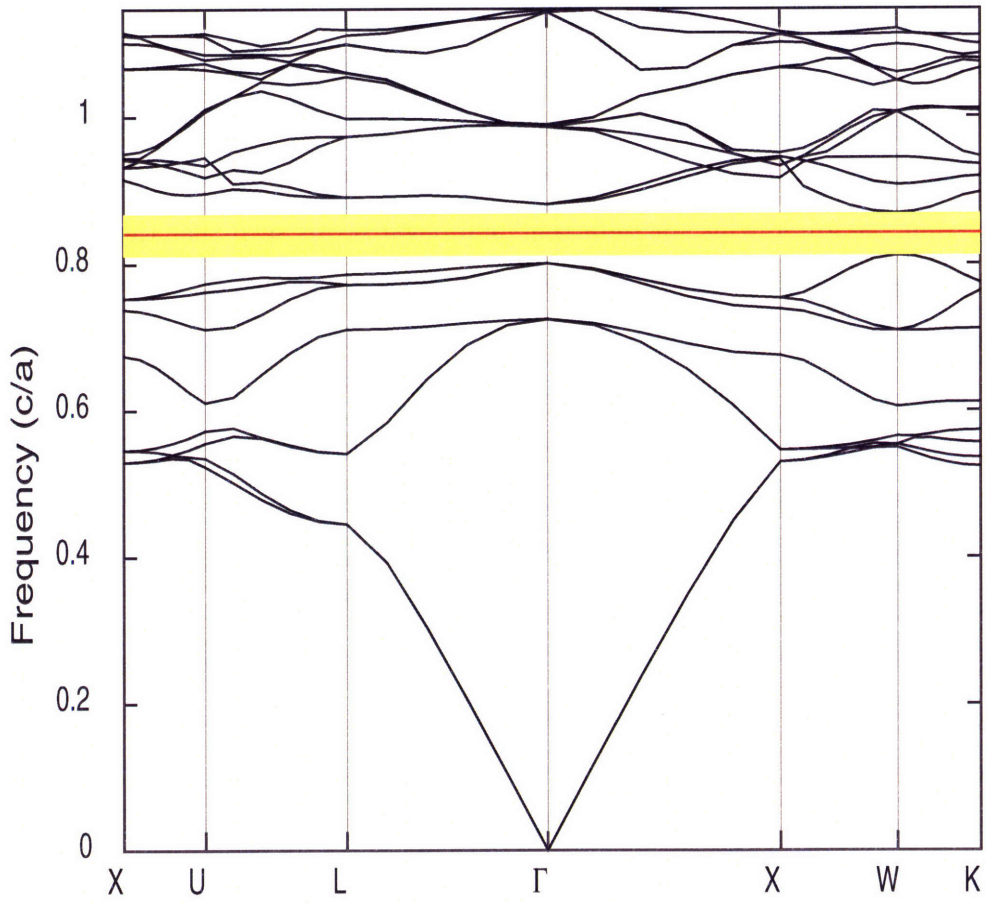

Figure 2-2: (Color) Bandstructure of photonic crystal with point defect mode. Defect calculation performed with 3x3x3 supercell, with a (48,48,48) basis set, for shrunk silica sphere radius of 0.35a. The 3x3x3 supercell calculation for the defect produced bandstructure with multiple folding of bands, and as such the band diagram for that calculation is not edifying to show. The most important result from that calculation, namely, the defect state frequency, was extracted, and this piece of information was incorporated into the above non-supercell bandstructure.

integrity of the PBG. This geometry has the desirable features that we look for.

We also performed bandstructure calculations for shrunk silica spheres of different radii. We examined a series of defect radii from $0.15a$ to $0.35a$. Each one of these defect radii produces a change in the bandstructure of the system. The defect pulls down some states from above the gap. The larger the radius, the further into the gap the states are pulled. Since we are interested in the local confinement of light, and such confinement requires the existence of defect bands within an otherwise forbidden region, we are looking for radii that pull down states such that they are in or near the middle of the gap with forbidden regions on either side. It turns out that such a defect state can be produced with defect radii between $0.33a$ and $0.35a$. Obviously, the smaller the radius, the greater the overall increase in dielectric constant. In general, the frequency of the defect mode decreases as the average dielectric constant of the defect is increased; this is the qualitative dependence of defect frequency with dielectric constant. We show $0.35a$, which is the defect mode that is most easily distinguished from the surrounding background of states. We did a careful counting of the number of defect bands pulled down by the defect into the gap, and it turns out to be three. Thus, the defect state is triply degenerate. (Such a result is certainly consistent given the cubic symmetry of the lattice.) The symmetry of the defect structure allows for a three-fold degenerate irreducible representation, which in turn leads to a three-fold degenerate state.

As an aside, it is useful to observe that the adequacy of a particular size of supercell for the calculation at hand can be determined from the flatness of the defect band. A point defect has complete directional symmetry and its mode must therefore be independent of wave vector. This corresponds to a flat band in $\omega - k$ space. If the supercell is insufficiently large, the defects would be interacting (in a tight-binding sense), and such interaction would produce a network of interlinked defects, favoring the $\{100\}$, or cubic, directions. In other words, the band would not be flat. We were able to have confidence in the frequency of the defect band to the extent that the bands obtained in our 3x3x3 supercell calculations were acceptably flat.

Fig. 2-3 gives the reflectance spectrum for the system with and without the defect.

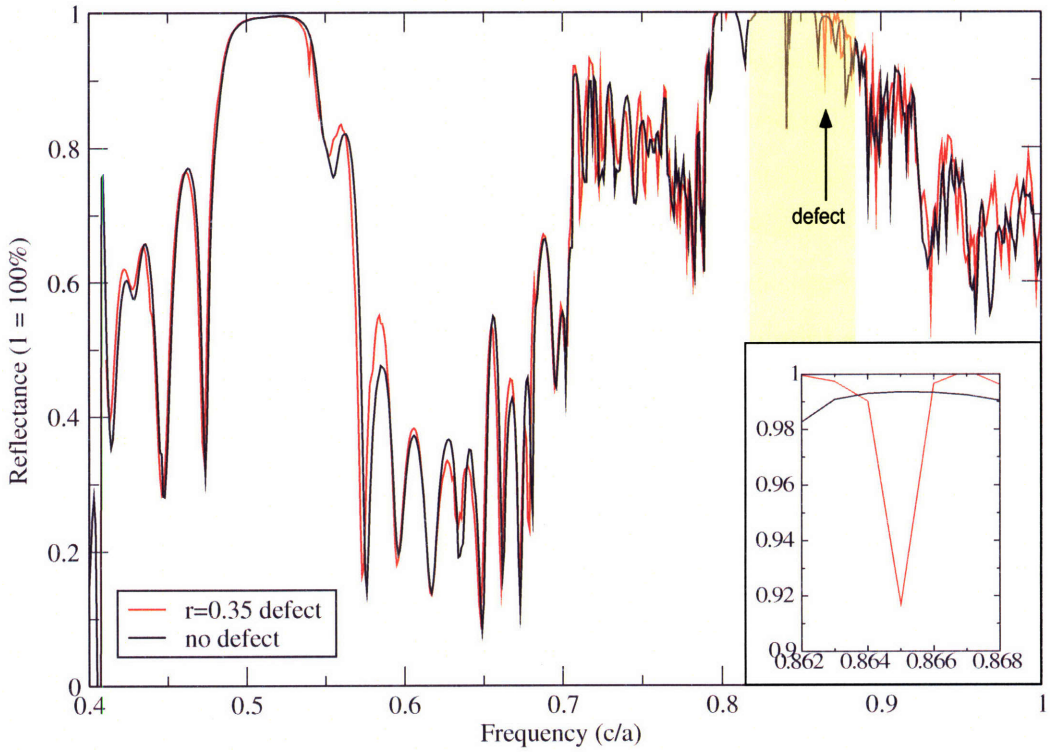

Figure 2-3: (Color) Reflectance spectrum of photonic crystal, with and without point defect. The dipole source is polarized in the [110] direction. The computational cell used had dimensions of 56x97x411 grid points, corresponding to 40 grid points per lattice constant. The photonic crystal slab was seated on a silicon substrate. A 2x2 supercell was used, and the simulation was run for 79,195 time steps. [Inset shows magnified version of reflectance dip due to defect.]

The computational cell chosen was a long one, with dimensions 56x97x411 grid points, corresponding to about 40 grid points per lattice constant a. The photonic crystal slab was in the middle, and flux planes were placed on either side of it at distances of $1.5a$ and $4a$. The slab was nine spheres thick, seated on a silicon substrate, and the surface was normal to the [111] direction. This was also a supercell calculation, though in this case, we used a 2x2 supercell because we wanted to produce a wider band and stronger coupling of the incident radiation with the defect mode. In these computational experiments, a dipole source was used instead of a Gaussian plane wave, as the former contains many different wave vectors while the latter contains only one (that which corresponds to normal incidence), and we want the incident radiation to couple into the defect mode, irrespective of its symmetry. The simulation was run for a total of 79,195 time steps. This was chosen to be sufficiently large to ensure that the Gaussian pulse had sufficient time to propagate through the entire system. The reflectance was calculated by the following equation, which comes from dividing the magnitude of the reflected flux ($|\mathbf{E}^{\mathbf{slab}} - \mathbf{E}^{\mathbf{vac}}|^2$) by the magnitude of the incident flux ($|\mathbf{E}^{\mathbf{vac}}|^2$):

$$R = \frac{|E_x^{slab} - E_x^{vac}|^2 + |E_y^{slab} - E_y^{vac}|^2 + |E_z^{slab} - E_z^{vac}|^2}{|E_x^{vac}|^2 + |E_y^{vac}|^2 + |E_z^{vac}|^2}$$

Note that all fields are functions of frequency, for a given point in space, as we take the Fourier transform of the time series of fields in real time. A discrete Fourier transform was performed on the entire time series, and no averaging was required. We take the absolute values because the fields are complex quantities in general. We run the simulation once with the slab in place, and then again with vacuum only, and the difference in fields between the first run and the second run, when expressed as a fraction of the intensities in the vacuum case, gives the reflectance. For normally incident radiation, one only needs to record the fields at one monitor point situated between the source plane and the slab, but for a dipole source, integration over a flux plane is required since the fields are different in different directions. That is what we did to obtain Fig. 2-3.

One can see good agreement between the black curve (no defect) and the red curve (defect) at almost all frequencies. To find the effect of the point defect, we focus our attention on the region of the photonic band gap. This is a region where we expect near 100% reflectance, since there are no propagating modes within the slab for that range of frequencies, and the slab is thick enough to prevent tunnelling of evanescent waves. It is encouraging to see the reflectance dip caused by the point defect, which has been highlighted along with the band gap region. The position of the dip agrees with the frequency of the defect state predicted by the bandstructure calculations. We stress that the bandstructure and reflectance spectrum are two different calculations, and that the agreement between the two on the frequency of the defect mode is a strong indication of the reliability of our results.

The introduction of a defect causes a redistribution of the local density of states (LDOS) of the system, with the total number of states being conserved. The defect takes a few states from outside the gap and puts them inside the gap. This change is localized in space but not in frequency. Integrating the LDOS over all volume (including the defect) gives the global density of states. If the total number of states in the system is N, then the effect of the defect is to put a state of weight ~ 1 in the gap and reduce the DOS outside the gap by $\sim 1/N$. Transmission as a function of frequency is proportional to the global density of states. In a structure of infinite extent, $N \to \infty$ and the change in DOS outside the gap tends to zero. However, in such a limit, the defect state becomes unobservable because $1 \ll N$. Thus, a compromise is needed to keep the disturbance to states outside the gap small while allowing the localized state to have an observable effect on the spectrum inside the gap. This is also the reason why it is impossible to observe the defect mode in a reflectance spectrum without collateral change to the spectrum outside the gap (though the relative magnitudes of these changes are in the ratio $1 : \frac{1}{N}$).

We recognize also that there are a few reflectance dips *within* the photonic band gap that appear to be states inside the gap. On closer examination, however, one can see that the black and red curves overlap completely for these 'states'. What this means is that the dips are present irrespective of the existence of the defect.

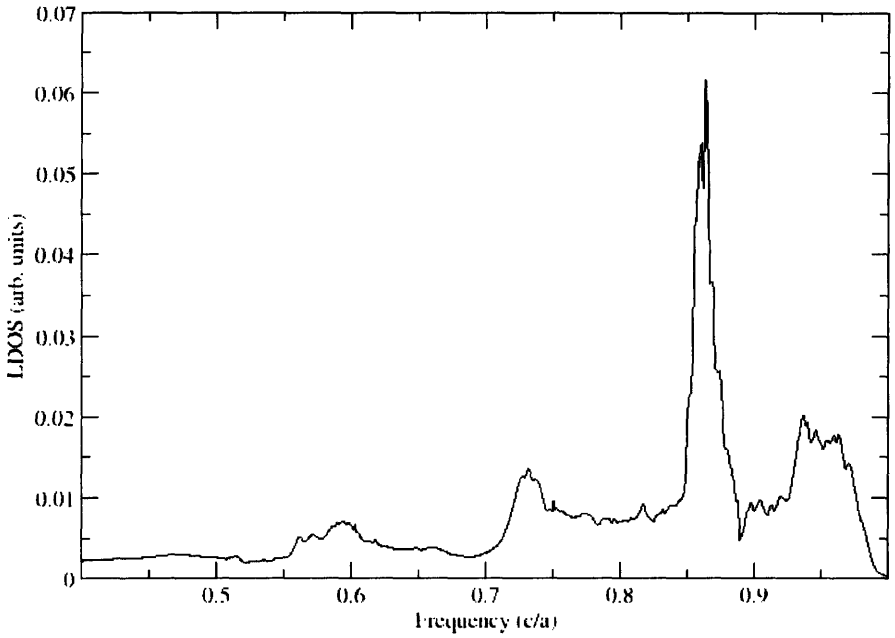

Figure 2-4: Local density of states of photonic crystal, with point defect. We followed the Gilat-Raubenheimer method, using 8 evenly spaced k-points in the irreducible Brillouin zone.

We understand these to be resonant transmission peaks caused by the finite size of the photonic crystal slab that we used in our calculations. Therefore, they are *not* localized states.

We also point out that while a dipole source contains many wave vectors, in practice, because of the long computational cell and the distance between the source and the slab, the light that reaches the slab is not too far from being normally incident. As a result, the light hits the slab with a wave vector close to the Γ-L direction (111). The bandstructure calculation (Fig. 2-2) exhibits a partial gap in the Γ-L direction between 0.45 and 0.55, and we see this showing up in the reflectance spectrum in the form of a region of high reflectance between 0.48 and 0.55. The range of frequencies do not correspond exactly because the incidence is only approximately normal. Similarly, we see a region of high (but not unity) reflectance between 0.7 and 0.77, corresponding to the partial Γ-L gap in that range.

To obtain even more definite evidence of the existence and frequency of the defect state, we performed calculations of the local density of states of the photonic crystal system, and these results are presented in Fig. 2-4. The local density of states of a system is defined by

$$D(\omega, \mathbf{r}) = \sum_{n\mathbf{k}} |E_{n\mathbf{k}}(\mathbf{r})|^2 \delta(\omega - \omega_{n\mathbf{k}})$$

such that

$$D(\omega) = \int D(\omega, \mathbf{r}) d^3\mathbf{r} = \sum_{n\mathbf{k}} \int |E_{n\mathbf{k}}(\mathbf{r})|^2 \delta(\omega - \omega_{n\mathbf{k}}) d^3\mathbf{r} = \sum_{n\mathbf{k}} \delta(\omega - \omega_{n\mathbf{k}})$$

where $D(\omega)$ is the *global* density of states, and $E_{n\mathbf{k}}(\mathbf{r})$ is assumed to be normalized to unity over all space. We see that integrating the local density of states over all space gives the global density of states, as required.

Such a calculation can be done numerically by integrating over 'shells' of constant energy in k-space[36, 3]:

$$D(\omega, \mathbf{r}) = 2\frac{V}{(2\pi)^3} \int \frac{dS_\omega}{v_g}$$

where $v_g = |\nabla_{\mathbf{k}} \omega(\mathbf{k})|$, the magnitude of the group velocity, and the integral is performed over a surface of constant energy $\omega(\mathbf{k})$. The extra factor of 2 accounts for the two transverse polarizations of light. The local density of states can be thought of as the probability of finding a photon with frequency ω at point $\mathbf{r}$, irrespective of wave vector or band number (these are summed over). We choose to calculate the local density of states for a point near the center of the defect sphere, with the physical understanding that if a defect mode exists, it should have a mode profile that has a high concentration of photons within the defect sphere. We therefore expect a peak at around $0.86c/a$ in the LDOS spectrum. Numerically, we follow the Gilat-Raubenheimer method[24, 63] of dividing up the irreducible Brillouin zone into a cubic mesh and approximating the constant energy surface with parallel planes. We use 8 evenly spaced k-points in the irreducible Brillouin zone. Another way of doing it would be to use a special k-points scheme[52].

Our local density of states calculation exhibits a very distinct peak at about

$0.86c/a$, showing clearly the existence of the defect mode. The LDOS is low for frequencies on either side of the peak because of the photonic band gap. However, it is not zero because our LDOS calculation was performed on a slab rather than an infinite structure. The bandstructure calculation was done on an infinite crystal and so it had a real gap. A slab, on the other hand, only has a pseudogap, and so we see some states inside the pseudogap region. (Incidentally, we chose to do the calculation for a slab because that is what can be made and observed experimentally.) Therefore, we do not expect zero LDOS in the 'gap' region. The frequency of the peak agrees well with our bandstructure predictions and reflectance calculations. There are interesting peaks on either side of the main defect peak. They show that the defect produces resonant structure beyond the gap. These resonant structures are more noticeable with a finite slab than an infinite one in which the resonances wash out.

2.4 Conclusion

In this chapter, we studied possible point defect geometries in inverted opal photonic crystals that can be easily fabricated by means of colloidal self-assembly. Two broad classes of defects were considered: interstitial and substitutional. Calculations for isolated as well as clumps of interstitial defects did not reveal promising changes to the bandstructure that could introduce a defect band into the photonic band gap. On the other hand, substitutional defects, wherein the air sphere is replaced by a smaller silica sphere surrounded by silicon, were found to be much more promising. By performing high resolution bandstructure calculations, we were able to determine that a silica sphere of radius between $0.33a$ and $0.35a$ could introduce a clear and usable defect mode into the gap. The state is found to be triply degenerate. We are encouraged by the results of our bandstructure, reflectance and local density of states calculations, all of which agree on the frequency of the defect mode. Since these are three different calculations, we have confidence that the defect mode exists.

The proposed defect can be made by replacing some of the $0.354a$ silica spheres with $0.35a$ spheres in the colloidal self-assembly process. Backfilling the assembled

structure with silicon should result in an thicker coating of silicon for the shrunk spheres than for the normal ones, yielding the geometry we put forward in this chapter. One possible problem with this approach, however, is that the smaller silica sphere is unlikely to be 'floating' between other spheres and might quite possibly be touching one of the larger spheres around it. This could prevent complete coating of the silica sphere during the backfill. If there is a silica-silica point of contact between the shrunk sphere and an adjacent sphere, then the wet-etching process could remove the silica from the defect sphere as well. One way of overcoming this problem would be to pre-coat the shrunk silica spheres with silicon. The ideal situation would be to have the $0.35a$ silica spheres coated with a layer of silicon that is $0.004a$ thick, resulting in a total radius of $0.354a$ for the 'hybrid' sphere. We can vary the density of such hybrid spheres in order to tune the Q value of the cavities. The higher the concentration, the smaller the effective supercell, and the stronger the coupling of radiation with the mode.

Chapter 3

Thermal emission and design in 1D-periodic metallic photonic crystal slabs

In this chapter, we present a useful framework within which we can understand some of the physical phenomena that drive thermal emission in 1D-periodic metallic photonic crystals, emphasizing phenomenology and physical intuition. We perform detailed numerical calculations for these systems and find that polarization and periodicity play key roles in determining the types of physical phenomena that can be excited. Two promising structures are identified as good candidates for thermal design. We conclude with a discussion of how the emissive properties of these systems can be tailored to our needs.

3.1 Introduction

The physics of blackbodies has been a source of fascination and scientific research for well over a century now[59]; properties of their thermal emission provided one of the most important clues for the discovery of quantum mechanics. In practice, most objects have only finite absorption, and are thus referred to as 'graybodies'. By virtue of Kirchhoff's law, these objects also have sub-unity emissivity. However,

graybodies are of interest because their thermal emission spectra can be changed by altering the geometry of the system or the materials used. The ability to modify or tailor the thermal emission profile of an object is of great importance and interest in many areas of applied physics and engineering. It has been noted recently that periodic sub-wavelength scale patterning of metallo-dielectric systems, i.e. photonic crystals, can modify their emission spectra in many interesting ways[70, 2, 53, 25, 54, 48, 16, 23], through various physical effects such as surface plasmons[61, 39], resonant-cavity enhancement[11], Bragg reflection[14] and modification of density of states via photonic band gaps[14, 41, 45, 46]. Thus, a clear and physically intuitive understanding of the mechanisms that can arise in such systems is of great value in guiding thermal design.

In this chapter, we focus on some of the most important physical phenomena that give rise to many of the features observed in thermal emission spectra of 1D-periodic metallic photonic crystal slabs, with the intention of developing physical intuition and understanding of features of emission spectra. We study these systems and demonstrate through detailed numerical studies the intricate dependence of these excitations on polarization, and how the type of periodicity can affect the characteristics of thermal emission spectra we observe. This enables us to analyze the emission spectra of 1D-periodic metallic photonic crystal slabs in order to identify, with confidence, the underlying physical phenomena and to understand the physics behind them; this way, we show how one can tailor the thermal emission properties of these structures to achieve one's design needs. For definiteness, we focus our attention on emission in the direction perpendicular to the plane of the slab.

This chapter is organized as follows: in section 3.2, we discuss the various physical phenomena that can influence the emission spectra of 1D-periodic metallic photonic crystal slabs. Section 3.3 outlines the numerical methods we use in our calculations. In section 3.4, we examine the role of polarization in these systems. In section 3.5, we turn our attention to periodicity and how it can give rise to surface plasmon excitations. Section 3.6 discusses the dependence of emission spectra on metallic material parameters, while in section 3.7, we give consideration to the role of diffraction and its

influence on emission spectra. In section 3.8, we show how the physical intuition and understanding developed in earlier sections can help us design the thermal emission spectra of these systems.

3.2 Physical phenomena that influence emission spectra

Kirchhoff's law states that for an object in thermal equilibrium with the surrounding radiation field, its absorptivity and emissivity are equal, for every frequency, direction, and polarization. Thus, to study thermal emission of an object, we need simply calculate its absorptivity spectrum, knowing that the object's absorptivity and emissivity spectra are identical. Moreover, for the purposes of developing an intuitive understanding of the physics behind thermal emission, it is often more helpful to think in terms of absorption rather than emission, and it is on this basis that we proceed.

In a 1D-periodic metallic photonic crystal (PhC) slab, there is a marked distinction between the two orthogonal directions within the plane of the slab (see graphic insets in Fig. 3-1). One direction (we shall call this x) is the direction of the PhC's periodicity, and is characterized by the existence of a discrete translational symmetry. The other direction (we shall call this y) supports continuous translational symmetry. The two types of translational symmetry can lead to drastically different physical effects in a 1D-periodic metallic PhC slab. Some of the phenomena that can be observed can be broadly described as waveguide cut-offs, waveguide resonances, surface plasmons and diffraction peaks. Each of these phenomena leaves a characteristic mark on the emission/absorption spectra. In our examination of the significant role played by polarization and periodicity in the physics of these systems, we will come across each of these interesting phenomena in turn. In this section, we give brief descriptions of these phenomena.

First, it is important to note that because of the mirror symmetry of the system

in a plane perpendicular to y (i.e. the xz-plane), the modes of the system can be separated into transverse electric (TE) and transverse magnetic (TM) modes with respect to the mirror plane. TE modes have field components E_x, E_z and H_y, and are even with respect to the mirror operation in the plane normal to y. TM modes, on the other hand, have field components H_x, H_z and E_y, and are odd with respect to the same mirror operation. Incident and outgoing light polarized in the x-direction can couple to TE modes while y-polarized light can couple to TM modes. Thus, we can analyze these two types of modes completely separately, and this is what we do in all our calculations.

Consider again the structure in Fig. 3-1. If we illuminate the structure with light incident from the top of the cell, the air gaps in the metal slab can be thought of as metallic waveguides channeling light downwards in the direction of $-z$. In other words, the light is propagating between two metal slabs that are infinite in the y-direction. Waveguide cut-offs arise from the requirement that the parallel component of the electric field (i.e. E_y in our case) be continuous across a boundary. Inside a perfect metal, the electric field is strictly zero. For such a material, E_y is constrained to vanish at the surface, and this leads to the well-known cut-off frequency corresponding to a half-wavelength oscillation in the x-direction. Below this frequency, no propagating mode can be supported within the waveguide, because the boundary condition cannot be satisfied. For a realistic metal (i.e. one that permits some penetration of fields), the fields do not exactly vanish at the surface, but decay away rapidly and exponentially once inside the material. Such boundary condition matching leads to a similar cut-off as in the case of the perfect metal, except that the penetration of field into the metal produces a cut-off with a slightly lower frequency, because the *effective* width of the waveguide in the x-direction is slightly larger. Cut-off frequencies depend on the width of the waveguide. The wider the waveguide, the lower the cut-off frequency. No such boundary condition holds for light polarized in the x-direction, so there is no waveguide cut-off for that polarization.

Continuing with the same waveguide setup, there exists another phenomenon which applies equally to light of either polarization. Waveguide resonances are analo-

gous to Fabry-Perot resonances except that they take place within a waveguide 'cavity'. Any narrow channel through which light is forced to propagate can be thought of as a Fabry-Perot cavity with partially reflecting mirrors at either end. If the incoming radiation is of a frequency such that the length of the cavity is equal to an integer number of half-wavelengths, we observe resonant transmission of light. We can think of these waveguide resonances as the consequence of boundary impedance matching in the longitudinal (z) direction. These resonances give rise to sharp peaks in the absorbance/emittance spectrum. Although this physical effect can be seen for either polarization of incident light, it is most prominent for light polarized in the x-direction whose spectra are not dominated by the existence of waveguide cut-offs.

Surface plasmons (SPs) are excitations that exist on the interface between a plane-metal and a dielectric. They are confined to the surface, but can propagate freely within that surface. They have a relatively simple dispersion relation that is approximately linear at low wave vectors and bends over toward a flat cut-off at higher wave vectors ($\omega_p/\sqrt{\epsilon+1}$ is the cut-off frequency, where ω_p is the plasmon frequency and ϵ is the dielectric constant). If the direction of propagation is x (i.e. $\mathbf{k}$ is in the x-direction), then the SP will have field components E_x, E_z and H_y (the z-direction is normal to the interface). The SPs are unusual in that they have an electric field component in the direction of propagation. Light incident from air cannot couple into SP modes since all SP modes are below the light line of air. However, it *can* couple into SP modes if the wave vector of the SP is along a direction of discrete translational symmetry, because in such a direction, wave vector is conserved only up to an integer multiple of the reciprocal lattice vector. These correspond to $k = 1, 2, 3...$ in units of $2\pi/a$. Thus, for our structure in Fig. 3-1, normally incident light polarized in x can couple into SPs propagating in the x-direction. In contrast, normally incident light polarized in y cannot couple into any SP modes.

Diffraction peaks occur when we consider the slab system at a macroscopic level, in terms of incoming and outgoing radiation modes. This effect is not unique to metallic PhCs, and can be observed in non-metallic PhCs as well. In terms of absorption, the incident light can couple to outgoing radiation modes (in transmission or reflection)

that conserve the wave vector in the x-direction (k_x) up to a reciprocal lattice vector, since that is the direction of discrete periodicity. Because the incident light has no k_x component, it can couple to outgoing modes with k_x equal to an integer multiple of $2\pi/a$ (i.e. 1 in our units). This means that as we increase the frequency of the incoming radiation, a new diffraction direction will be coupled into at $\omega = 1, 2, 3...$ (in units of $2\pi c/a$), corresponding to $k_x = 1, 2, 3...$ At the threshold frequency for a new diffraction mode, the wave vector has no k_z component, and so $\mathbf{k}$ is parallel to the surface of the slab. Such 'grazing' modes have maximum interaction with the slab because they travel close to the surface of the metal, and as such are strongly absorbed by the material. These absorption peaks translate into emission peaks, via Kirchhoff's law, so we would expect to see emission peaks for modes corresponding to $\omega = k = 1, 2, 3...$

3.3 Description of Numerical Methods

Before presenting our results, a brief description of our methods is in order. Numerical simulations in this chapter are performed using a finite-difference time-domain (FDTD) algorithm[75]. These are exact (apart from discretization) solutions of 3D Maxwell's equations, including material dispersion and absorption. We choose a computational cell with dimensions $40\times2\times240$ grid points, corresponding to 40 grid points per lattice constant a. This is essentially a 2D simulation, because k_y is constrained to be zero by periodic boundary conditions on opposite y-faces of the computational cell. The PhC slab is in the middle, and flux planes are placed on either side of it at least $2a$ away. We run the simulation for a total of 40,000 time steps, chosen to be sufficiently large to allow resolution of peaks with quality factors (Q) up to 250. We illuminate the photonic crystal slab with a normally incident, temporally Gaussian pulse. We record the fields going through flux planes on either side of the slab and perform a discrete Fourier-transform on the time-series of fields, which we use to calculate fluxes as functions of frequency, $\Phi(\omega) = \frac{1}{2}\mathrm{Re}\{\int \mathbf{E}^*(\mathbf{r},\omega) \times \mathbf{H}(\mathbf{r},\omega) \cdot \mathrm{d}\mathbf{S}\}$. We run the simulation once with the slab in place, and again with vacuum only, such

that $\mathbf{E}_{slab} = \mathbf{E}_{vac} + \mathbf{E}_{ref}$ between the source plane and the slab, with $\mathbf{E}_{ref}$ being the field due to reflection. The reflectance is given by

$$R(\omega) \equiv \frac{\Phi_{ref}}{\Phi_{vac}} = \frac{-\frac{1}{2}\mathrm{Re}\{\int_{A_1}[\mathbf{E}_{slab}(\mathbf{r},\omega) - \mathbf{E}_{vac}(\mathbf{r},\omega)]^* \times [\mathbf{H}_{slab}(\mathbf{r},\omega) - \mathbf{H}_{vac}(\mathbf{r},\omega)] \cdot \mathrm{d}\mathbf{S}\}}{\frac{1}{2}\mathrm{Re}\{\int_{A_1} \mathbf{E}^*_{vac}(\mathbf{r},\omega) \times \mathbf{H}_{vac}(\mathbf{r},\omega) \cdot \mathrm{d}\mathbf{S}\}} \tag{3.1}$$

where A_1 is the flux plane corresponding to '1', and the minus sign in the numerator is there to make the reflected flux positive. We can simplify the numerator as follows (dropping the dependence of fields on $(\mathbf{r},\omega)$ for clarity of notation):

$$\begin{aligned}
\Phi_{ref} &\equiv -\frac{1}{2}\mathrm{Re}\{\int_{A_1} (\mathbf{E}_{slab} - \mathbf{E}_{vac})^* \times (\mathbf{H}_{slab} - \mathbf{H}_{vac}) \cdot \mathrm{d}\mathbf{S}\} \\
&= -\Phi_1^{slab} - \Phi_1^{vac} + \frac{1}{2}\mathrm{Re}\{\int_{A_1} (\mathbf{E}^*_{vac} \times \mathbf{H}_{slab} + \mathbf{E}^*_{slab} \times \mathbf{H}_{vac}) \cdot \mathrm{d}\mathbf{S}\} \\
&= -\Phi_1^{slab} - \Phi_1^{vac} + \frac{1}{2}\mathrm{Re}\{\int_{A_1} [\mathbf{E}^*_{vac} \times (\mathbf{H}_{vac} + \mathbf{H}_{ref}) + (\mathbf{E}_{vac} + \mathbf{E}_{ref})^* \times \mathbf{H}_{vac}] \cdot \mathrm{d}\mathbf{S}\} \\
&= \Phi_1^{vac} - \Phi_1^{slab} + \frac{1}{2}\mathrm{Re}\{\int_{A_1} (\mathbf{E}^*_{vac} \times \mathbf{H}_{ref} - \mathbf{H}_{vac} \times \mathbf{E}^*_{ref}) \cdot \mathrm{d}\mathbf{S}\}
\end{aligned}$$

where the flux plane closer to the light source is '1', and the flux plane further from the light source is '2'. The cross term vanishes for incoming and outgoing plane waves crossing the flux planes in vacuum, for which $\mathbf{E}$ and $\mathbf{H}$ are proportional. Therefore, the expression for reflectance simplifies to

$$R(\omega) = [\Phi_1^{vac}(\omega) - \Phi_1^{slab}(\omega)]/\Phi_1^{vac}(\omega)$$

Similarly, the transmittance is given by $T(\omega) = \Phi_2^{slab}(\omega)/\Phi_2^{vac}(\omega)$ and the absorbance is simply $A(\omega) = 1 - R(\omega) - T(\omega)$. This way, we obtain reflectance, transmittance and absorbance spectra for PhC slabs. We incorporate absorption into our simulations by means of the Drude model, according to the following equation:

$$\epsilon(\omega) = \epsilon_\infty + \frac{\omega_p^2}{\omega_0^2 - \omega^2 - i\gamma\omega}$$

w	cut-off	$\lambda/2$
0.2	0.984	0.32
0.3	1.22	0.41
0.4	1.56	0.51

Table 3.1: The waveguide cut-off frequencies associated with different gap widths in Fig. 3-1a, and their corresponding half-wavelengths.

where ϵ_∞, γ, ω_0 and ω_p are input parameters. In our case, we are concerned with metals, for which $\omega_0 = 0$. (For metals, ω_p is known as the plasmon frequency.) By Kirchhoff's law, the absorbance spectra so calculated are identical to the emittance spectra of these objects, for each polarization, frequency and observation angle.

3.4 Role of Polarization

Let us now make our discussion more concrete by considering a real 1D system. We study a 1D-periodic metal slab with gaps (as in Fig. 3-1) by calculating the emittance of such an object at normal incidence. For now, we focus on y-polarized light, i.e. light polarized in the direction of *continuous* translational symmetry. Fig. 3-1a shows the emittance spectrum for this structure for a few different gap widths. (We include the transmittance spectrum (dotted lines) for completeness.) The first peak we see in emittance, whose frequency varies with the gap width, corresponds to the waveguide cut-off that we described earlier, which is the frequency at which one can just fit approximately half a wavelength into the gap in the x-direction. In reality, there is penetration of evanescent waves into the surrounding metal in the x-direction which makes the gap effectively wider than it is. As we increase the gap width, the waveguide cut-off frequency decreases, as expected. From the frequencies of the peaks, we can deduce the half-wavelength associated with these cut-offs, and we find that they are slightly larger than the widths of the gaps, as predicted (see Table 3.1). The half-wavelengths are about $0.1a$ larger than the actual gap widths, demonstrating penetration of fields into the bulk of the metal. In Fig. 3-1b, we hold the gap width constant and vary the thickness of the slab. The waveguide cut-off is clearly seen around $\omega \approx 1.5c/a$, and is the same for all thicknesses. The dotted

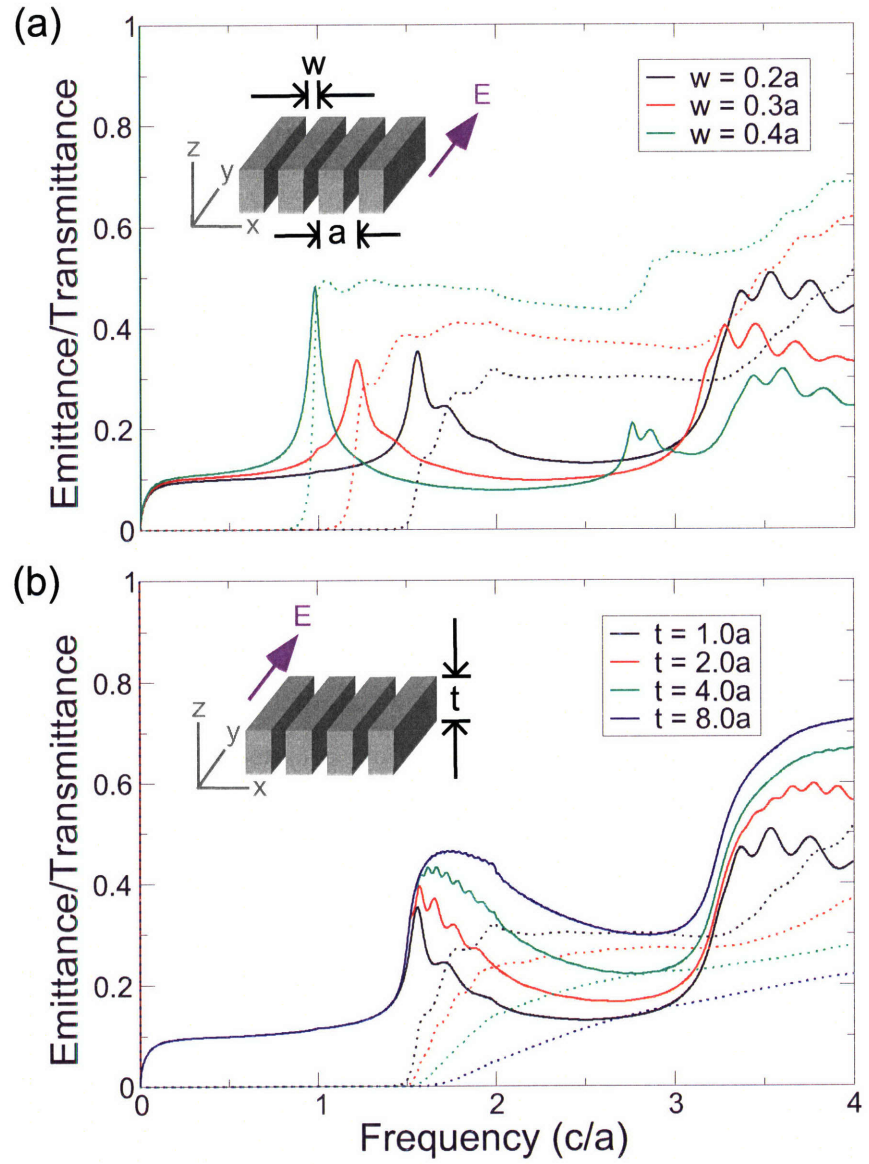

Figure 3-1: (Color) Here we show emittance (solid lines) and transmittance (dotted lines) spectra for y-polarized light emitted from a 1D-periodic metal slab with gaps, viewed at normal incidence. The Drude parameters used are $\epsilon_\infty = 1$, $\omega_0 = 0$, $\gamma = 0.15(2\pi c/a)$ and $\omega_p = \sqrt{10}(2\pi c/a)$. In Panel (a), we fix the thickness of the slab at $1.0a$ (where a is the lattice constant of the slab) and vary the width of the gaps. In Panel (b), we hold the gap width constant at $0.2a$ and vary the thickness of the slab.

freq.	$\lambda/2$	$2/n$
1.577	2.20	2
1.658	0.89	1
1.760	0.61	$\frac{2}{3}$
1.880	0.48	$\frac{1}{2}$

Table 3.2: The waveguide resonant frequencies associated with the red curve in Fig. 3-1b, and their corresponding half-wavelengths, calculated and predicted.

lines show transmittance decreasing with increasing slab thickness; as expected, more light is being absorbed while propagating through longer waveguides. Notice the small oscillations between $1.5c/a$ and $2.0c/a$. These are the waveguide resonances we discussed earlier. The number of such oscillations increases with the thickness of the slab. Indeed, we see that the red curve has twice as many oscillations as the black curve, and the green curve twice as many as the red curve, and so on. We took the four peaks from the red curve, recorded their frequencies, and calculated their half-wavelengths in the z-direction (see Table 3.2). The half-wavelengths ($\lambda_z/2$) are calculated using the formula $(\omega/c)^2 = (2\pi/\lambda_x)^2 + (2\pi/\lambda_z)^2$, where λ_x is the half-wavelength in the x-direction (obtained from Table 3.1) and λ_z is the half-wavelength in the direction of guided propagation. In the third column of Table 3.2, we put the expected/predicted number of half-wavelengths that fit into the vertical cavity. For example, the nth-order harmonic fits n half-wavelengths into the waveguide in the z-direction, so we would expect to see a half-wavelength of $2/n$ in units of a, since the thickness of the slab is $2.0a$. Assuming the first peak listed in Table 3.2 is the second harmonic, we see good correspondence between the half-wavelengths calculated from the emission peaks and the expected half-wavelengths. Thus, we can be confident that the peaks in frequency range 1.5 to 2.0 are due to Fabry-Perot resonances in the waveguides.

In both panels of Fig. 3-1, we see a dramatic rise in transmittance and emittance above $\omega_p = \sqrt{10} \approx 3.16$ because the material behaves as a regular dielectric (rather than metal) above the plasmon frequency. We see some oscillations above $3.25c/a$; these are dielectric slab resonances, which are analogous to waveguide Fabry-Perot resonances except that they permeate the entire slab. Once again, the number of

oscillations increases with increasing slab thickness. Thus, we see relatively simple physical effects for incident light polarized in the y-direction.

Significantly different emission and transmission characteristics can be observed for the same structure for light of an orthogonal polarization (i.e. polarized in the x-direction). Since Maxwell's equations do not require that the perpendicular component of electric field (E_x) be continuous across a boundary, the waveguide cut-offs in the x-direction no longer exist. Instead, we expect to see resonances in the z-direction within the waveguide cavity. We study the same 1D-periodic metal slab with gaps as in Fig. 3-1, except that this time, we focus on emitted light polarized in the x-direction, the direction of *discrete* translational symmetry. In Fig. 3-2a, we show emittance and transmittance spectra for this system as a function of gap width. First, we notice that there is high transmittance (dotted lines) at nearly all frequencies shown. Contrast this with Fig. 3-1a, which had zero transmittance for frequencies below the waveguide cut-off at $\omega \approx 1$. The two lowest frequency emittance peaks in the black curve are waveguide cavity resonances (we shall discuss this further in Fig. 3-2b). Between $\omega = 1$ and $\omega = \omega_p \approx 3.16$, the spectra shown here are very different from those in the corresponding frequency range in Fig. 3-1a. However, above the plasmon frequency, the entire structure behaves as a dielectric, and the differences between the two polarizations are no longer as pronounced. Indeed, we observe similar emittance curves for both polarizations above the plasmon frequency (high transmittance and slab resonances which increase in number with thickness).

In Fig. 3-2b, we hold the gap width constant at $0.2a$ and vary the thickness of the slab. The most interesting phenomenon here is the number of sharp peaks between $\omega = 0$ and $\omega = 1$. The fact that their number and density increase with the thickness of the slab is clear evidence that they are produced by waveguide resonances in the z-direction. To confirm this suspicion, we plot the field profiles for two resonances on the red curve (first and fourth resonances), as indicated by the two black arrows (I and II). For each resonance, we plot E_x and E_z side by side. The resonances were excited by normally incident light coming down from the top of the computational cell, in the absorbance setup. We notice that the first resonance has one E_x node

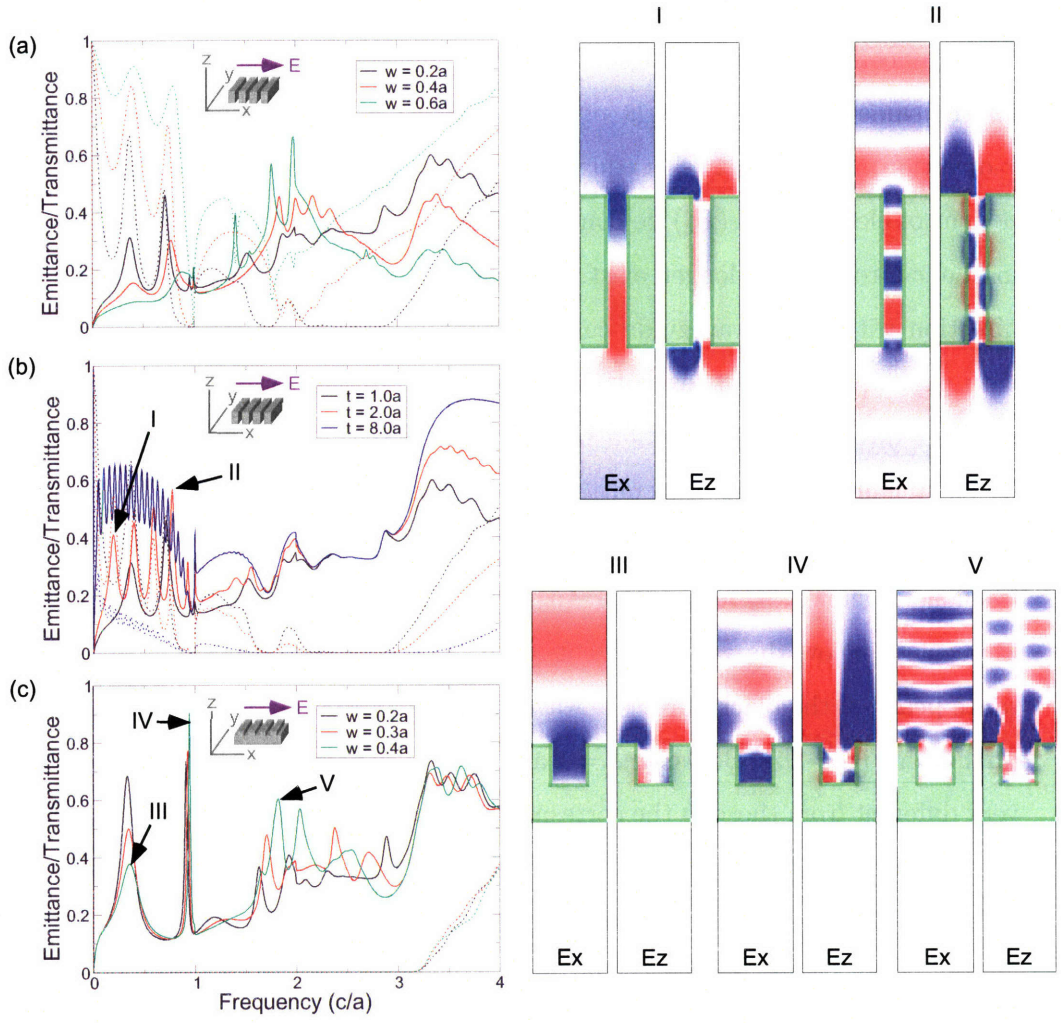

Figure 3-2: (Color) We show emittance (solid lines) and transmittance (dotted lines) spectra for a 1D-periodic metal slab for normal incidence and light polarized in the x-direction. The Drude parameters used are $\epsilon_\infty = 1$, $\omega_0 = 0$, $\gamma = 0.15(2\pi c/a)$ and $\omega_p = \sqrt{10}(2\pi c/a)$. In Panel (a), we fix the thickness of the slab at $1.0a$ and vary the width of the gaps. In Panel (b), we hold the gap width constant at $0.2a$ and vary the thickness of the slab. In Panel (c), we study a corrugated metal slab of thickness $1.0a$ with a gutter of depth $0.5a$, for different gutter widths. To better understand some of the modes exhibited in these panels, we show field profiles for peaks labeled I-V on the right half of the figure. Each pair of field plots shows E_x on the left and E_z on the right. The edges of the computational cell are marked by thin black lines, while the metallic structure is shown in a translucent green color with dark green borders. The incident beam comes down from the top of the cell.

within the waveguide in the z-direction. For the fourth resonance on the red curve, we expect four nodes, and indeed this is what we find. Although in (I) we see that E_x has one node in the middle of the waveguide, it is in fact the lowest order mode because H_y (not shown), which is related to $\partial E_x/\partial z$ through Ampère's law, has a maximum at that same point in the middle of the waveguide, and no node. (Note that H_y is a scalar in this case because we are considering a TE mode which has only one component of magnetic field in the y-direction.) Another interesting feature is the nodal line in E_z down the middle of the waveguide. This arises because E_z is given by $\partial H_y/\partial x$ (from Faraday's law). Since there is a maximum in H_y as we traverse the waveguide in the x-direction, there is a node in E_y. Note also that the node in E_x is shifted upwards from the center of the waveguide because the incident wave coming down from the top of the cell interacts with the resonance inside the waveguide in such a way as to shift the position of the node of the combined fields upwards.

In Fig. 3-2c, we study a corrugated metal slab, for various gutter widths, in order to see how things are different when we prevent direct transmission of light through the solid. First of all, above the plasmon frequency we see the same transparent behavior and the familiar dielectric slab resonances. However, the rest of the emittance spectrum looks very different. To better understand some of these modes, we show field profiles for three of the peaks on the green curve (III-V). In each set of field plots, we can see the incident beam and also a sort of cavity mode inside the gutter. These cavity modes are analogous to the case when we had gaps/waveguides in the metal, except that they are terminated differently: instead of being terminated with air, they are terminated with metal. This is most pronounced in the case of (V) ($\omega \approx 1.8$), which shows strong fields being pinned to the corners and edges of the gutter.

Thus, we see that polarization plays a key role in 1D-periodic systems. Because one kind of polarization sees a continuity boundary condition when impinging on a metallic surface and the other does not, drastically different physical effects are observed. In the next section, we discuss the intricate connection between periodicity

and surface plasmons.

3.5 Periodicity and surface plasmons

Most of the physical effects we have seen so far have been explainable in terms of Maxwell boundary conditions which require us to fit an integer or half-integer number of wavelengths within a particular resonant cavity. We now turn our attention to a totally different type of physical phenomenon, one which does not arise from such resonances in cavities: surface plasmons. These are affected by periodicity because wave vector has to be conserved up to a reciprocal lattice vector in a direction of periodicity; however, along a direction of continuous translational symmetry, wave vector has to be absolutely conserved. Since the x-direction is, in our case, discretely periodic, normally incident light polarized in x can couple into SP modes with integer k (in units of $2\pi/a$). The y-direction, however, has continuous translational symmetry, so incident light polarized in y cannot couple into SP modes in the system.

We consider a uniform metal slab with small dielectric strips on its surface. (We use dielectric strips instead of metallic ones in order to keep the metal surface uniform; a metallic strip/corrugation would have led to SP modes on two different planes, producing much stronger modification of the SP dispersion relation. In turn, such a system would be less tractable intuitively.) We excite SP modes in the system, and they emit light at normal incidence, polarized in the x-direction. Fig. 3-3a shows how emittance and transmittance vary with the dielectric constant of the strip (ϵ). First, we observe many peaks in the emittance spectra, and we note that the frequencies of these peaks decrease with increasing ϵ. Second, we see zero transmittance in the system for frequencies below $\omega_p \approx 3.16$, as we expect, because the metal is opaque at frequencies below the plasmon frequency. Third, we demonstrate that most of the emittance peaks with frequencies below 2.0 observed in Fig. 3-3a are in fact produced by SPs.

To show this, we record the frequencies of the peaks (up to $\omega_p/\sqrt{\epsilon+1}$, the SP cut-off) for each curve in Panel (a), and plot them as circles (red circles corresponding

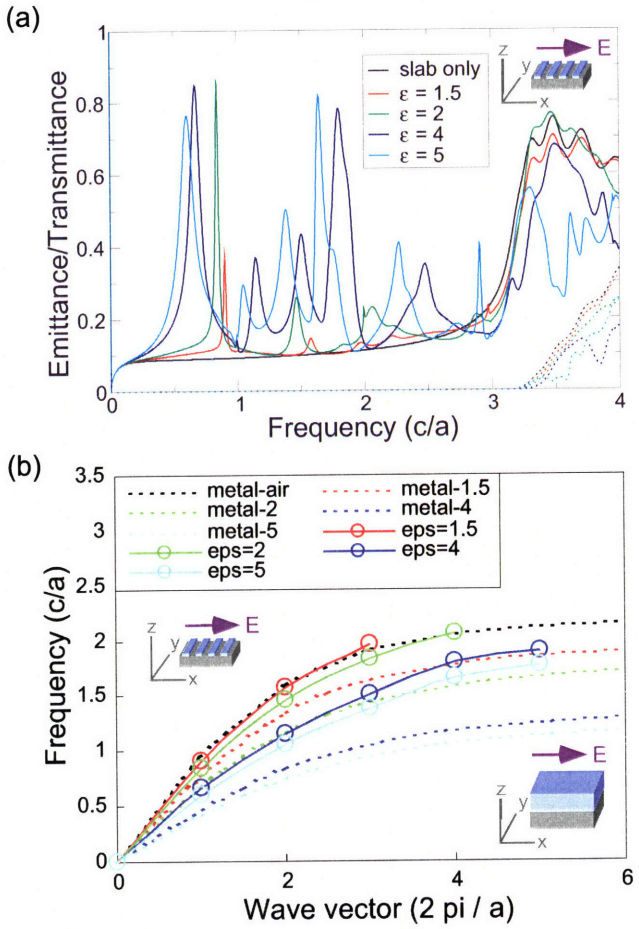

Figure 3-3: (Color) We present emittance (solid lines) and transmittance (dotted lines) spectra for a uniform metal slab with thin dielectric strips periodically distributed on its surface. We consider light emitted/transmitted at normal incidence and polarized in the x-direction. The dielectric structure has a rectangular cross section of width $0.5a$ and height $0.2a$, and sits on top of a metal slab of thickness $1.0a$. The metal has Drude parameters $\epsilon_\infty = 1$, $\gamma = 0.15(2\pi c/a)$ and $\omega_p = \sqrt{10}(2\pi c/a)$. Panel (a) shows how emittance and transmittance vary for a few different dielectric constants of the strips. In Panel (b), we plot the frequencies of some of the peaks in Panel (a) as circles (red circles corresponding to red peaks, for example). In addition, we plot SP dispersion curves for uniform, semi-infinite metal-air and metal-dielectric structures (dotted lines). Top-left inset shows structure described by solid lines; bottom-right inset shows structure described by dotted lines.

to red peaks, for example), making the assumption that the first peak has a wave vector of $1.0(2\pi/a)$, the second has a wave vector of $2.0(2\pi/a)$, and so on. We make this assumption because, as we have said, normally incident light can only couple to SP modes with integer wave vectors (in units of $2\pi/a$) in the direction of periodicity. Thus, we expect to see successive SP peaks with increasing frequencies corresponding to $k = 1, 2, 3...$ SP modes. In addition, we plot SP dispersion curves for uniform and semi-infinite metal-air and metal-dielectric structures (dotted lines). Surface plasmon modes in the periodic structure under consideration would therefore be expected to have a dispersion relation that lies between different SP dispersion relations of the case when the dielectric is uniform. For example, we would expect the red circles to lie between the black and red dotted curves, the green circles to lie between the black and green dotted curves, and so on. Indeed, this is exactly what we see. Furthermore, the fact that the circles, when joined together by solid lines, form a dispersion relation that clearly bends over toward a cut-off, gives us confidence in identifying these modes as surface plasmons. Note also that, in Fig. 3-3a, no SP peaks are observed in the case of the uniform and unperturbed metal slab (black curve), just as expected: in that case, continuous translational symmetry in the x-direction is maintained, so incident light cannot couple to the SP modes of the system.

3.6 Dependence on metallic material parameters

We have seen the pivotal role played by polarization in the kinds of modes we can thermally excite in a 1D-periodic metallic PhC slab system. We have also examined the conditions under which SP modes can be excited, and the relation of these modes to the type of translational symmetry exhibited by the structure (continuous or discrete). With this knowledge, we can design, analyze and understand a diverse array of 1D-periodic metallic PhC slab structures. For completeness, we examine a few other interesting physical effects which can arise in such systems.

This time, we study light emanating from a corrugated metal slab at normal incidence and polarized in the y-direction. In Fig. 3-4a, we show how emittance

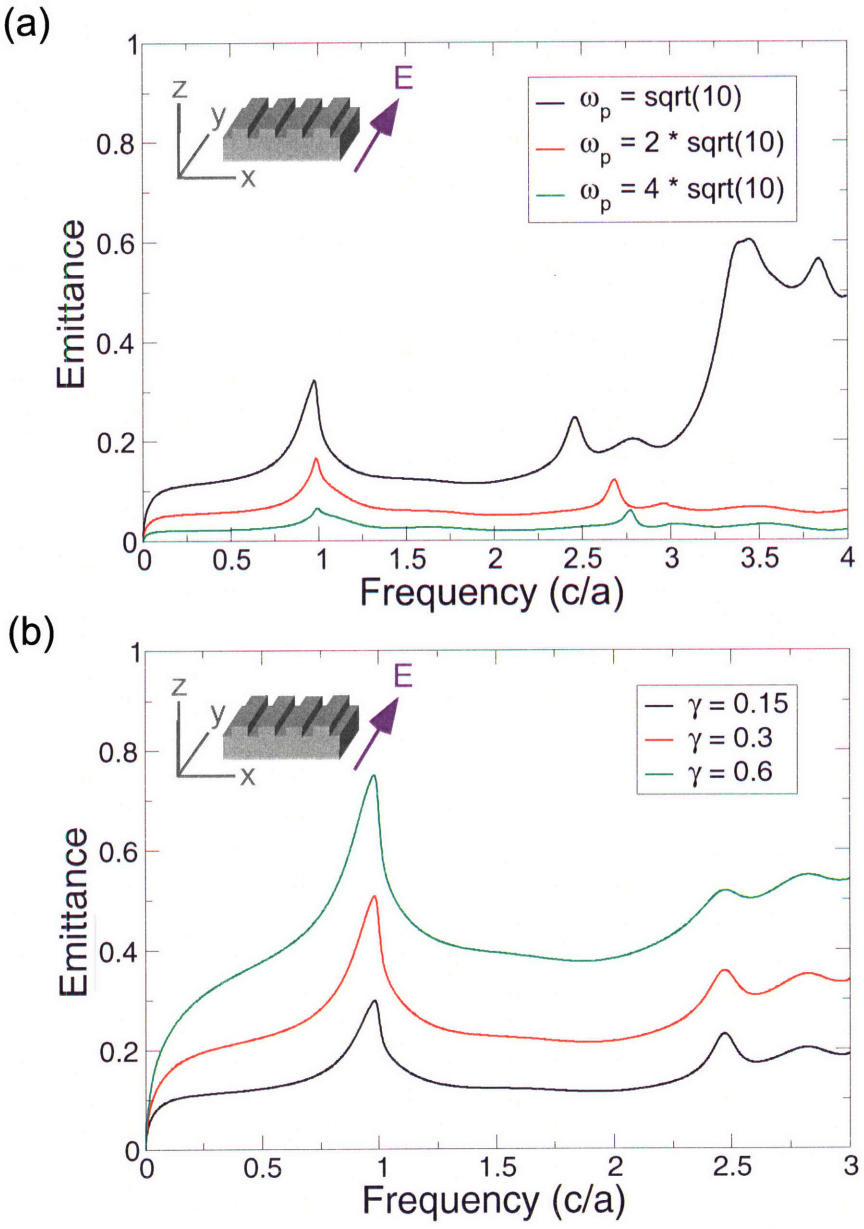

Figure 3-4: (Color) Emittance spectra for a corrugated metal slab, for normal incidence and y-polarization. The metal slab has thickness $1.0a$, with gutters of depth $0.5a$ and width $0.5a$. The metal has the usual Drude parameters of $\epsilon_\infty = 1$, $\gamma = 0.15(2\pi c/a)$ and $\omega_p = \sqrt{10}(2\pi c/a)$. In Panel (a), we show how emittance changes with the plasmon frequency (ω_p). Panel (b) shows the variation of emittance with γ, the parameter that controls material losses in the Drude model (in this case $\omega_p = \sqrt{10}$). Note that in both panels, clear diffraction peaks are seen at $\omega = 1$, and the positions of these peaks do not change with either ω_p or γ.

changes with the plasmon frequency (ω_p) of the metal. One can easily observe an inverse proportionality relationship between background emittance and ω_p. Using the Drude model, we can show that in the regime specified by $\gamma \ll \omega \ll \omega_p$, the absorbance, and therefore the emittance, is given approximately by $2\gamma/\omega_p$.

Consider light incident on a semi-infinite slab of metal with dielectric function

$$\epsilon(\omega) = 1 - \frac{\omega_p^2}{\omega^2 + i\gamma\omega}$$

where we have chosen $\epsilon_\infty = 1$ and $\omega_0 = 0$, as is consistent with our numerical calculations. Breaking this up into real and imaginary parts, we have

$$\epsilon_1 = 1 - \frac{\omega_p^2/\gamma^2}{1 + \omega^2/\gamma^2} \tag{3.2}$$

$$\epsilon_2 = \frac{\omega_p^2/\gamma}{\omega(1 + \omega^2/\gamma^2)} \tag{3.3}$$

We can convert these into expressions for the real and imaginary parts of the refractive index, using the equality $\epsilon_1 + i\epsilon_2 = (n+ik)^2$. Making the approximation $\gamma \ll \omega \ll \omega_p$, we have

$$n = \frac{\gamma\omega_p}{2\omega^2} \tag{3.4}$$

$$k = \omega_p/\omega \tag{3.5}$$

For a semi-infinite slab of metal, the reflectance (R) is given by

$$R = \frac{(n-1)^2 + k^2}{(n+1)^2 + k^2}$$

Substituting our expressions for n and k into the above expression yields, approximately,

$$R \approx 1 - \frac{2}{\omega_p/\gamma}$$

from which the absorbance (A) follows:

$$A \equiv 1 - R = \frac{2\gamma}{\omega_p} \tag{3.6}$$

This is precisely the inverse proportionality relationship we observe between absorbance and ω_p.

Again, we see, for the black curve, that emittance increases significantly at frequencies above $\omega_p = \sqrt{10} \approx 3.16$, because above the plasmon frequency the metal becomes transparent to incident radiation, which penetrates the whole structure, leading to greater absorption and thereby greater emission. (This is not seen in the red and green curves because their plasmon frequencies are out of the plotting range.) Fig. 3-4b shows the variation of emittance with γ, the parameter that controls material losses in the Drude model. We observe that the background emittance increases almost linearly with increasing γ. This can be understood by considering $\mathrm{Im}(\epsilon) \sim \gamma/[\omega(\omega^2 + \gamma^2)]$, which, for high frequencies ($\omega \gg \gamma$), is roughly linear in γ. This is also consistent with Equation (3.6), which is approximate. Finally, we point out that in both panels, clear diffraction peaks are seen at $\omega = 1$, and the positions of these peaks do not change with either ω_p or γ.

3.7 Role of diffraction

In Fig. 3-5, we show emittance and transmittance spectra for a corrugated metal slab for normally incident light polarized in the y-direction, for two different gutter widths. We observe that there are small emittance peaks at the integer frequencies ($\omega = 1, 2, 3$). These peaks are caused by diffraction. The size of these diffraction peaks depends on the geometry of the system and the materials used. Notice that diffraction peaks do not appear in the case of a uniform metal slab (black curve), because such a slab has continuous translational symmetry in the x-direction. This symmetry implies that the transverse wave vector is *absolutely* conserved, with the consequence that only modes for which $k_x = 0$ can couple to outgoing modes at normal incidence.

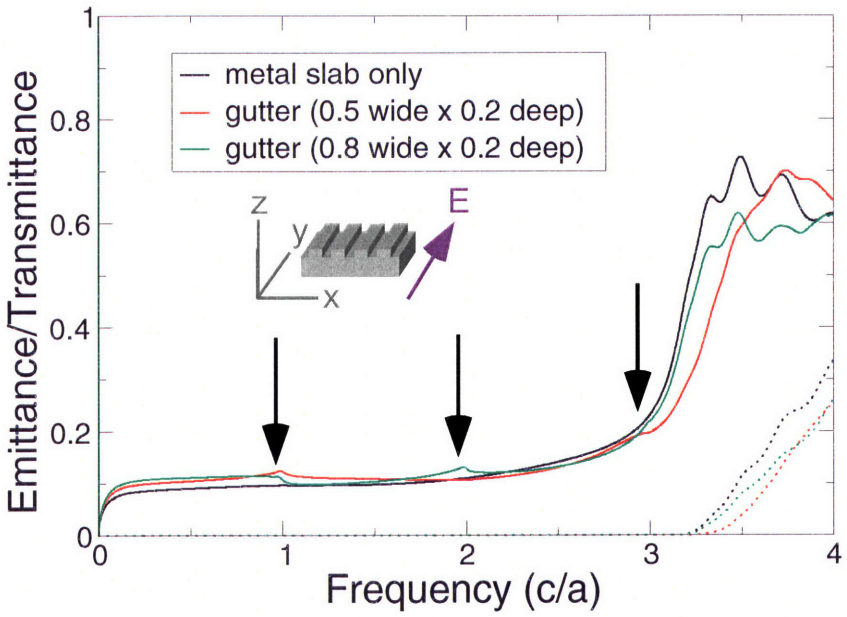

Figure 3-5: (Color) We show emittance and transmittance spectra for a corrugated metal slab produced by normally incident light, polarized in the y-direction, for two different gutter widths. The metal has Drude parameters $\epsilon_\infty = 1$, $\gamma = 0.15(2\pi c/a)$ and $\omega_p = \sqrt{10}(2\pi c/a)$. The metal slab has thickness $1.2a$, with gutters of depth $0.2a$ and width $0.5a$ (red curve) and $0.8a$ (green curve). We observe that there are small emittance peaks at integer frequencies ($\omega = 1, 2, 3$, indicated by black arrows), caused by diffraction. Notice that no diffraction peaks are seen in the case of a uniform metal slab (black curve), because such a slab has continuous translational symmetry in the x-direction. Note also the sudden rise in transmittance and emittance above the plasmon frequency ($\omega_p \approx 3.16$), above which the metal is transparent.

In other words, a uniform metal slab is unable to produce diffracted beams. Note also the sudden rise in transmittance and emittance above the plasmon frequency ($\omega_p \approx 3.16$), above which the metal acts as a dielectric.

3.8 Thermal design

Now that we have a good understanding of the physical effects that thermal emission can produce, we turn our attention to thermal design using 1D-periodic metallic PhCs. Of the many systems we studied in this chapter, the corrugated metal slab and the slab with dielectric strips are the most promising in terms of emissivity enhancement, and it is to these two structures that we devote our attention. Fig. 3-6a shows the power emitted by a corrugated metal slab (identical to the one in Fig. 3-2c), at two different temperatures (1000K and 1200K). We show also emission spectra for a blackbody (the Planck distribution) and a uniform slab for comparison. First, we notice that the positions of the peaks do not change with temperature. Second, increasing temperature increases emission at *all* wavelengths, as expected by Stefan's law. Third, the relative weighting given to different wavelengths changes with temperature, because the peak of the Planck distribution shifts toward lower wavelengths with increasing temperature. In our case, the group of small peaks between 1 and $2\mu m$ were insignificant features at 1000K, but became much more prominent at 1200K, because the blackbody spectrum shifted in such a way as to give those peaks much more weight than before. Fourth, the emission of the photonic crystal slab exceeds that of the uniform slab at all wavelengths and at all temperatures. In fact, the enhancement is impressive: we see a 10-fold increase in emissive power (over that of a slab) at the major peak at around $3.1\mu m$. Of course, emissivity never exceeds unity, because that would violate the Second Law of Thermodynamics (the large peak in question attains 90% emissivity). The important lesson we learn from this is that we can emphasize different parts of the emission spectrum of a PhC by changing the temperature at which we operate the thermal structure.

In Fig. 3-6b, we present the emissive power of a metal slab with dielectric strips

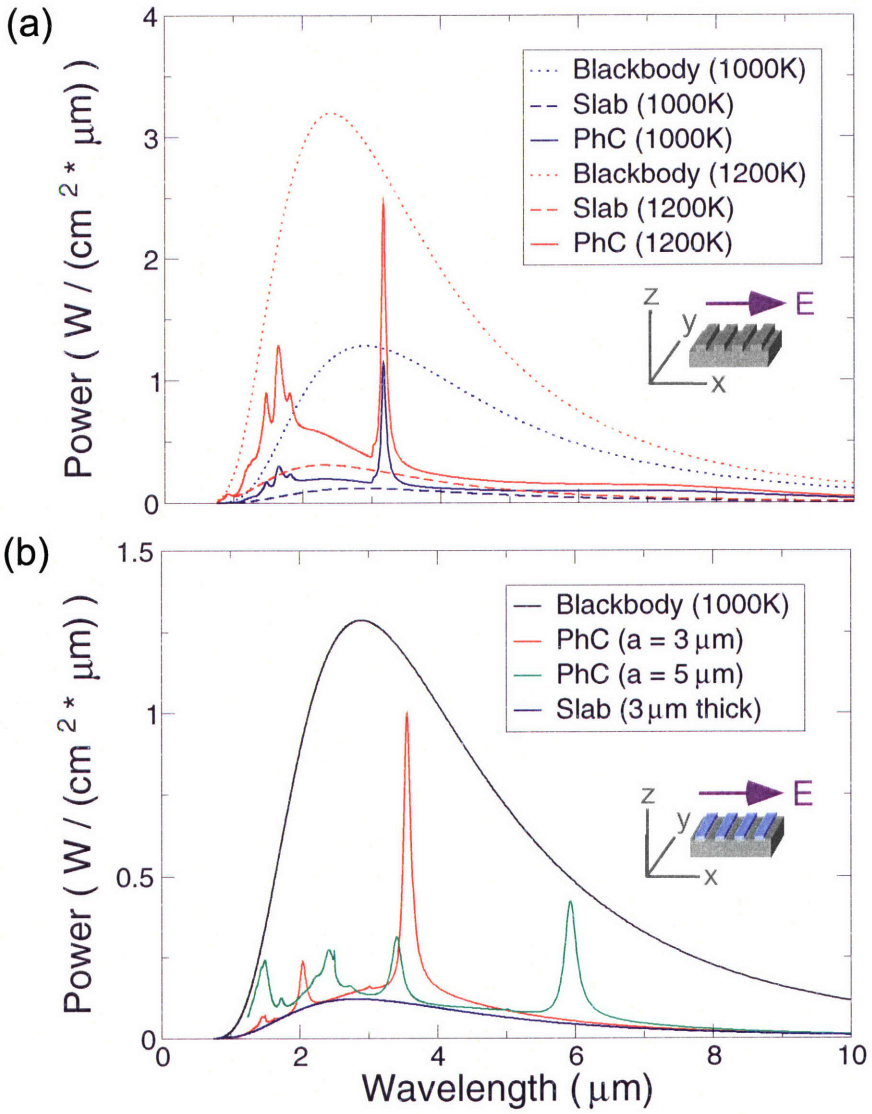

Figure 3-6: (Color) Panel (a) shows how emissive power for a corrugated metal slab changes with temperature of operation. The emission spectra is observed at normal incidence, polarized in the y-direction. The metal has Drude parameters $\epsilon_\infty = 1$, $\gamma/(2\pi c) = 500cm^{-1}$ and $\omega_p/(2\pi c) = 10540cm^{-1}$. The metal slab has thickness $3\mu m$, with gutters of depth $1.5\mu m$ and width $1.2\mu m$. We show the spectra for the blackbody, the PhC, and the uniform metal slab (thickness $3\mu m$) for two temperatures, 1000K and 1200K. Panel (b) shows how emissive power for a metal slab with dielectric strips changes with the lattice constant. The metal slab is of thickness $3\mu m$, while the dielectric strips are of width $1.5\mu m$, height $0.6\mu m$, and $\epsilon = 2$. Clearly, increasing the lattice constant increases the wavelength at which peak emission occurs. Note that the peaks arise from the excitation of surface plasmon modes.

on top (similar to the one in Fig. 3-3a). Here, instead of changing the temperature, we keep temperature fixed and vary the lattice constant of the PhC. The blackbody envelope and the emission spectrum of a uniform slab of this same metal are shown for comparison. We see that increasing the lattice constant shifts the emission peaks in the PhC toward a higher wavelength. In our case, for $a = 3\mu m$, the large peak is already close to the point of maximum blackbody emission, so that increasing the lattice constant only served to decrease the total emission from that excitation (incidentally, it is a surface plasmon excitation). However, the change in a also brought some small peaks from the lower wavelengths into the picture. Clearly, one has a substantial degree of control over the positions of the peaks. One should realize that in both cases, the emissivity of the peak is unchanged, because PhC emissivity spectra are scale invariant (contrast this with that of a uniform slab, whose absolute emission spectrum does not scale with a, since it has continuous translational symmetry). For both choices of a, there is significant enhancement of emission over that of a uniform slab.

3.9 Conclusion

We demonstrated a physical and intuitive framework within which the thermal behavior of 1D-periodic metallic photonic crystal slabs can be understood. In such systems, polarization and periodicity play key roles in our understanding of waveguide cut-offs, waveguide Fabry-Perot resonances, SP modes and diffraction peaks. We found that metal slabs with corrugation or dielectric strips are good building blocks for thermal design, because they have strong emission peaks with high emissivity. These peaks can be shifted to the desired wavelength by changing the lattice constant of the system, while other parts of the emission spectrum can be amplified and made more prominent by altering the temperature of operation, which changes the weight given to a particular range of wavelengths. One can use the principles described here to tailor and design thermal emission using 1D-periodic metallic photonic crystal slabs.

Chapter 4

Thermal emission and design in 2D-periodic metallic photonic crystal slabs

We present a useful framework within which we can understand some of the physical phenomena that drive thermal emission in 2D-periodic metallic photonic crystal slabs, emphasizing phenomenology and physical intuition. Through detailed numerical calculations for these systems, we find that periodicity plays a key role in determining the types of physical phenomena that can be excited. We identify two structures as good candidates for thermal design, and conclude with a discussion of how the emissive properties of these systems can be tailored to our needs.

4.1 Introduction

A blackbody is defined as an object of perfect absorption. Its entropy is maximized, and in that sense it exemplifies utter disorder. The physics of blackbodies has both fascinated and intrigued scientists for well over a century now[59]. In practice, most objects have only finite absorption, and are thus referred to as 'graybodies'. However, graybodies are of interest because their thermal emission spectra can be changed by altering the geometry of the system or the materials used. The ability to modify or

tailor the thermal emission profile of an object is of great importance and interest in many areas of applied physics and engineering. It has been noted that periodic sub-wavelength scale patterning of metallo-dielectric systems, i.e. photonic crystals, can modify their emission spectra in interesting ways[70, 44, 14, 7, 41, 17, 69, 25, 22, 45, 46, 68, 54, 48, 39, 11, 23]. Thermal radiation from 2D-periodic photonic crystals has been studied within the contexts of spectral and directional control[51, 69, 61, 16, 38], guided resonances[19], thermophotovoltaic generation[68], resonant scattering[58, 15], laser action[50], Kirchhoff's law[48], coherence[25, 38], and spontaneous emission enhancement[7, 17, 61].

In this chapter, we focus on some of the most important physical phenomena that give rise to many of the features observed in thermal emission spectra of 2D-periodic metallic photonic crystal slabs, with the intention of developing physical intuition and understanding of features of emission spectra. We demonstrate through detailed numerical studies the key role played by periodicity in determining the types of physical phenomena that can be thermally excited in 2D-periodic metallic photonic crystals. We develop understanding and physical insight using two illustrative examples, before applying them to hybrid structures. Such structures exhibit strong thermal emission peaks which can be used as building blocks in thermal design. We show how one can tailor the emissive properties of these structures to one's design needs by changing two simple physical parameters.

4.2 Description of Numerical Methods

Kirchhoff's law states that for an object in thermal equilibrium with the surrounding radiation field, its absorptivity and emissivity are equal, for every frequency, direction, and polarization. Thus, to study thermal emission of an object, we need simply calculate its absorptivity spectrum, knowing that the object's absorptivity and emissivity spectra are identical. Moreover, for the purposes of developing an intuitive understanding of the physics behind thermal emission, it is often more helpful to think in terms of absorption rather than emission, and it is on this basis that we will

proceed.

It is important to note that because of the mirror symmetry of the system in a plane perpendicular to x and y, the modes of the system can be separated into transverse electric (TE) and transverse magnetic (TM) modes with respect to the mirror plane. As a result of this symmetry, x-polarized modes do not mix with y-polarized modes. Thus, we can analyze these two polarizations completely separately, and this is what we do in all our calculations.

Numerical simulations in our work are performed using a finite-difference time-domain (FDTD) algorithm[75]. These are exact (apart from discretization) 3D solutions of Maxwell's equations, including material dispersion and absorption. We choose a computational cell with dimensions $40 \times 40 \times 240$ grid points, corresponding to 40 grid points per lattice constant a. The faces of the cell normal to the x and y axes are chosen to have periodic boundary conditions, while the faces normal to the z-axis (i.e. the top and bottom ones) have perfectly matched layers (PML) to prevent reflection. In other words, this is a 3D simulation of a 2D-periodic system. The PhC slab is in the middle, and flux planes are placed on either side of it at least $2a$ away. We run the simulation for a total of 40,000 time steps, chosen to be sufficiently large to allow resolution of peaks with quality factors (Q) up to 250. We illuminate the photonic crystal slab with a normally incident, temporally Gaussian pulse. We record the fields going through flux planes on either side of the slab and perform a discrete Fourier-transform on the time-series of fields, which we use to calculate fluxes as functions of frequency, $\Phi(\omega) = \frac{1}{2}\mathrm{Re}\{\int \mathbf{E}^*(\mathbf{r},\omega) \times \mathbf{H}(\mathbf{r},\omega) \cdot \mathrm{d}\mathbf{S}\}$. We run the simulation once with the slab in place, and again with vacuum only, such that $\mathbf{E}_{slab} = \mathbf{E}_{vac} + \mathbf{E}_{ref}$, with $\mathbf{E}_{ref}$ being the field due to reflection. The reflectance is given by

$$R(\omega) \equiv \frac{\Phi_{ref}}{\Phi_{vac}} = \frac{-\frac{1}{2}\mathrm{Re}\{\int_{A_1} [\mathbf{E}_{slab}(\mathbf{r},\omega) - \mathbf{E}_{vac}(\mathbf{r},\omega)]^* \times [\mathbf{H}_{slab}(\mathbf{r},\omega) - \mathbf{H}_{vac}(\mathbf{r},\omega)] \cdot \mathrm{d}\mathbf{S}\}}{\frac{1}{2}\mathrm{Re}\{\int_{A_1} \mathbf{E}^*_{vac}(\mathbf{r},\omega) \times \mathbf{H}_{vac}(\mathbf{r},\omega) \cdot \mathrm{d}\mathbf{S}\}} \tag{4.1}$$

where A_1 is the flux plane corresponding to '1', and the minus sign in the numerator is there to make the reflected flux positive. This expression can be shown to simplify to

$R(\omega) = [\Phi_1^{vac}(\omega) - \Phi_1^{slab}(\omega)]/\Phi_1^{vac}(\omega)$ where the flux plane closer to the light source is '1', and the flux plane further from the light source is '2'. (One can show that the numerator becomes $\Phi_1^{vac}(\omega) - \Phi_1^{slab}(\omega) + \frac{1}{2}\mathrm{Re}\{\int_{A_1}(\mathbf{E}_{vac}^* \times \mathbf{H}_{ref} - \mathbf{H}_{vac} \times \mathbf{E}_{ref}^*) \cdot \mathrm{d}\mathbf{S}\}$ but the cross term vanishes for incoming and outgoing plane waves in vacuum, for which $\mathbf{E}$ and $\mathbf{H}$ are proportional.) Similarly, the transmittance is given by $T(\omega) = \Phi_2^{slab}(\omega)/\Phi_2^{vac}(\omega)$ and the absorbance is simply $A(\omega) = 1 - R(\omega) - T(\omega)$. This way, we obtain reflectance, transmittance and absorbance spectra for PhC slabs. We incorporate absorption into our simulations by means of the Drude model, according to the following equation:

$$\epsilon(\omega) = \epsilon_\infty + \frac{\sigma}{(\omega_0^2 - \omega^2 - i\gamma\omega)} \tag{4.2}$$

where ϵ_∞, γ, ω_0 and σ are input parameters. In our case, we are concerned with metals, for which $\omega_0 = 0$. By Kirchhoff's law, the absorbance spectra so calculated are identical to the emittance spectra of these objects, for each polarization, frequency and observation angle.

4.3 Holes and dips

Let us now turn our attention to real systems and the physical effects that are manifested therein. The goal is to develop an understanding of the physical processes that drive emittance in these systems. The first structure we will examine is a simple metal slab with holes (see Fig. 4-1). If we illuminate the structure with light incident from the top of the cell, the light propagates down the holes which act as metallic waveguides. Waveguide cut-offs arise from the requirement that the parallel component of the electric field be continuous across a boundary. Inside a perfect metal, the electric field is strictly zero. For such a material, $E_\parallel$ is constrained to vanish at the surface, and this leads to the well-known cut-off frequency corresponding to a half-wavelength oscillation. Below this frequency, no propagating mode can be supported within the waveguide, because the boundary condition cannot be satisfied. For a realistic metal (i.e. one that permits some penetration of fields), the fields are not required to exactly

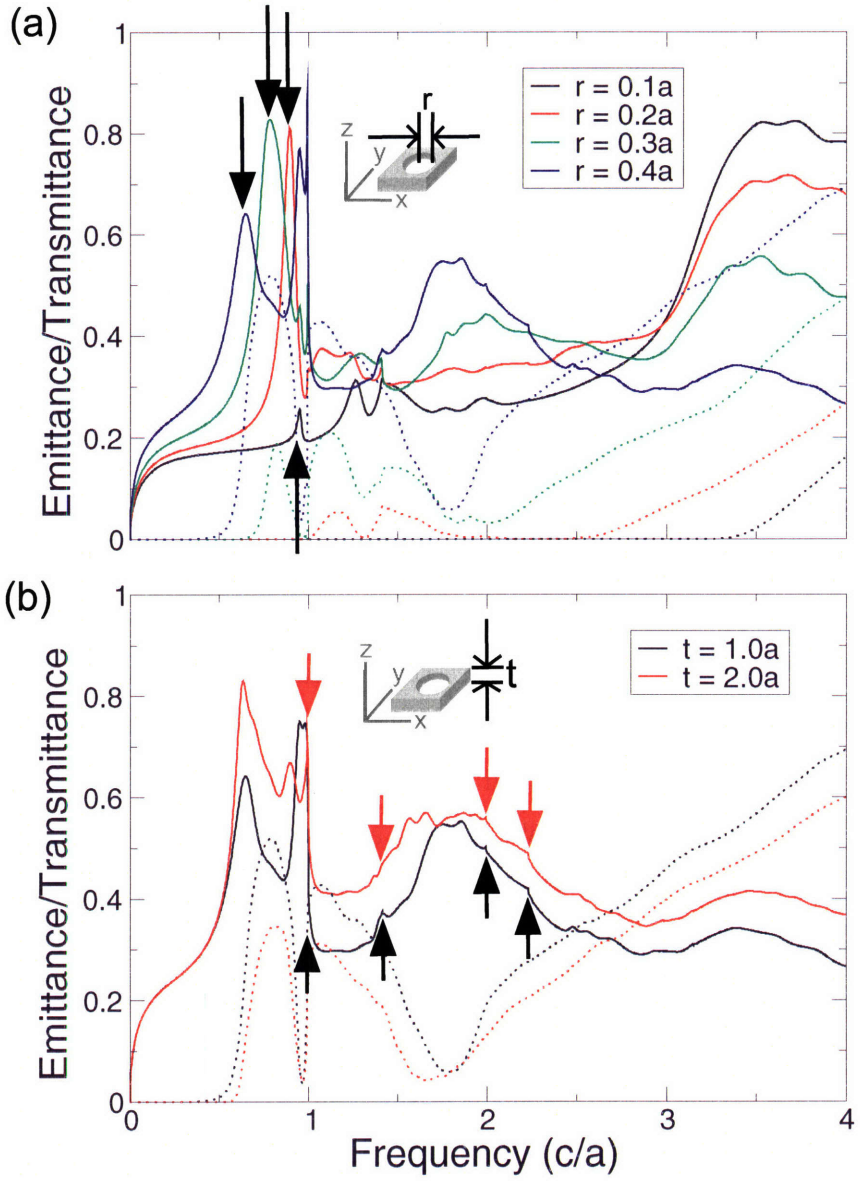

Figure 4-1: (Color) Here we show emittance (solid lines) and transmittance (dotted lines) spectra for a 2D-periodic metal slab with circular holes, viewed at normal incidence and for y-polarized light. The Drude parameters used for the metal are $\epsilon_\infty = 1$, $\omega_0 = 0$, $\gamma = 0.3(2\pi c/a)$ and $\omega_p = \sqrt{10}(2\pi c/a)$. In Panel (a), we fix the thickness of the slab at $1.0a$ (where a is the lattice constant of the slab) and vary the radius of the holes. The black arrows indicate the peaks produced by the waveguide cut-off in the x-direction. In Panel (b), we keep the hole radius constant at $0.4a$ and vary the thickness of the slab. Here, we use arrows to indicate the peaks produced by diffraction.

vanish at the surface, but must decay away rapidly and exponentially once inside the material. Such boundary condition matching leads to a similar cut-off as in the case of the perfect metal, except that the penetration of field into the metal produces a cut-off with a slightly lower frequency, because the *effective* width of the waveguide is slightly larger. Cut-off frequencies depend on the width of the waveguide. The wider the waveguide, the lower the cut-off frequency.

We present emittance and transmittance spectra for this system. Fig. 4-1a shows how the spectra change with hole radius. The peaks below 1.0 (indicated by black arrows) are waveguide cut-offs arising from propagation of light through the holes. These peaks decrease in frequency with increasing radius, a clear signature of waveguide cut-offs. They correspond to modes that fit approximately half a wavelength across the hole in the x-direction. As we discussed, the electric field has to be continuous as we cross media boundaries in the x-direction (because E_y is parallel to the media boundary) but not in the y-direction. Thus, these modes have one 'hump' as we cross the holes in the x-direction, and decay exponentially inside the metallic bulk between holes such that the field profile within the metal is of the form of a hyperbolic sine/cosine curve (a combination of a decaying and growing exponential), depending on parity. We can see immediately that as we increase the radius of such a hole, the profile relaxes in the x-direction in such a way as to make the hump wider. This leads to a larger effective x-wavelength for the mode, and thus a lower frequency cut-off. (The wavelength in the y-direction is unaffected by the radius of the hole, since E_y is not required to be continuous in the y-direction.)

Diffraction peaks occur when we consider the slab system at a macroscopic level, in terms of incoming and outgoing radiation modes. This effect is not unique to metallic PhCs, and can be observed in non-metallic PhCs as well. In terms of absorption, the incident light, being normal, can couple into outgoing radiation modes (in transmission or reflection) that conserve the wave vector up to a reciprocal lattice vector in a direction of discrete periodicity. Because the incident light has no $k_{transverse}$ component, it can couple into outgoing modes with $k_{transverse}$ equal to an integer multiple of $2\pi/a$ (i.e. 1 in our units). This means that as we increase the

frequency of the incoming radiation, a new diffraction direction will be coupled into at $\omega = 1, \sqrt{2}, 2, \sqrt{5}...$, corresponding to $(k_x, k_y) = (1,0), (1,1), (2,0), (2,1)...$ At the threshold frequency for a new diffraction mode, the wave vector has no k_z component, and so $\mathbf{k}$ is parallel to the surface of the slab. Such 'grazing' modes have maximum interaction with the slab because they travel close to the surface of the metal, and as such are strongly absorbed by the material. These absorption peaks translate into emission peaks, via Kirchhoff's law, so we would expect to see emission peaks for modes corresponding to $\omega = |k| = 1, \sqrt{2}, 2, \sqrt{5}...$

Fig. 4-1b shows how emittance and transmittance change with the thickness of the metal slab. First, we notice that transmittance is greater for the thinner slab, as one would expect. Second, we see the emergence of diffraction peaks at $1, \sqrt{2}, 2$ and $\sqrt{5}$ (we indicate these with red and black arrows). Not only do they occur at precisely those frequencies that correspond to the root of the sum of two squares (their wave vectors being permutations of (1, 0), (1, 1), (2, 0) and (2, 1), respectively), they are also the same for both black and red curves, lending further weight to the argument that they are diffraction peaks. Their magnitudes are clearly quite variable; indeed, they wash out at higher frequencies. Such diffraction peaks can be seen in Fig. 4-1a, too.

What happens if we take the same metal slab, but do not drill holes in the slab that go all the way through? What happens if, instead of having circular holes, we have circular *dips*? We present emittance and transmittance for this structure in Fig. 4-2 as a function of dip radius. Again, we see peaks below 1.0 which correspond to cut-offs, except in this case they are not waveguide cut-offs but a kind of 'cavity' cut-off, where k_x is such that there is approximately half a wavelength in the x-direction. We see diffraction peaks at $1, \sqrt{2}, 2$ and $\sqrt{5}$. Above $\omega_p = \sqrt{10} \approx 3.16$, the plasmon frequency of the metal, transmittance becomes significant, because above that frequency, the metal becomes transparent and light can pass through it as though it were a dielectric material (while still being subject to some absorptive loss).

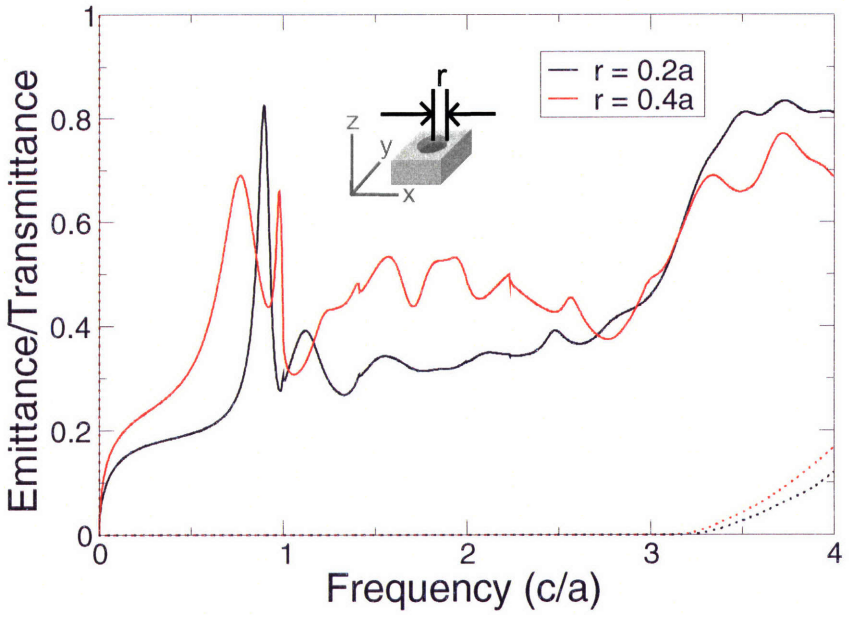

Figure 4-2: (Color) We show emittance (solid lines) and transmittance (dotted lines) spectra for a 2D-periodic metal slab of thickness $1.0a$ with circular dips, observed at normal incidence and y-polarization. The dips have a depth of $0.5a$. The Drude parameters used are $\epsilon_\infty = 1$, $\omega_0 = 0$, $\gamma = 0.3(2\pi c/a)$ and $\omega_p = \sqrt{10}(2\pi c/a)$. We show spectra for two different radii of dips, keeping the slab thickness constant.

4.4 Hybrid structures

Let us now turn our attention to hybrid structures which involve both metal and dielectric. We consider a metal slab with a circular dielectric puck on top. This puck is intended to be a small perturbation to the system that introduces discrete periodicity in both the x- and y-directions by means of a piece of dielectric. We observe emitted light at normal incidence and polarized in the y-direction.

Fig. 4-3a shows how emittance and transmittance vary with the dielectric constant of the perturbation (ϵ). First, we observe many peaks in the emittance spectra, and we note that the positions of some these peaks (particularly the ones at frequencies less than 2.0) decrease with increasing ϵ. Second, we see zero transmittance in the system for frequencies below $\omega_p \approx 3.16$, as we expect, because the metal is opaque at frequencies below the plasmon frequency. Third, we see also an entire series of diffraction peaks, at frequencies 1, $\sqrt{2}$, 2, $\sqrt{5}$, $2\sqrt{2}$ and 3, corresponding to modes with wave vectors (1, 0), (1, 1), (2, 0), (2, 1) and permutations thereof. These are especially clearly seen on the black curve. We know they are diffraction peaks because they not only fit the above sequence, but also have the same frequencies on the red and green curves. (Diffraction peaks do not change with the dielectric constants of the structure.) Fourth, we demonstrate that most of the emittance peaks with frequencies below 2.0 that we see in Fig. 4-3a are in fact produced by surface plasmons.

Surface plasmons (SPs) are excitations that exist on the interface between a plane-metal and a dielectric. They are confined to the surface, but can propagate freely within that surface. They have a relatively simple dispersion relation that is approximately linear at low wave vectors and bends over toward a flat cut-off at higher wave vectors ($\omega_p/\sqrt{\epsilon+1}$ is the cut-off frequency, where ω_p is the plasmon frequency and ϵ is the dielectric constant). If the direction of propagation is x (i.e. $\mathbf{k}$ is in the x-direction), then the SP will have field components E_x, E_z and H_y (the z-direction is normal to the interface). The SP is unusual in that it has an electric field component in the direction of propagation. Normally incident light (for which $k_{transverse} = 0$) cannot couple into SP modes with non-zero k because of conservation of wave vec-

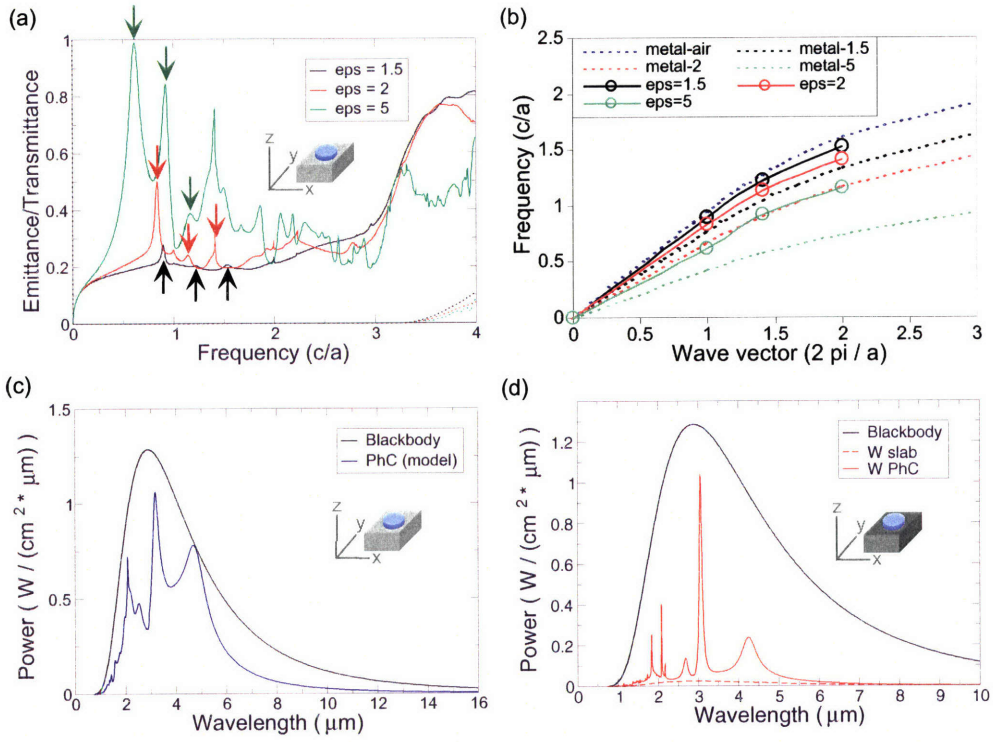

Figure 4-3: (Color) Panel (a) shows emittance (solid lines) and transmittance (dotted lines) spectra for a 2D-periodic metal slab of thickness $1.0a$ with circular dielectric pucks for normal incidence and light polarized in the y-direction. The pucks have a radius of $0.4a$ and a thickness of $0.2a$. The Drude parameters used for the metal are $\epsilon_\infty = 1$, $\omega_0 = 0$, $\gamma = 0.3(2\pi c/a)$ and $\omega_p = \sqrt{10}(2\pi c/a)$. We show spectra for three different dielectric constants for the circular puck. In Panel (b), we took the peaks labeled by arrows in Panel (a), and plotted them on a dispersion curve. (Note that the third red peak in Panel (a) coincides with a diffraction peak at frequency $\sqrt{2} \approx 1.41$.) We see that the dispersion of the peaks (lines with circles) lies between the metal-air dispersion and the metal-dielectric dispersion, for the corresponding dielectric constant. Therefore, it is quite plausible that these peaks are produced by surface plasmon modes. In Panel (c), we show the thermal emission spectrum for the same metal slab with pucks of dielectric constant $\epsilon = 5$ at temperature 1000K (we call it "PhC (model)"). We also show the blackbody spectrum at that temperature for comparison. The lattice constant was chosen to be $a = 2.94\mu m$. Panel (d) shows the thermal emission spectrum for the same system except that the "model" metal has been replaced by tungsten. We modeled tungsten with Drude parameters[55] $\epsilon_\infty = 1$, $\omega_0 = 0$, $\gamma/(2\pi c) = 487cm^{-1}$ and $\omega_p/(2\pi c) = 51700cm^{-1}$, and we chose $a = 2.94\mu m$. We show the emission spectra for a uniform tungsten slab of thickness a (without pucks) and a blackbody for comparison.

tor; however, it *can* couple into such modes if the wave vector of the SP is along a direction of discrete translational symmetry, because in such a direction, wave vector is conserved only up to an integer multiple of the reciprocal lattice vector. These correspond to $\mathbf{k} = (m, n)(2\pi/a)$ where m and n are integers.

To show that the emittance peaks with frequencies below 2.0 are indeed SPs, we record the frequencies of the peaks (up to $\omega_p/\sqrt{\epsilon + 1}$, the SP cut-off) for each curve in Fig. 4-3a, and plot them as circles in Fig. 4-3b against wave vector magnitude, making the assumption that the first peak has a wave vector of (0, 1), the second a wave vector of (1, 1), and the third a wave vector of (0, 2) (all in units of $2\pi/a$). We make this assumption because this sequence of $(k_x, k_y) = (m, n)$ produces a sequence of frequencies in ascending order. In addition, we plot SP dispersion curves for metal-air and metal-dielectric structures where both media are semi-infinite in extent (dotted lines). SP modes in the structure under consideration would therefore be expected to have a dispersion relation that lies between the metal-air and the metal-dielectric dispersions, since the average dielectric constant of the dielectric strip/air lies between that of the air and the dielectric. Thus, we would expect the black circles to lie between the dotted black and blue curves, the red circles to lie between the dotted red and blue curves, and so on. Indeed, this is exactly what we see. Furthermore, the fact that the circles, when joined together by solid lines, form a dispersion relation that clearly bends over toward a cut-off, gives us confidence in identifying these modes as SPs.

We can obtain the emissive power of these structures by taking the emittance spectra that we have calculated and multiplying them by the blackbody emission spectrum (which is also known as the Planck distribution). This is what we did in Fig. 4-3c. We chose $a = 2.94\mu m$ and plotted thermal emission of the PhC slab as a function of wavelength. We show the emission spectrum of a blackbody for comparison. We can immediately see an emission peak near $4.7\mu m$ that has as high emission as a blackbody; this peak corresponds to the first SP peak in Fig. 4-3a. The two emission peaks at approximately $2.1\mu m$ and $3.2\mu m$ are diffraction and SP peaks, respectively.

In Fig. 4-3d, we consider the same structure except that the "model" metal slab is now replaced by a tungsten slab. We did this by doing the calculation using the Drude parameters of tungsten[79, 1, 56, 55]. We also plot the equivalent tungsten slab emittance (dashed red curve) for comparison. In keeping with Kirchhoff's law, at no point does the emission of the PhC structure exceed that of a blackbody. The qualitative similarities between this emission spectrum and that shown in Fig. 4-3c can be traced quite easily: the three major peaks remain; the tall central peak and the peak to its right are SPs, while the sharp peak to the left (around $2\mu m$) comes from diffraction into (1, 1) modes. Overall, the background emission of the tungsten PhC slab is lower than that for the "model" metal that we have hitherto been studying, because the background emittance of a slab[48] goes as $2\gamma/\omega_p$ (in regime $\gamma < \omega < \omega_p$), and ω_p is much higher for tungsten than for the Drude metal in Fig. 4-3c. Notice that the PhC tungsten slab has higher emission at *all* frequencies than the uniform tungsten slab. Thus, we have excellent enhancement of emissive power through the use of a PhC.

As we have already remarked, the dominant feature of the emission characteristics of this structure is the central peak at $3.06\mu m$, which achieves 80% of the emission of a blackbody. As we will show in the next figure, it is possible to shift this peak by changing the lattice constant of the structure. By so doing, we can place a strong emission peak at whatever frequency we choose. If we combine copies of this structure with different lattice constants, we can place strong emission peaks at multiple frequencies. This is the beginning of thermal design using 2D-periodic metallic PhC slabs.

4.5 Thermal design

In order to facilitate our discussion of thermal design in 2D-periodic metallic photonic crystals, we turn our attention to another variation on the theme of a hybrid structure, and show how the emission spectrum of this structure can be tailored to our needs. We study a tungsten slab on top of which sits a dielectric slab with circular holes.

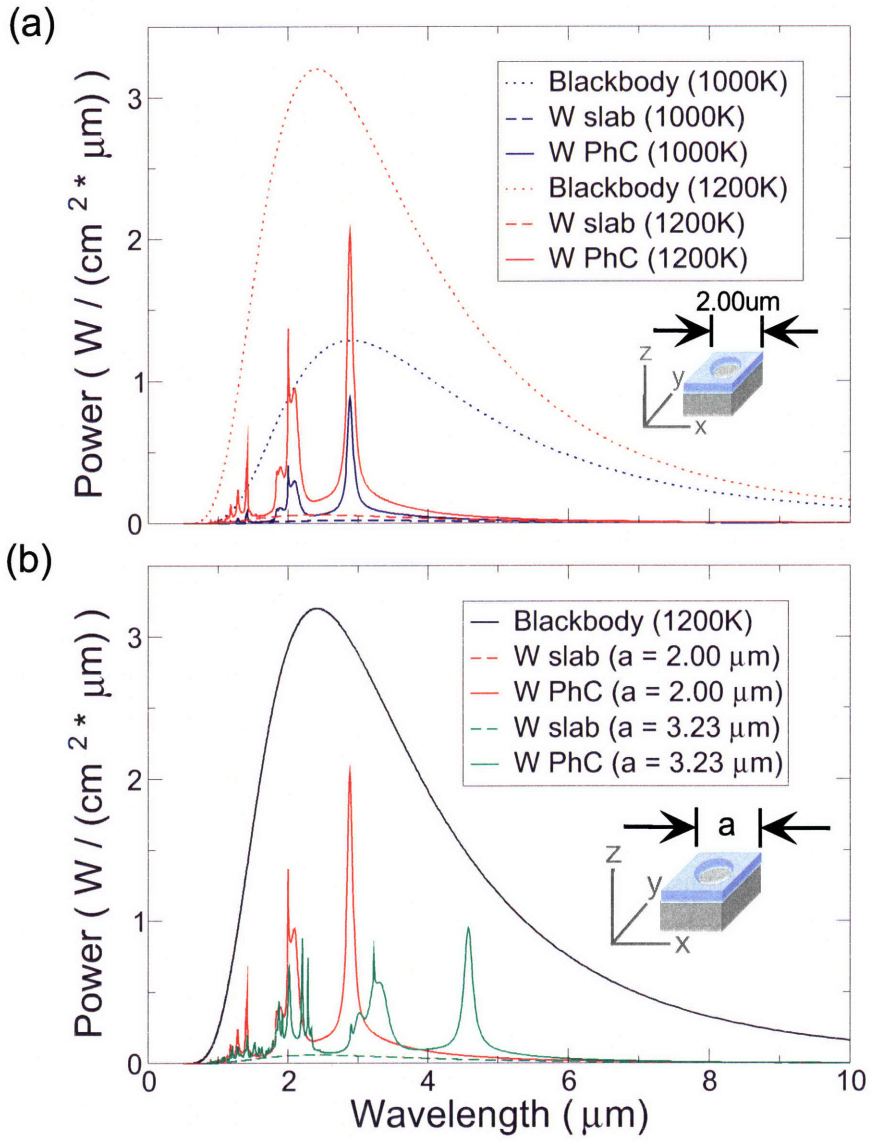

Figure 4-4: (Color) Here we show the thermal emission spectrum for a hybrid 2D-periodic structure consisting of a tungsten slab and a dielectric slab with holes. The metal slab is $1.0a$ thick while the dielectric slab ($\epsilon = 5$) is $0.2a$ thick with holes of radius $0.4a$. We show emission of light polarized in the y-direction. In Panel (a), we display emission at two different temperatures. We chose a lattice constant of $a = 2.00\mu m$. In Panel (b), we show how the emissive power changes with lattice constant. In both panels, we show emission spectra for a uniform tungsten slab of thickness a without dielectric, and a blackbody, for comparison.

One can think of the dielectric portion of this structure as being the 'inverse' of the circular puck. Such a structure exhibits discrete periodicity in both the x- and y-directions.

We show the emission spectrum for such a structure in Fig. 4-4. In Panel (a), we choose $a = 2.00\mu m$ and vary the temperature of operation. We plot thermal emission for the PhC slab, the unadorned tungsten slab, and a blackbody. Again, the PhC emission far exceeds that of a uniform tungsten slab. We see three prominent groups of peaks, the smallest of which has fairly complicated substructure. First, we notice that the positions of the peaks do not change with temperature. Second, increasing temperature increases emission at *all* wavelengths. Emissive power goes as T^4 (Stefan's law), so that, going from 1000K to 1200K, emission increases by a factor of $(1.2)^4 \approx 2.07$ (provided the weighting does not change significantly). Third, the relative weighting given to different wavelengths changes with temperature, because the peak of the Planck distribution shifts toward lower wavelengths with increasing temperature. In our case, the group of small peaks between 1 and $2\mu m$ were insignificant features at 1000K, but became more prominent at 1200K, because the blackbody spectrum shifted in such a way as to give those peaks much more weight than before (thus, they were enhanced by more than a factor of 2.07). Fourth, the emission of the PhC slab exceeds that of the uniform slab at all wavelengths and at all temperatures. In fact, the enhancement is impressive: we see a 20-fold increase in emissive power (over that of a slab) at the major peak at around $2.9\mu m$. Of course, emissivity never exceeds unity, because that would violate the Second Law of Thermodynamics (the large peak in question attains 66% emissivity). The important lesson we learn from this is that we can emphasize different parts of the emission spectrum of a PhC by changing the temperature at which we operate the thermal structure.

In Fig. 4-4b, instead of changing the temperature, we keep temperature fixed and vary the lattice constant of the PhC. The blackbody envelope and the emission spectrum of a uniform slab of this same metal are shown for comparison. We see that increasing the lattice constant shifts the emission peaks in the PhC towards a higher

wavelength. In our case, for $a = 2.00\mu m$, the large peak is already close to the point of maximum blackbody emission, so that increasing the lattice constant to $a = 3.23\mu m$ only served to decrease the total emission from that excitation (incidentally, it is a surface plasmon). However, the change in a also brought some small peaks from the lower wavelengths into the picture. The point of this exercise is to illustrate the degree of control we have over the position of the peaks, and by these simple techniques, we can shift emissive power around to different parts of the spectrum. It is useful to note that for both choices of a, there is significant enhancement of emission over that of a uniform slab because the breaking of continuous translational symmetry allows more wave vector modes to be excited and coupled into.

The two hybrid structures we considered in this and the previous sections would be suitable candidates for applications that require narrow band emission in one or more frequencies. Both structures have a dominant peak that can be shifted in wavelength by changing the lattice constant. If we want three emission bands separated by 1-2μm, the structure in Fig. 4-4 would be a good choice. There are two different ways to amplify an emission peak relative to background emission. We can choose to operate the structure at different temperatures, or we could change the lattice constant. These are simply two different ways of making the emission peak coincide with the wavelength of maximum blackbody emission. By combining many such hybrid structures, each with its own lattice constant, we can place strong emission peaks at whichever wavelengths we choose. We therefore have a means of tailoring the thermal emission properties of a hybrid structure to our needs.

4.6 Conclusion

We presented a physical and intuitive framework within which we can understand some of the physical phenomena that drive thermal emission in 2D-periodic metallic photonic crystal slabs. We performed detailed numerical calculations for these systems, and found that periodicity played a key role in determining the types of physical phenomena that can be excited. In particular, we saw how periodicity gave

rise to waveguide cut-offs, waveguide resonances, diffraction peaks and surface plasmon modes. Using hybrid structures composed of metal and dielectric components, we obtained sharp emission enhancement over and above that of a metal slab. In the case of tungsten, we created strong emission peaks with 80% and 66% emissivity, far exceeding that of a uniform tungsten slab, which plateaus at about 3-4%. These peaks could be shifted at will by changing the lattice constant of the structure or by changing the temperature at which the structure is operated. We can design materials with multiple emission peaks by combining hybrid structures, each with its own lattice constant. Thus, we have a powerful set of tools with which to develop physical intuition and understanding for thermal design. The ability to design thermal emission could well find uses in thermophotovoltaic systems and defense applications, where many targeting systems rely on the detection of thermal emission from projectiles.

Chapter 5

Emulating 1D resonant scattering behavior in a 2D system via Fano resonances

We establish that the significant enhancement of thermal emission via Q-matching, which has been possible in 1D systems only, can be extended to 2D systems by means of Fano resonances in the 2D system. In particular, we show the existence of essentially 1D behavior in a 2D system — a case of reduced dimensionality. We demonstrate through detailed numerical and analytical studies that the Fano resonances characteristic of 2D-periodic photonic crystal slabs can be understood in terms of a 1D-model. Moreover, we show how properties of these spectra can be controlled by changing the geometrical parameters of the photonic crystals. Therefore, this work provides a path to the creation of graybodies that have tailored thermal emission spectra, with highly unusual properties.

5.1 Introduction

A blackbody is defined as an object of perfect absorption. Its entropy is maximized, and in that sense it exemplifies utter disorder. The physics of blackbodies has both fascinated and intrigued scientists for well over a century now[59]; properties of their

thermal emission provided one of the most important clues for the discovery of quantum mechanics. In practice, most objects have only finite absorption, and are thus referred to as 'graybodies'. Graybodies are of interest because their thermal emission spectra can be changed by altering the geometry of the system or the materials used. Most black/graybodies have certain generic features in common, many of which are captured in Fig. 5-1a.

The ability to modify or tailor the thermal emission profile of an object is of great importance and interest in many areas of applied physics and engineering. It has been noted recently that periodic sub-wavelength scale patterning of metallo-dielectric systems, i.e. photonic crystals, can modify their emission spectra in interesting ways[44, 7, 41, 17, 69, 22, 45, 46, 68, 48, 23]. Researchers studying 1D-periodic photonic crystals have come up with ways to control emission spectra[70, 14, 54], demonstrate the coherence of emitted light[25, 39], and enhance thermal emission via resonant cavities[11]. Thermal radiation from 2D-periodic photonic crystals has been studied within the contexts of spectral and directional control[51, 69, 61, 16], guided resonances[19], thermophotovoltaic generation[68], resonant scattering[58, 15], laser action[50], Kirchhoff's law[48] and spontaneous emission enhancement[7, 17, 61]. And most recently, Laroche *et al.*[38] predicted coherent thermal emission due to leaky surface waves in truncated photonic crystal structures.

The body of work on enhancement of emission via resonant cavities will interest us the most. It turns out that the idea of matching the radiative Q-factor of a system with its absorptive Q-factor in order to enhance emission, as in Eq. (2) in [11], is fundamentally a one-dimensional one. It is reducible to the problem of having one input channel, a resonant cavity, and one output channel. In such a setup, light emitted by the resonant cavity and the incident light interfere in such a way as to extremize the net outgoing wave. This complete cancellation of waves from the cavity and the incident/outgoing beam is unique to the one-dimensional world. Thus, enhancement via Q-matching, an essentially 1D phenomenon, would not be expected to work in a general 2D system with multiple input/output channels.

In this chapter, we show that enhancement of thermal emission via Q-matching,

which is usually observed in 1D systems only, can be extended to 2D systems by coupling into Fano resonances[19] (arising from bulk guided modes of an otherwise uniform slab) in the 2D system. This mechanism is different from all those described above. In particular, we show the existence of essentially 1D behavior in a 2D system — a case of reduced dimensionality. We demonstrate through detailed numerical and analytical studies that the Fano resonances characteristic of 2D-periodic photonic crystal slabs can be understood in terms of a 1D-model based on Q-matching. Moreover, we show how properties of these spectra can be controlled by changing the geometrical parameters of the photonic crystals.

5.2 Fano resonances in photonic crystals

A photonic crystal (PhC) slab with a 2D-periodic array of holes gives rise to a number of Fano resonances [19], as shown in Fig. 5-2a. The way to understand these resonances is to note that radiation incident from the surrounding low-ϵ medium cannot couple into the guided modes of a uniform high-ϵ slab with continuous in-plane translational symmetry because of conservation of in-plane (transverse) wave vector. However, when the slab is punctuated with a periodic array of holes, dips or other such perturbations, the transverse wave vector is now conserved only up to a reciprocal lattice vector, and coupling between the incident radiation and the guided modes of the slab is possible. The interaction between the guided modes and the incident radiation manifests itself in the form of very sharp peaks in the transmission spectrum (shown in Fig. 5-2a), called Fano resonances. Fano resonances show up in both transmission and absorption as high-Q states on top of an otherwise undulating background of Fabry-Perot resonances from the slab; this kind of undulating background would occur even if the slab were uniform. In the case of no absorption, the transmission peaks would go all the way up to 1 and all the way down to 0, but with absorption, they are rounded out somewhat, though their frequencies remain essentially the same; the frequencies are determined by the frequencies of the modes of the corresponding transverse wave vector of the PhC slab. As can be seen from

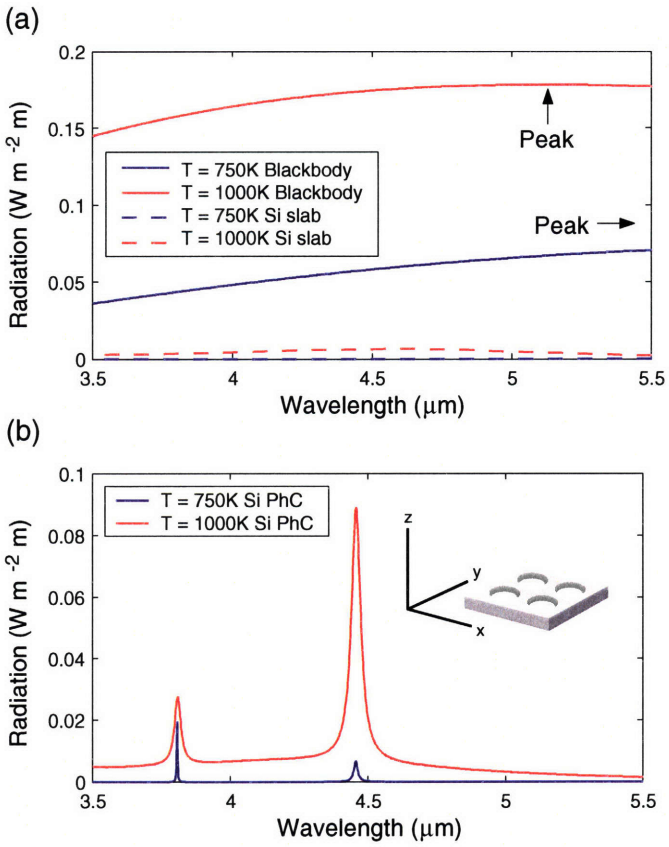

Figure 5-1: (Color) Panel (a) shows some generic features associated with thermal radiation of common black/graybodies into air (the case of a perfect blackbody is denoted by solid lines, while an example of a graybody, a uniform Si slab of thickness $0.75\mu m$, is denoted by dashed lines); plotted is the thermal radiation intensity/$dk_x dk_y d\lambda$ for an exemplary case: $k_x = 0.838\mu m^{-1}$ and $k_y = 0$. First, black/graybodies have perfectly incoherent and ultra-broad bandwidth thermal emission spectra. Next, as the temperature of such a body increases, the emission spectrum shifts to shorter wavelengths. Finally, bodies with lower absorption have weaker thermal emission; for example, a thin silicon slab is nearly transparent for infra-red light even at fairly high temperatures, so its thermal emission is very weak. Panel (b) shows FDTD calculations of the thermal emission spectra of the same Si slab as in Panel (a), but this time patterned as a square-lattice 2D-periodic photonic crystal slab of holes with radius $r = 0.3\mu m$, and lattice constant $a = 1.5\mu m$ (structure schematic shown in inset). Thermal radiation of such a body can display drastically different behavior than the one shown in Panel (a). First, a photonic crystal can produce very coherent thermal radiation, as implied by the narrowness of the emission peaks. Next, as one increases the temperature, the peak emission can shift to longer (instead of shorter) wavelengths. Finally, despite the near-transparency of Si, emissivity can be comparable to that of a perfect blackbody for certain frequencies.

Fig. 5-2b, as one increases the angle of incidence (k_x), some resonances increase in frequency while others decrease. Still others remain unchanged (these are flat bands).

Turning a closer attention to the absorption spectrum in Fig. 5-2a, we observe first of all that the background absorption of the slab is very low, in the region of 2-3%. However, of more interest are the strong absorption peaks on top of the background, in some cases reaching 50%. This illustrates how greatly Fano resonances can enhance absorption over and above that for the slab. Now, Kirchhoff's law states that emissivity and absorptivity are equal, meaning that for Fano resonance frequencies the *emissivity* of the PhC slab can approach that of a perfect blackbody.

5.3 Analytical modeling

To identify the important physical parameters of the system and their relationship to PhC emissivity, we study the behavior of Fano resonances within a framework of coupled-mode theory[28]. A 2D PhC slab exhibits two dominant mechanisms for electromagnetic wave transmission. The first transmission mechanism is the direct transmission path through the slab, as in the case of a uniform slab. The second mechanism is the resonant coupling to the guided modes of the slab by means of Fano resonances; this produces sharp peaks in the transmission and reflection spectra. Therefore, transmission can be understood as the superposition of a direct transmission path (represented by a slowly-varying envelope in frequency) and a Lorentzian-type oscillator transfer function for each of the Fano resonances. This is analogous to treating the system as a waveguide with a side-coupled cavity and partially-reflecting mirrors. Waveguide-resonator systems have been studied using scattering theory, coupled-mode theory and perturbation theory[81, 21, 18, 72, 83, 84, 73].

We now derive transmission and reflection coefficients for Fano resonances in a lossy medium. For the benefit of the reader unfamiliar with coupled-mode theory we outline some of the key steps in the analysis. Consider a 2D PhC slab surrounded by air. We label the two sides 1 and 2, and define s_{+i} as the incident wave amplitude from air on side i and s_{-i} as the reflected wave amplitude leaving side i. Using

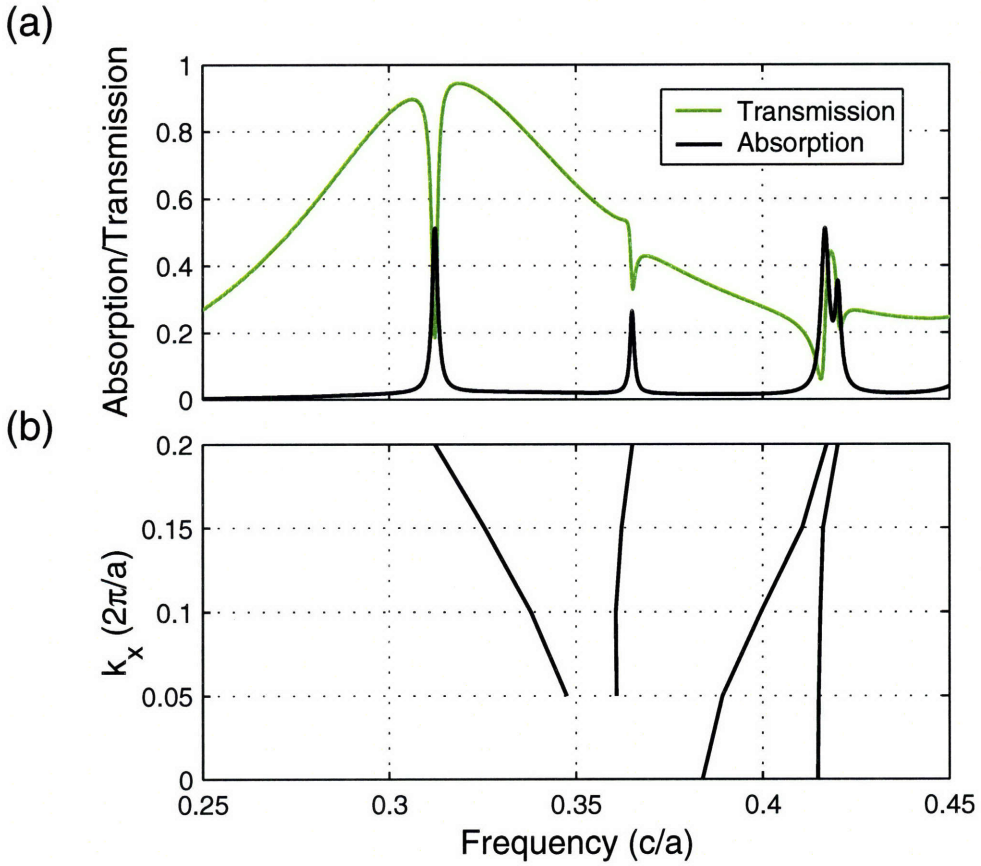

Figure 5-2: (Color) FDTD simulations of a photonic crystal slab (PhC) of thickness $0.5a$ with $\mathrm{Re}(\epsilon) = 12$ for incident electric field polarized in the y-direction. (a) Transmission and absorption spectra for PhC slab, for $k_x = 0.2(2\pi/a)$, with $\mathrm{Im}(\epsilon) \approx 0.005$ (chosen to maximize absorption for the first peak), displaying 4 Fano resonance peaks. (b) Band diagram of the photonic crystal slab modes in the case of an infinitesimally small amount of absorption. Note that Fano resonances in Panel (a) occur exactly at those frequencies for which there is a guided mode of the PhC that has $k_x = 0.2(2\pi/a)$.

coupled-mode theory, we can write down three equations that describe this system:

$$\frac{da(t)}{dt} = i\omega_0 a(t) - \left(\frac{1}{\tau_{rad}} + \frac{1}{\tau_{abs}}\right) a(t) + \sqrt{\frac{1}{\tau_{rad}}}\kappa s_{+1}(t)$$

$$s_{-2}(t) = t_{slab} s_{+1}(t) + \sqrt{\frac{1}{\tau_{rad}}}\kappa a(t)$$

$$s_{-1}(t) = r_{slab} s_{+1}(t) \pm \sqrt{\frac{1}{\tau_{rad}}}\kappa a(t)$$

where $a(t)$ is the amplitude of the resonant mode, ω_0 is the resonant frequency, τ_{rad} is the cavity mode lifetime in the case of no absorption, $1/\tau_{abs}$ is the decay rate due to material absorption, κ is the coupling constant, $s_{+1}(t)$ is the incoming wave amplitude, $s_{-1}(t)$ is the reflected wave amplitude, $s_{-2}(t)$ is the transmitted wave amplitude and r_{slab} and t_{slab} are the reflection and transmission coefficients, respectively, of the planar slab without any holes. Note that r_{slab} and t_{slab} are complex functions that incorporate the phase change upon transmission and reflection. In this set up, we do not have an incoming wave on the other side ($s_{+2} = 0$).

The first equation says that the rate of change of the resonant mode complex amplitude depends on the resonant frequency (responsible for phase oscillations), the decay rates ($1/\tau_{rad}$ and $1/\tau_{abs}$), and the coupling to the incoming wave, which causes the resonant mode amplitude to grow. The second equation states that the transmitted amplitude is equal to t_{slab} times the incident amplitude (including a phase) plus a coupling to the cavity mode. Similarly, the third equation states that the reflected amplitude is equal to r_{slab} times the incident amplitude, plus a coupling to the cavity mode. Note that there is a $\pm$ sign in front of the a term: this takes into account the fact that the cavity mode may have even or odd parity. Even parity, defined here with the $+$ sign, indicates that the contribution of the a term to the reflected and transmitted amplitudes are in phase with each other. Odd parity, represented by the $-$ sign, is the opposite: the contribution of the cavity mode to reflection is π out of phase with its contribution to transmission. Of course, we could just as easily have put the $\pm$ sign in the transmission equation; the net effect of such

a change would be to shift the absolute phase of a by π, a change that has no physical significance.

Using a complex exponential form as an ansatz for a, with frequency ω, yields

$$a(\omega) = \frac{\sqrt{\frac{1}{\tau_{rad}}}\kappa s_{+1}(\omega)}{i(\omega - \omega_0) + \frac{1}{\tau_{rad}} + \frac{1}{\tau_{abs}}}$$

It is now straightforward to write down equations for the transmission and reflection coefficients of the photonic crystal slab:

$$t_{PhC}(\omega) \equiv \frac{s_{-2}(\omega)}{s_{+1}(\omega)} = t_{slab} + \frac{\kappa^2 \frac{1}{\tau_{rad}}}{i(\omega - \omega_0) + \frac{1}{\tau_{rad}} + \frac{1}{\tau_{abs}}} \tag{5.1}$$

$$r_{PhC}(\omega) \equiv \frac{s_{-1}(\omega)}{s_{+1}(\omega)} = r_{slab} \pm \frac{\kappa^2 \frac{1}{\tau_{rad}}}{i(\omega - \omega_0) + \frac{1}{\tau_{rad}} + \frac{1}{\tau_{abs}}} \tag{5.2}$$

There are two conditions we can impose in order to calculate κ^2. The transmission, reflection and absorption coefficients for the 2D PhC slab have to satisfy conservation of energy: $|a_{PhC}|^2 + |t_{PhC}|^2 + |r_{PhC}|^2 = 1$. The same is true for the planar dielectric slab without holes: $|a_{slab}|^2 + |t_{slab}|^2 + |r_{slab}|^2 = 1$. These two equations, combined with Eqs. (5.1) and (5.2), can only be satisfied simultaneously if $\kappa^2 = -(t_{slab} \pm r_{slab})$. (One can derive this relation by considering the lossless case, where $|a_{PhC}| = |a_{slab}| = 0$ and $1/\tau_{abs} = 0$.) Substituting this into Equations (5.1) and (5.2) gives the final form for Fano resonances in lossy media:

$$t_{PhC} = t_{slab} - \frac{(t_{slab} \pm r_{slab})\frac{1}{\tau_{rad}}}{i(\omega - \omega_0) + \frac{1}{\tau_{rad}} + \frac{1}{\tau_{abs}}} \tag{5.3}$$

$$r_{PhC} = r_{slab} - \frac{(r_{slab} \pm t_{slab})\frac{1}{\tau_{rad}}}{i(\omega - \omega_0) + \frac{1}{\tau_{rad}} + \frac{1}{\tau_{abs}}} \tag{5.4}$$

One can repeat the above derivation for multiple Fano resonances. The general result is complicated, although it simplifies in the case of two resonances that are of opposite

parity. If the first resonance is even and the second odd, then

$$t_{PhC} = t_{slab} - \frac{(t_{slab} + r_{slab})\frac{1}{\tau_1}}{i(\omega - \omega_{01}) + \frac{1}{\tau_1} + \frac{1}{\tau_{abs1}}} - \frac{(t_{slab} - r_{slab})\frac{1}{\tau_2}}{i(\omega - \omega_{02}) + \frac{1}{\tau_2} + \frac{1}{\tau_{abs2}}}$$

$$r_{PhC} = r_{slab} - \frac{(r_{slab} + t_{slab})\frac{1}{\tau_1}}{i(\omega - \omega_{01}) + \frac{1}{\tau_1} + \frac{1}{\tau_{abs1}}} - \frac{(r_{slab} - t_{slab})\frac{1}{\tau_2}}{i(\omega - \omega_{02}) + \frac{1}{\tau_2} + \frac{1}{\tau_{abs2}}}$$

and vice versa for the opposite case.

Substituting Equations (5.1) and (5.2) into $|a_{PhC}|^2 = 1 - |r_{PhC}|^2 - |t_{PhC}|^2$ gives, after some algebra,

$$|a_{PhC}|^2 = \frac{2|\kappa^2|^2 \frac{1}{\tau_{rad}} \frac{1}{\tau_{abs}}}{(\omega - \omega_0)^2 + (\frac{1}{\tau_{rad}} + \frac{1}{\tau_{abs}})^2}$$

By applying time-reversibility to a lossless cavity[28], one can show that $|\kappa^2| = 1$. We now proceed to do this. Consider a situation with no source, such that $s_{+1} = s_{+2} = 0$. The cavity mode amplitude decays at $1/\tau_{rad}$ through symmetric decay channels $s_{-1} = s_{-2} = s_-$.

$$\frac{d|a|^2}{dt} = -\frac{2}{\tau_{rad}}|a|^2 = -2|s_-|^2$$

Note that $|a|^2 = \tau_{rad}|s_-|^2$. Now consider the time-reversed situation, where the lossless cavity, with amplitude $\tilde{a}$, grows at the rate $1/\tau_{rad}$ as a result of being driven by incident waves.

$$\frac{d|\tilde{a}|^2}{dt} = \frac{2}{\tau_{rad}}|\tilde{a}|^2$$

(Quantities with a tilde indicate the time-reversed situation.) For our situation with two inputs, it is true that

$$\tilde{a} = \frac{\sqrt{\frac{1}{\tau_{rad}}}\kappa(2\tilde{s}_+)}{i(\omega - \omega_0) + \frac{1}{\tau_{rad}}}$$

Since $|\tilde{a}|$ grows at $1/\tau_{rad}$, we can write $\omega = \omega_0 - i/\tau_{rad}$. Substituting this into the expression for $\tilde{a}$ gives $|\tilde{a}|^2 = \tau_{rad}|\kappa|^2|\tilde{s}_+|^2$. At time zero, $|a| = |\tilde{a}|$ and $|s_-|^2 = |\tilde{s}_+|^2$, allowing us to conclude that $|\kappa|^2 = 1$. Thus, the absorption coefficient of the photonic

crystal slab is given by

$$|a_{PhC}|^2 = \frac{2\frac{1}{\tau_{rad}}\frac{1}{\tau_{abs}}}{(\omega-\omega_0)^2 + (\frac{1}{\tau_{rad}}+\frac{1}{\tau_{abs}})^2} \tag{5.5}$$

Clearly, absorptivity (and therefore, emissivity) is maximized when $\tau_{rad} = \tau_{abs}$. In terms of quality factors ($Q_{rad} \equiv \omega_0\tau_{rad}/2$), this means $Q_{rad} = Q_{abs}$, i.e. the absorption is maximized when the Q_{rad} of the Fano resonance is exactly matched with the absorptive Q_{abs} of the guided mode. When $Q_{rad} = Q_{abs}$, $|a_{PhC}|^2_{max} = 50\%$. For certain different geometries (e.g. dielectric 2D PhC placed on top of a uniform metallic surface), $|a_{PhC}|^2_{max}$ can equal 100%.

The frequency (ω_0) and the lifetime ($\tau_{rad} = 1/\gamma = 1/HWHM$) of the lossless Fano resonances can be extracted from FDTD simulations. The cavity lifetime τ_{abs} (due to material absorption losses only) can be calculated as follows. The quality factor of a cavity with only internal losses (i.e. decoupled from the outside world) is defined by

$$Q_{abs} = \frac{\omega_0}{2(1/\tau_{abs})}.$$

An equivalent definition is

$$Q_{abs} = \frac{\omega_0\langle U\rangle}{\langle P\rangle}$$

where $\langle U\rangle$ is the average energy stored in the cavity, and $\langle P\rangle$ is the average rate of energy dissipation. Combining the two yields an expression for τ_{abs}:

$$\tau_{abs} = \frac{2\langle U\rangle}{\langle P\rangle} = 2\frac{\frac{1}{2}\int \epsilon_r\epsilon_0|\mathbf{E}|^2dV}{\frac{1}{2}\int \sigma|\mathbf{E}|^2dV}$$

where $\epsilon_r\epsilon_0$ is the real part of the dielectric function of the material (ϵ_r is the relative permittivity), and σ is the electric conductivity. (The lower integral comes from $\langle P\rangle = \frac{1}{2}\int \mathbf{J}\cdot\mathbf{E}dV$ and $\mathbf{J} = \sigma\mathbf{E}$.) The region of integration is only close to the slab. Assuming homogeneous media (ϵ_r and σ independent of position), we can write

$$\tau_{abs} = \frac{2\epsilon_r\epsilon_0}{\sigma\xi} \tag{5.6}$$

where ξ is the fraction of modal energy contained within the dielectric.

It is well known that the imaginary part of the relative permittivity is given by $\epsilon_i = \sigma/\omega\epsilon_0$ (where $\omega = \omega_0$ in our case). Thus, we obtain a simple expression for the absorptive Q_{abs}:

$$Q_{abs} = \frac{\epsilon_r}{\xi\epsilon_i}$$

We derived this under the high-Q approximation, assuming that the fields are only slightly perturbed by the introduction of absorption in the material, which is indeed the case here close to the resonance. (A similar result can be derived via perturbation theory in ϵ_i[73].)Note that Eqs. (5.5) and (5.6) provide us with a physical model that can be used as a powerful tool for thermal design and understanding anomalous thermal behavior.

5.4 Numerics

As we have seen, our analytical model consists of equations for the transmission, reflection and absorption coefficients of Fano resonances, together with an expression for τ_{abs}, the cavity lifetime in terms of ϵ_r and ϵ_i. Let us now proceed to test this model against numerical simulations, in order to validate our theory.

Numerical simulations in our work are performed using a finite-difference time-domain (FDTD) algorithm[75]. These are exact 3D solutions of Maxwell's equations, including material dispersion and absorption. We choose a computational cell with dimensions $30 \times 30 \times 300$ grid points, corresponding to 30 grid points per lattice constant a. The photonic crystal slab is in the middle, and flux planes are placed on either side of it at least $2a$ away. The slab is $0.5a$ thick. We run the simulation for a total of 988,235 time steps, chosen to be sufficiently large to allow resolution of peaks with quality factors (Q) in excess of 2,500. We illuminate the photonic crystal slab with a temporally Gaussian pulse, with a transverse wave vector of our choosing (this is implemented by specifying a phase difference between fields on opposite faces of the computational cell). We record the fields going through flux planes on either side of the slab and perform a discrete Fourier-transform on the time-series of fields, which

we use to calculate fluxes as functions of frequency ($\Phi(\omega)$). We run the simulation once with the slab in place, and again with vacuum only. The reflectance is given by $R(\omega) = (\Phi_1^{vac}(\omega) - \Phi_1^{slab}(\omega))/\Phi_1^{vac}(\omega)$ where the flux plane closer to the light source is '1', and the flux plane further from the light source is '2'. The transmission is given by $T(\omega) = \Phi_2^{slab}(\omega)/\Phi_2^{vac}(\omega)$ and the absorption is simply $A(\omega) = 1 - R(\omega) - T(\omega)$. This way, we obtain reflectance, transmission and absorption spectra for PhC slabs. We repeat these calculations for incident light with different transverse wave vectors (k_x). From these spectra, the resonant frequencies and widths (i.e. lifetimes) of Fano resonances can be extracted. We incorporate absorption into our simulations by means of the Drude model, according to the following equation: $\epsilon(\omega) = \epsilon_\infty + \sigma/(\omega_0^2 - \omega^2 - i\gamma\omega)$ where ϵ_∞, γ, ω_0 and σ are input parameters. These are chosen so as to produce the desired absorption ($\mathrm{Im}(\epsilon)$) at the frequencies we are interested in.

We show the results in Fig. 5-3. First, we plot transmission, reflectance and absorption in the nearly lossless case ($\gamma_{abs} < 3 \times 10^{-6}$) for the first two Fano peaks shown in Fig. 5-2b (red circles in Fig. 5-3); then ω_0 and γ ($= 1/\tau_{rad}$) were extracted from these numerical results, and analytical predictions (red lines) were thus obtained. (The parameters r_{slab} and t_{slab} representing the background of the spectra are the standard expressions for the reflection and transmission coefficients of a uniform slab: we refer the reader to Equations (9) and (10) in [19].) We then plot the numerical results with absorption (black circles), and the predictions of the model (black lines). This was done for both peaks.

We see very good agreement between theory and simulation. The imaginary part (ϵ_i) of the material in the absorptive case was chosen such that there is near-perfect matching between the Q_{rad} of the first resonance (≈ 370) and the absorptive Q of the material: $Q_{abs} = Q_{rad}$, which causes the absorption to be maximized. We see this clearly in the first panel, where the absorption coefficient (black line and circles) hits 50%. The same is not true of the second peak, because the Q_{rad} of that peak (≈ 2000) is much higher than $Q_{abs} = 370$, so there is poor Q-matching and thus weaker absorption. Nonetheless, the fit between theory and simulation is excellent.

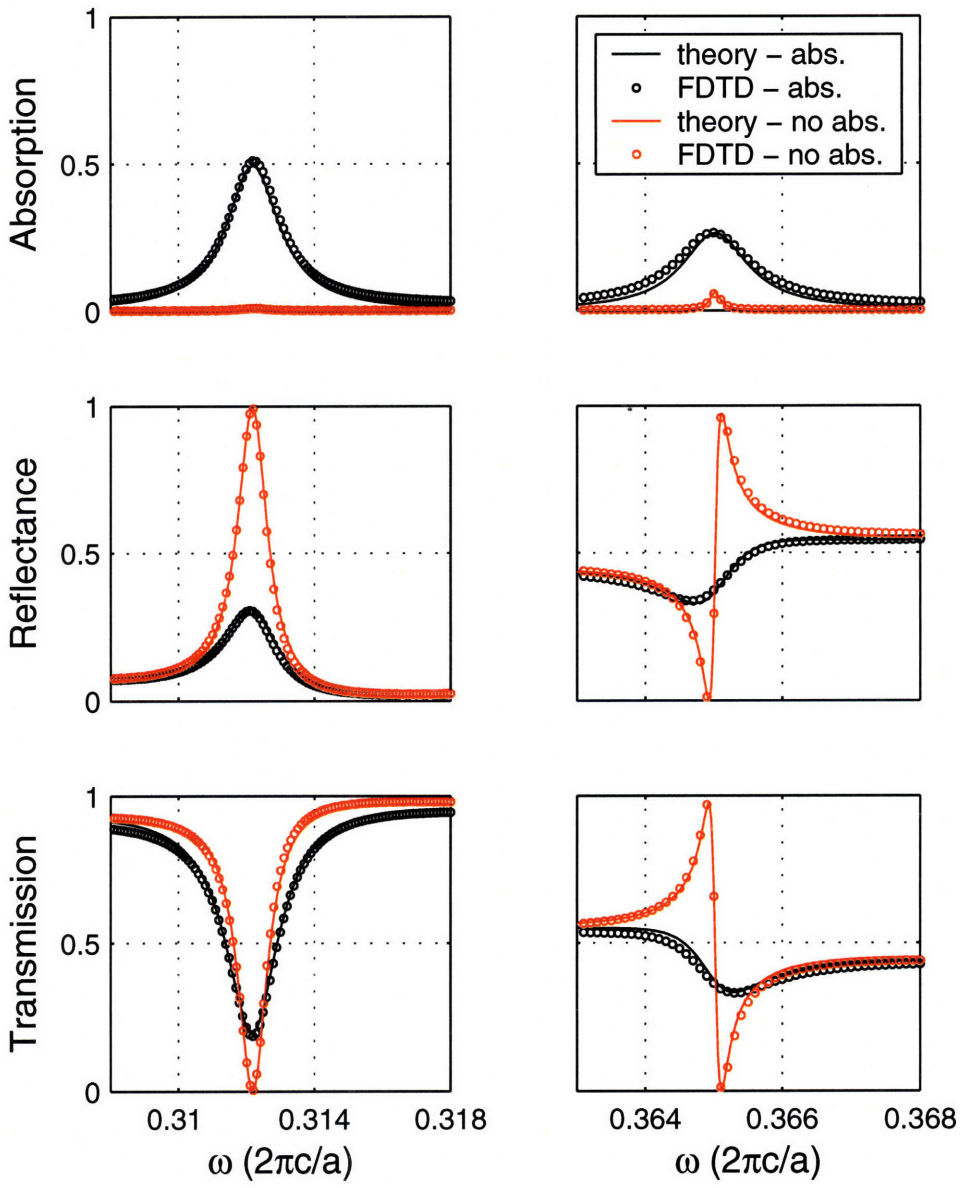

Figure 5-3: (Color) Comparison between theory and simulation, for the first two Fano peaks shown in Fig. 5-2a. The parameters of the theory (ω_0 and γ) were calibrated by fitting the red line (theory without absorption) to the red circles (simulation without absorption). The black line gives the prediction of theory for the absorptive case; the black circles represent the results from simulation with absorption. (The fraction of energy in dielectric (ξ) was 90% for the first peak and 95% for the second, done in a separate FDTD calculation.)

5.5 Thermal design

Confident that our analytical model has been validated by numerical studies, we proceed to apply this model to the case of thermal design. Kirchhoff's law allows us to relate absorptivity and emissivity, such that if we can design a PhC with high absorptivity for certain frequencies, we know that it will also have high emissivity for those frequencies too. We have shown that low emissivities of uniform slabs can be greatly enhanced by means of Fano resonances. The frequencies of these emission peaks are determined by the frequencies of Fano resonances, while the heights of these peaks are determined by how well Q_{abs} matches with Q_{rad}. The exact positions of Fano frequencies can be controlled by the geometry of the PhC (slab thickness, lattice constant a, ϵ_r, and to some extent also hole sizes) which determines the guided modes. Q_{rad} is determined by the strength of the coupling of the guided modes to radiation (controlled mostly by the size of the holes). Q_{abs} is determined by ϵ_i, and the overlap of the guided modes with the regions of the structure that are absorptive. Given that one has so many parameters to control, and that their influence is largely decoupled, one is provided with excellent possibilities to tailor properties of thermal radiation almost at will.

In fact, most of the relevant parameters can even be controlled dynamically. For example, changes in geometry can be implemented mechanically at ms-μs time scales (e.g. MEMS). Similarly, changes of ϵ_r, ϵ_i can be implemented via change of temperature, or using electro-optical effects, or carrier injection (this can change ϵ_i by orders of magnitude); some of these effects can be operated at sub-nanosecond time scales.

As an illustrative example, we study the case where ϵ_i varies with temperature. In the case of silicon, the imaginary part of the dielectric function is strongly temperature-dependent, and increasing the temperature from, say, 750K to 1000K increases the imaginary part in the IR regime from 10^{-3} to 10^{-2}, i.e. by a factor of ten[13]. (The real part changes by 3% or so. We use the following expressions for the temperature-dependent refractive index for silicon: $n_{Si} = 16.044(1000\lambda)^{-0.194}$ and $k_{Si} = (\alpha/4\pi)\lambda \times 10^{-4}$, where $\alpha = 4.15 \times 10^{-5}\lambda^{1.51}T^{2.95}e^{-7000/T}$, with λ specified in μm

and α in cm^{-1}.) At 750K, $Q_{abs} \sim 1000$ and the higher frequency Fano peak (at around 4.5μm in Fig. 5-1b) is more closely matched with Q_{abs} than the lower frequency peak, resulting in a higher emissivity. At 1000K, $Q_{abs} \sim 100$ and the lower frequency Fano peak (at around $3.8\mu m$) is better matched, resulting in emissivity close to 50%. In other words, as we heat up this 2D silicon PhC slab, we see peak emission move from short to long wavelength. This is precisely the opposite of what is expected from a simple graybody, where the wavelength of strongest emission decreases with temperature. Without additional information, an external observer would be led to think that the body's temperature is actually decreasing. Note that the position of each emissivity peak is fairly independent of the temperature, which is also markedly different than in ordinary graybodies. This anomalous emissivity behavior occurs as a result of a peculiar interplay between $Q_{abs}(T)$ and the Q_{rad} of the Fano resonances.

Of further interest is the fact that Fano resonance frequencies can change with wave vector (c.f. Fig. 5-2b). Since wave vector and angle of incidence are related, it is clear that peak frequencies vary with the angle at which we view the material. Fig. 5-4 shows the variation in the frequency of the emissivity peak with respect to change in angle. In the top panel, plotted for the low-frequency Fano resonance from Fig. 5-2a, we see that as we move away from normal incidence, the frequency of the peak decreases. This agrees well with the band diagram for Fano resonances in Fig. 5-2b, which shows decreasing ω with increasing k_x (a proxy for angle of incidence) for the first band. In the bottom panel, we plot the same variation for the second peak. This agrees with the band diagram again in Fig. 5-2b, which shows a relatively flat second band. Such a material would be intriguing in that it would emit different thermal colors depending on the direction from which it is viewed; observers without additional information would perceive the 'temperature' changing with the angle of observation.

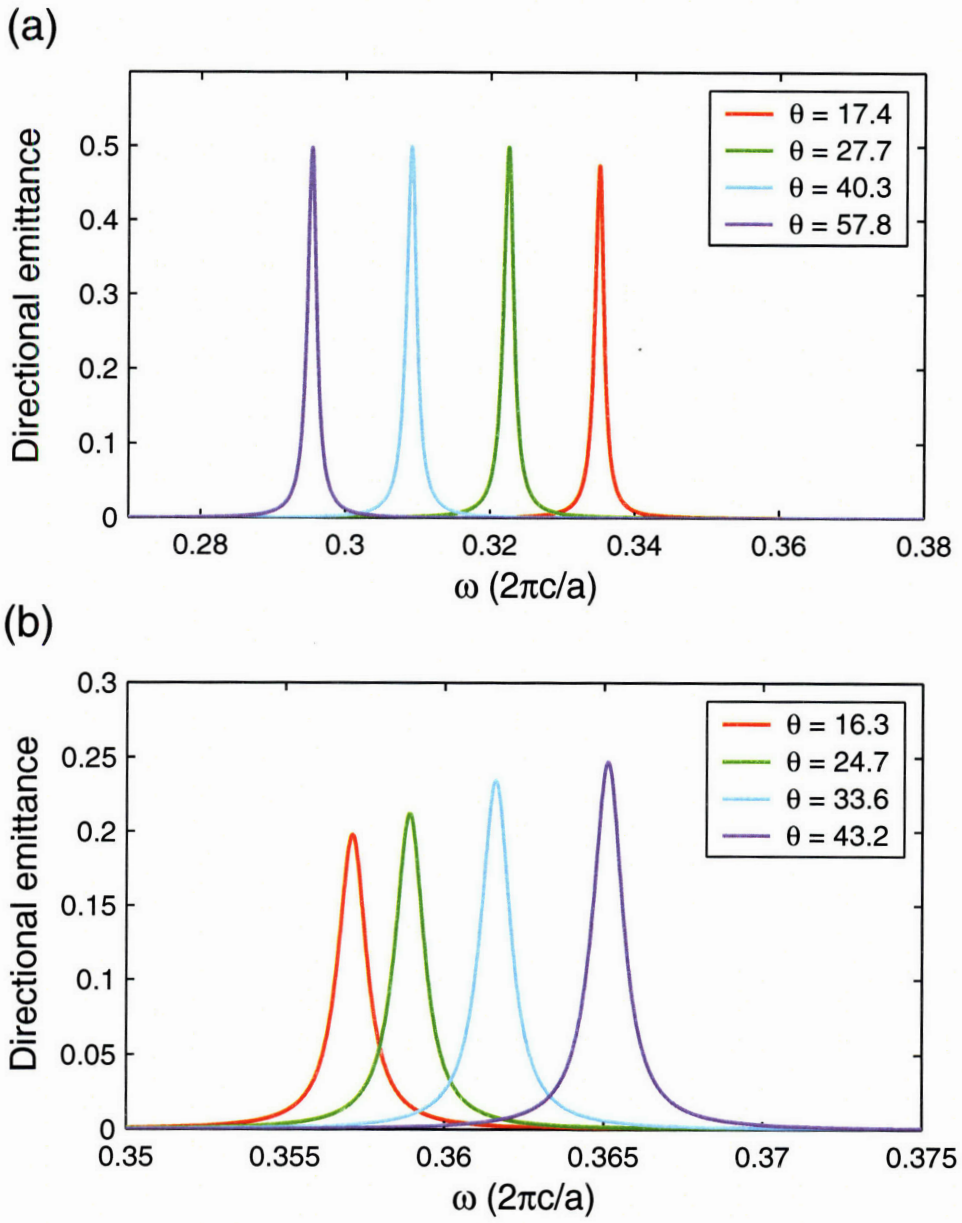

Figure 5-4: (Color) Variation of Fano absorption peak frequency as function of angle of incidence (in degrees); rotation angle is around y-axis, and electric field is polarized along y-direction. (a) First peak. (b) Second peak. The change in frequency for the second peak is much smaller than that for the first. The angles are different for the top and bottom panels even though the k_x's used are the same because θ is a function of both k_x and ω.

5.6 Conclusion

We have demonstrated that the significant enhancement of thermal emission via Q-matching, which has been possible in 1D systems only, can be extended to 2D systems by means of Fano resonances in the 2D system. Through detailed numerical and analytical studies, we showed that these Fano resonances characteristic of 2D-periodic photonic crystal slabs can be understood in terms of a 1D-model. Moreover, we found that properties of these spectra can be controlled by changing the geometrical parameters of the photonic crystals. Therefore, this work provides a path to the creation of graybodies that have tailored thermal emission spectra, with highly unusual properties.

Since thermal emission is so ubiquitous, we expect this novel capability of tailoring it to open up a wide range of new and exciting opportunities. The capability to significantly change the thermal spectra of bodies dynamically (and perhaps even at time scales shorter than the thermalization times), could enable implementation of another intriguing class of systems. In terms of concrete applications, coherent thermal emission in infra-red spectra could be used for remote sensing. As far as defense applications go, many reconnaissance (e.g. night-vision), as well as targeting systems are based on thermal emission; the capability to modify thermal emission might thus provide means of protection for objects that are being targeted.

Chapter 6

Direct calculation of thermal emission for 2D- and 3D-periodic photonic crystal slabs

We perform direct thermal emission calculations for 2D- and 3D-periodic photonic crystal slabs using stochastic electrodynamics following the Langevin approach, implemented via an FDTD algorithm. We demonstrate that emissivity and absorptivity are equal, by showing that such photonic crystal systems emit as much radiation as they absorb, for every frequency, up to statistical fluctuations. We also study the effect of surface termination on absorption and emission spectra from these systems.

6.1 Introduction

The physics of blackbodies has fascinated and intrigued researchers for well over a century now[59]; properties of their thermal emission provided one of the most important clues for the discovery of quantum mechanics. In practice, most objects have absorption less than that of a blackbody, and are thus referred to as 'graybodies'. By virtue of Kirchhoff's law, these objects also have sub-unity emissivity. However, the thermal emission spectra of graybodies can be changed by altering the geometry of the system or the materials used.

Very exciting work has been done recently on three-dimensionally periodic photonic crystals with photonic band gaps[44, 41, 22, 45, 42, 43, 46, 12, 23] concerning enhancement and suppression of thermal emission[41, 42, 43] and thermophotovoltaic applications[45, 46]. Emission and absorption from 2D-periodic photonic crystals have been also studied within the contexts of spectral and directional control[51, 69, 61, 16, 38], guided resonances[19], thermophotovoltaic generation[68], resonant scattering[58, 15], laser action[50], Kirchhoff's law[26, 48], coherence[25, 38], and spontaneous emission enhancement[7, 17, 61]. It has been noted that periodic subwavelength scale patterning of metallodielectric systems, i.e. photonic crystals, can modify their thermal emission spectra in many interesting ways[70, 53, 17, 69, 25, 68, 54, 48, 16, 23], through various physical effects such as surface plasmons[61, 39], resonant-cavity enhancement[11], Bragg reflection[14] and modification of density of states via photonic band gaps[14, 41, 45, 46].

In previous work, most calculations for thermal emission were performed by calculating the absorption and then appealing to Kirchhoff's law, which states that absorptivity and emissivity are equal. This has been shown analytically for a uniform slab. Luo *et al.*[48], following a Langevin approach to stochastic electrodynamics, performed a direct thermal emission calculation for a 2D-periodic photonic crystal slab and showed that emissivity was equal to absorptivity (up to thermal fluctuations), thus numerically verifying Kirchhoff's law for such systems. This has been an issue of great controversy because of experimental work indicating the violation of Kirchhoff's law[45, 43].

In this chapter, we extend the work done by Luo *et al.* to 3D-periodic structures. Using stochastic electrodynamics, we perform direct simulations of emission spectra for 2D- and 3D-periodic structures. We compare these directly calculated emission spectra to the absorption spectra of these systems, and demonstrate that Kirchhoff's law holds for 3D-periodic photonic crystal slabs. Moreover, we examine the effect of changing the surface termination of a 3D-periodic structure and suggest how it may be used to enhance absorption and emission of a photonic crystal. We also give an in-depth and coherent presentation of the theory of stochastic electrodynamics,

including relevant derivations and detailed explanations of our methodology.

This paper is organized as follows: in section 6.2, we describe the theory of stochastic electrodynamics, and how it can be used to perform direct emission calculations. Section 6.3 outlines the numerical methods and techniques used in this paper. In section 6.4, we study a 2D-periodic array of rods, and show bandstructure, absorption and emission calculations. We do the same in sections 6.5 and 6.6 for a 3D-periodic woodpile structure and metallodielectric structure, respectively. Section 6.7 deals with the effect of surface termination, and how it can be used to enhance emission in these photonic crystal slab structures.

6.2 Theory

6.2.1 Stochastic electrodynamics and the Langevin approach

Maxwell's equations, as they stand, are classical deterministic field equations. We would like to introduce an element of randomness into these field equations, in order to represent the randomness inherent in thermal fluctuations. We follow the Langevin approach to Brownian motion by introducing a random force term into our equations. There are three ways in which we can proceed: (i) introduce randomness directly in the Newtonian equation of motion, (ii) add a random term to the displacement field, $\mathbf{D}$, or (iii) add a random term to the free current density, $\mathbf{J}$. These three ways of introducing randomness are entirely equivalent, as we will demonstrate.

The first approach introduces randomness through the addition of a random term in Newton's equation of motion. Modeling charge carriers as damped simple harmonic oscillators driven by an external field $\mathbf{E}$, we can write, for a deterministic system, $\ddot{\mathbf{r}} + \gamma\dot{\mathbf{r}} + \omega_0^2\mathbf{r} = e\mathbf{E}/m$, where $\mathbf{r}$ is the position of the charge carrier, e its charge, m its mass, γ the damping constant of the system, and ω_0 the natural resonant frequency of the system. Converting this to polarization via $\mathbf{P} = ne\mathbf{r}$ (where n is the density of

positive charge), we have

$$\frac{d^2\mathbf{P}}{dt^2} + \gamma\frac{d\mathbf{P}}{dt} + \omega_0^2\mathbf{P} = \sigma\mathbf{E} \tag{6.1}$$

where $\sigma \equiv ne^2/m$. We introduce a random term ($\mathbf{K}$) to the right-hand side following the Langevin approach:

$$\frac{d^2\mathbf{P}}{dt^2} + \gamma\frac{d\mathbf{P}}{dt} + \omega_0^2\mathbf{P} = \sigma\mathbf{E} + \mathbf{K}(t) \tag{6.2}$$

Substituting in a harmonic ansatz for $\mathbf{P}$ gives the following solution:

$$\mathbf{P}(\mathbf{r},\omega) = \frac{\sigma\mathbf{E}(\mathbf{r},\omega)}{\omega_0^2 - \omega^2 - i\gamma\omega} + \frac{\mathbf{K}(\mathbf{r},\omega)}{\omega_0^2 - \omega^2 - i\gamma\omega}$$

Polarization is related to the displacement field via $\mathbf{D} = \mathbf{E} + 4\pi\mathbf{P}$. Thus, we see that $\mathbf{D}$ consists of an external field $\mathbf{E}$, the usual non-stochastic polarization-induced component $4\pi\sigma\mathbf{E}(\mathbf{r},\omega)/(\omega_0^2 - \omega^2 - i\gamma\omega)$, and a random component which we define as

$$\mathbf{Q}(\mathbf{r},\omega) \equiv \frac{4\pi\mathbf{K}(\mathbf{r},\omega)}{\omega_0^2 - \omega^2 - i\gamma\omega} \tag{6.3}$$

Thus, a fluctuating polarization ($\mathbf{K}$) in the Newtonian equation of motion is equivalent to a random, fluctuating term ($\mathbf{Q}$) in the displacement field. The fourth Maxwell equation now becomes

$$\nabla \times \mathbf{H} = \frac{4\pi}{c}\mathbf{J} + \frac{1}{c}\frac{\partial}{\partial t}(\mathbf{D} + \mathbf{Q})$$

Alternatively, instead of introducing randomness to the displacement field, we could just as easily have added a random term $\mathbf{J}_{\text{fluc}} = \frac{1}{4\pi}\frac{\partial\mathbf{Q}}{\partial t}$ to the free current density $\mathbf{J}$, and the end result would have been the same. Therefore, we have shown that approaches (i), (ii) and (iii) for introducing randomness into Maxwell's equations are entirely equivalent.

6.2.2 Statistical properties of thermal fluctuations

Let us proceed with the fluctuating displacement field. The correlation function for $\mathbf{Q}$ has to satisfy a fluctuation-dissipation relation, derived by Rytov[66]:

$$\langle Q_i(\mathbf{r},\omega)Q_j^*(\mathbf{r}',\omega')\rangle = \frac{16\pi^3 c^2 \mathrm{Im}[\epsilon(\omega)]}{\omega^3} I_0(\omega,T)\delta_{ij}\delta_{\omega\omega'}\delta(\mathbf{r}-\mathbf{r}') \tag{6.4}$$

where Q_i for $i = 1,2,3$ are the components of $\mathbf{Q}$, $\langle\cdots\rangle$ denotes ensemble averaging, c is the speed of light, $\mathrm{Im}[\epsilon(\omega)]$ is the imaginary part of the permittivity including the polarization response in the absence of fluctuations (cf. Eq. (6.1)), and $I_0(\omega,T) = \frac{c}{4\pi}D(\omega)E(\omega,T)$. In this expression, $D(\omega) = \frac{\omega^2}{\pi^2 c^3}$ is the free-space density of photon states and $E(\omega,T) = \hbar\omega/[\exp(\hbar\omega/kT) - 1]$ is the Bose-Einstein energy distribution function at absolute temperature T.

We can also calculate the correlation function for $\mathbf{Q}$ directly from Eq. (6.3):

$$\langle Q_i(\mathbf{r},\omega)Q_j^*(\mathbf{r}',\omega')\rangle = \frac{(4\pi)^2}{[(\omega_0^2-\omega^2)-i\gamma\omega][(\omega_0^2-\omega'^2)-i\gamma\omega']}\langle K_i(\mathbf{r},\omega)K_j^*(\mathbf{r}',\omega')\rangle \tag{6.5}$$

The two expressions for the $\mathbf{Q}$ correlation function must be equal. By equating Eqs. (6.4) and (6.5), we can learn something about the correlation function of $\mathbf{K}$.

Our first step is to find the imaginary part of the dielectric function. In the absence of fluctuations, the dielectric function for our system is

$$\epsilon(\omega) = 1 + 4\pi\frac{|\mathbf{P}|}{|\mathbf{E}|} = 1 + \frac{4\pi\sigma}{\omega_0^2 - \omega^2 - i\gamma\omega}$$

Therefore, the imaginary part is

$$\mathrm{Im}[\epsilon(\omega)] = \frac{4\pi\sigma\gamma\omega}{(\omega_0^2-\omega^2)^2 + \gamma^2\omega^2} \tag{6.6}$$

Combining Eqs. (6.4), (6.5) and (6.6) gives

$$\langle K_i(\mathbf{r},\omega)K_j^*(\mathbf{r}',\omega')\rangle = \frac{4\pi^2 c^2\sigma\gamma}{\omega^2} I_0(\omega,T)\delta_{ij}\delta_{\omega\omega'}\delta(\mathbf{r}-\mathbf{r}') \tag{6.7}$$

This expression for the $\mathbf{K}$ correlation function gives us information about the distribution of the Langevin noise term. However, since finite difference numerical simulations require the discretization of space, for our calculations, it will be necessary to convert the Dirac delta function in $\mathbf{r}$ to a Kronecker delta.

The delta function $\delta(\mathbf{r}-\mathbf{r}')$ can be defined as follows:

$$f(\mathbf{r}) = \int_V f(\mathbf{r}')\delta(\mathbf{r}-\mathbf{r}')d^3\mathbf{r}'$$

for any function $f(\mathbf{r})$ over some volume V. We can discretize the above definition by approximating the integral by a discrete summation:

$$f(\mathbf{r}) = \sum_V f(\mathbf{r}')\frac{\delta_{\mathbf{r}\mathbf{r}'}}{\Delta V}\Delta V$$

where ΔV is the volume element used in the simulation. Therefore, we can go from the continuous to the discrete limit by making the replacement $\delta(\mathbf{r}-\mathbf{r}') \rightarrow \delta_{\mathbf{r}\mathbf{r}'}/\Delta V$. Making this substitution in Eq. (6.7) gives us the discretized version (where we have set $\mathbf{r}' = \mathbf{r}$):

$$\langle K_i(\mathbf{r},\omega)K_j^*(\mathbf{r},\omega')\rangle = \frac{4\pi^2\sigma\gamma\delta_{ij}\delta_{\omega\omega'}}{\Delta V}\frac{I_0(\omega,T)}{(\omega/c)^2} \tag{6.8}$$

Note that in the high temperature limit, where $\hbar\omega \ll kT$, the Bose-Einstein energy density function $\hbar\omega/[\exp(\hbar\omega/kT)-1] \approx kT$, and so $I_0(\omega,T) \sim \omega^2$. This exactly cancels out the frequency dependence on the right-hand side of Eq. (6.8), leading to a white-noise spectrum in $\mathbf{K}$. However, we will find in the next section that emissivity can be simulated by a white-noise spectrum for *all* frequencies.

6.2.3 Calculation of emissivity

To calculate emissivity, the target thermal emission intensity needs to be normalized by that of the free-space Planck radiation. The linearity of the system ensures that this normalization procedure amounts to dividing the right-hand side of Eq. (6.8) by the blackbody radiation collected within an element of solid angle. It can be shown that[64] the Planck radiation emitted into an element of solid angle $d\Omega$ is

$I_0(\omega, T)\cos\theta d\Omega$.

However, in finite-difference time-domain calculations of photonic crystal systems implementing Bloch-periodic boundary conditions in the xz and yz faces, directions are specified using wave vectors k_x and k_y instead of polar and azimuthal angles θ and ϕ. Thus, the calculable quantity is $\langle K_i(\mathbf{r},\omega)K_j'^*(\mathbf{r},\omega')\rangle dk_x dk_y$ for emission into wave vector range $(k_x, k_x + dk_x)$ and $(k_y, k_y + dk_y)$. It is straightforward to calculate the Jacobian to convert from angles to wave vector components: $dk_x dk_y = (\omega/c)^2 \sin\theta\cos\theta d\theta d\phi = (\omega/c)^2\cos\theta d\Omega$. The Planck intensity of emission into $d\Omega$ is therefore

$$I_0(\omega, T)\cos\theta d\Omega = I_0(\omega, T)\frac{dk_x dk_y}{(\omega/c)^2} \tag{6.9}$$

Thus, the normalization factor is $I_0(\omega, T)/(\omega/c)^2$. Dividing Eq. (6.8) by this factor gives the emissivity spectrum for a given (k_x, k_y):

$$\langle K_i'(\mathbf{r},\omega)K_j'^*(\mathbf{r},\omega')\rangle = \frac{4\pi^2 C'^2\sigma\gamma\delta_{ij}\delta_{\omega\omega'}}{\Delta V} \tag{6.10}$$

where $\mathbf{K}'(\mathbf{r},\omega) \equiv C'\mathbf{K}(\mathbf{r},\omega)\sqrt{(\omega/c)^2/I_0(\omega,T)}$, and we are considering emission into an element of wave vector specified by $dk_x dk_y$. C' is a dimension-correcting factor that depends only on the discretization details of the system. It converts a fluctuation in polarization to a fluctuation in emissivity. Fourier-transforming back to the time-domain gives

$$\langle K_i'(\mathbf{r},t)K_j'^*(\mathbf{r},t')\rangle = \frac{1}{N^2}\sum_{\omega\omega'}\langle K_i'(\mathbf{r},\omega)K_j'^*(\mathbf{r},\omega')e^{-i\omega t+i\omega' t'}\rangle = \frac{4\pi^2 C'^2}{N\Delta V}\sigma\gamma\delta_{ij}\delta_{tt'} \tag{6.11}$$

with N being the number of time steps used in the Fourier transform. Thus, we can simulate emissivity by producing a time series of random drawings from a distribution with variance $\langle|K_i'(\mathbf{r},t)|^2\rangle$. Since this is the only physical constraint on the distribution of $\mathbf{K}$, we are free to choose a simple and tractable distribution for our simulations.

We choose a uniform distribution:

$$w[K_i'] = \begin{cases} 1/K_s & \text{if } |K_i'| < K_s/2 \\ 0 & \text{if } |K_i'| > K_s/2 \end{cases} \tag{6.12}$$

such that $K_s^2 = C\sigma\gamma$, with $C = 48\pi^2 C'^2/(N\Delta V)$ being a discretization-specific constant. Since Kirchhoff's law has been proven analytically for a 1D uniform slab, we perform calibration runs on a uniform slab for both emission and absorption in order to obtain the calibration constant. We then use the same constant (which is discretization-specific) to convert emitted 'flux' to emissivity for the case of the photonic crystal slab. Thus, we can calculate emissivity for a photonic crystal at *all* temperatures.

6.2.4 Limitations of the method

The approach we have outlined so far is able, as far as thermal fluctuations are concerned, to reproduce the wave nature of light, but not its particle nature.

From statistical mechanics[64], we know that the expected number of photons occupying a particular mode j is given by the Bose-Einstein distribution:

$$\langle n_j \rangle = \frac{1}{e^{\beta\epsilon_j} - 1}$$

where $\langle n_j \rangle$ is the mean occupation number of state j, $\beta = 1/kT$ where T is the temperature and k is Boltzmann's constant, and ϵ_j is the energy associated with the j^{th} state.

The mean square deviation of the photon occupation number from this mean is given by[64]

$$\langle \Delta n_j^2 \rangle = \frac{1}{\beta}\frac{\partial \langle n_j \rangle}{\partial \epsilon_j} = \langle n_j \rangle + \langle n_j \rangle^2 \tag{6.13}$$

Thus, we see that

$$\frac{\langle \Delta n_j^2 \rangle}{\langle n_j \rangle^2} = 1 + \frac{1}{\langle n_j \rangle} \tag{6.14}$$

For a general particle in the Maxwell-Boltzmann limit, $-\mu/kT \gg 1$ and so the Bose-

Einstein distribution can be approximated by $e^{\beta(\mu-\epsilon_j)}$. Plugging this into Eq. (6.13) gives

$$\frac{\langle \Delta n_j^2 \rangle}{\langle n_j^2 \rangle^2} = \frac{1}{\langle n_j \rangle}$$

Therefore, we can think of the $1/\langle n_j \rangle$ term as arising from the particle nature of light (because in the Maxwell-Boltzmann limit, these photons do behave more like particles than waves). Consequently, by deduction, the 1 term in Eq. (6.14) accounts for the wave nature of light. This term dominates in the limit of $kT \gg \epsilon_j$.

Luo *et al.*[48] performed a statistical analysis on their ensemble data and found that $\sqrt{\langle \Delta I(\omega,T)^2 \rangle} = \langle I(\omega,T) \rangle$. Thus, the stochastic electrodynamics that we have described so far reproduce the wave nature of light correctly. We can convert the fluctuations we see in our simulations to the real *physical* fluctuations by observing that $\frac{\langle \Delta n_j^2 \rangle}{\langle n_j \rangle^2} = \exp(\hbar\omega/kT)$ for physical fluctuations, and then scaling the observed fluctuations by the factor $\exp(\hbar\omega/2kT)$. Therefore, $\sqrt{\langle \Delta I(\omega,T)^2 \rangle} = \exp(\hbar\omega/2kT)\langle I(\omega,T) \rangle$.

6.3 Description of numerical methods

Numerical simulations in our work are performed using a finite-difference time-domain (FDTD) algorithm[75]. These are exact (apart from discretization) 3D solutions of Maxwell's equations, including material dispersion and absorption. Eqs. (6.1) and (6.2) can be discretized in the standard way by writing $d^2\mathbf{P}(\mathbf{r},t)/dt^2 \approx [\mathbf{P}(\mathbf{r},t+\delta t) - 2\mathbf{P}(\mathbf{r},t) + \mathbf{P}(\mathbf{r},t-\delta t)]/\delta t^2$ and $d\mathbf{P}(\mathbf{r},t)/dt \approx [\mathbf{P}(\mathbf{r},t+\delta t) - \mathbf{P}(\mathbf{r},t-\delta t)]/(2\delta t)$.

For 2D calculations, we choose a computational cell with dimensions $40 \times 2 \times 640$ grid points, corresponding to 40 grid points per lattice constant a. The faces of the cell normal to the x and y axes are chosen to have periodic boundary conditions, while the faces normal to the z-axis (i.e. the top and bottom ones) have perfectly matched layers (PML) to prevent reflection. This is a 2D simulation of a 2D-periodic system. The slab is placed in the middle of the cell, and flux planes are placed on either side of it at least $4a$ away. We run the simulation for a total of 81,600 time steps, chosen to give a frequency resolution of $0.001c/a$.

For 3D calculations, we choose a computational cell with dimensions $30 \times 30 \times 420$

grid points, corresponding to 30 grid points per lattice constant a. The faces of the cell normal to the x and y axes are chosen to have periodic boundary conditions, while the faces normal to the z-axis (i.e. the top and bottom ones) have PML boundary conditions. The slab is placed one-third of the way down the cell, and flux planes are placed on either side of it at least $3a$ away. We run the simulation for a total of 60,000 time steps, also chosen to be sufficiently large to give a frequency resolution of $0.001c/a$.

For absorbance calculations, we illuminate the photonic crystal (PhC) slab with a normally incident, temporally Gaussian pulse. We record the fields going through flux planes on either side of the slab and perform a discrete Fourier transform on the time-series of fields, which we use to calculate fluxes as functions of frequency ($\Phi(\omega)$). We run the simulation once with the slab in place, and again with vacuum only. We record the fields going through flux planes on either side of the slab and perform a discrete Fourier-transform on the time-series of fields, which we use to calculate fluxes as functions of frequency, $\Phi(\omega) = \frac{1}{2}\mathrm{Re}\{\int \mathbf{E}^*(\mathbf{r},\omega) \times \mathbf{H}(\mathbf{r},\omega) \cdot \mathrm{d}\mathbf{S}\}$. We run the simulation once with the slab in place, and again with vacuum only. To calculate reflectance, we know that $\mathbf{E}_{slab} = \mathbf{E}_{vac} + \mathbf{E}_{ref}$ is true above the slab (i.e. between the source and the slab), with $\mathbf{E}_{ref}$ being the field due to reflection. The reflectance is given by

$$R(\omega) \equiv \frac{\Phi_{ref}}{\Phi_{vac}} = \frac{-\frac{1}{2}\mathrm{Re}\{\int_{A_1} [\mathbf{E}_{slab}(\mathbf{r},\omega) - \mathbf{E}_{vac}(\mathbf{r},\omega)]^* \times [\mathbf{H}_{slab}(\mathbf{r},\omega) - \mathbf{H}_{vac}(\mathbf{r},\omega)] \cdot \mathrm{d}\mathbf{S}\}}{\frac{1}{2}\mathrm{Re}\{\int_{A_1} \mathbf{E}^*_{vac}(\mathbf{r},\omega) \times \mathbf{H}_{vac}(\mathbf{r},\omega) \cdot \mathrm{d}\mathbf{S}\}}$$

where A_1 is the flux plane corresponding to '1', and the minus sign in the numerator is there to make the reflected flux positive. This expression can be shown to simplify, in air, to $R(\omega) = [\Phi_1^{vac}(\omega) - \Phi_1^{slab}(\omega)]/\Phi_1^{vac}(\omega)$ where the flux plane closer to the light source is '1', and the flux plane further from the light source is '2'. (One can show that the numerator becomes $\Phi_1^{vac}(\omega) - \Phi_1^{slab}(\omega) + \frac{1}{2}\mathrm{Re}\{\int_{A_1} (\mathbf{E}^*_{vac} \times \mathbf{H}_{ref} - \mathbf{H}_{vac} \times \mathbf{E}^*_{ref}) \cdot \mathrm{d}\mathbf{S}\}$ but the cross term vanishes for incoming and outgoing plane waves in vacuum, for which $\mathbf{E}$ and $\mathbf{H}$ are proportional.) Similarly, the transmittance is given by $T(\omega) = \Phi_2^{slab}(\omega)/\Phi_2^{vac}(\omega)$ and the absorbance is simply $A(\omega) = 1 - R(\omega) - T(\omega)$. This way,

we obtain reflectance, transmittance and absorbance spectra for PhC slabs.

We incorporate absorption into our simulations by means of the Drude model, according to the following equation:

$$\epsilon(\omega) = \epsilon_\infty + \frac{4\pi\sigma}{(\omega_0^2 - \omega^2 - i\gamma\omega)} \tag{6.15}$$

where ϵ_∞, γ, ω_0 and σ are input parameters. In our case, we are concerned with metals, for which $\omega_0 = 0$.

For emittance calculations, we use the same setup except that we do not have a source plane. We include the random term ($\mathbf{K}$) in our updating of the polarization (see Eq. (6.2)), and we monitor the fluxes passing through the same two flux planes. We repeat this many times, and then perform an average of the fluxes. Averaging reduces the size of the fluctuations. The averaged fluxes are then converted to emittance by multiplying by the same constant conversion factor that exists between the absorbance and the fluxes in the case of the 1D uniform slab, for which emittance and absorbance are known to be equal, analytically.

A note about time averaging and ensemble averaging is appropriate here. According to the ergodic theorem, time averages and ensemble averages are equivalent in the limit of long time and large ensemble. However, when a discrete Fourier transform (DFT) is involved, the situation is somewhat subtle. In the FDTD algorithm that we use, the simulation is run for a discrete number of time steps N, after which a DFT is taken over the time series of fields $\mathbf{E}(t)$ and $\mathbf{H}(t)$, producing fields as functions of frequency $\mathbf{E}(\omega)$ and $\mathbf{H}(\omega)$. The frequency resolution ($\Delta\omega$) of the resulting DFT-produced spectrum is inversely proportional to the number of time steps for which the simulation is run: $\Delta\omega \sim 1/N$. Thus, the net effect of increasing the length of the run is to increase the frequency resolution of the spectrum. However, the time series of fields (and therefore its true, continuous Fourier transform) follows a stochastic process, which consists, in general, of a background drift combined with random fluctuations (distributed according to the probability density function in Eq. (6.12)). It is well known that stochastic processes, while continuous, are not differentiable

anywhere, i.e. they are infinitely 'wiggly'. This means that as we increase N and thus frequency resolution, all we are doing is resolving the fluctuations at a finer and finer level of detail, i.e. increasing N does nothing to reduce the magnitude of the fluctuations. On the other hand, performing a larger number of such runs and then taking the ensemble average *does* reduce the magnitude of those fluctuations, and we get much better convergence. Therefore, it is only necessary to make N large enough to achieve a desired frequency resolution. Once that resolution is reached, computational power is better spent performing more ensemble runs. We see this quite clearly in Figs. 6-4 and 6-6, both of which are averaged over an ensemble of 40 runs. Runs in Fig. 6-4 are ten times as long as runs in Fig. 6-6. Notice that the magnitudes of the fluctuations are comparable in the two figures, but the stochastic process is resolved at a much finer level of detail in Fig. 6-4, due to the higher frequency resolution that accompanies longer run times.

6.4 2D-periodic array of rods

The first system we consider is a 2D-periodic array of metal rods in air. Because of the existence of a mirror plane perpendicular to the y-direction, modes of the system can be divided into TM modes (with components E_y, H_x, H_z), which are odd under reflection, and TE modes (with components H_y, E_x, E_z), which are even under reflection. This separation of modes into TM and TE modes can be performed for all 2D-periodic systems with a mirror plane in the third dimension[31], and consequently, we can reap the benefits of this separation by considering the two types of modes independently.

We focus our attention on TM modes for which the magnetic field is transverse and the electric field is perpendicular to the 2D-plane of rods. (Physical behavior for TE modes is closely analogous.) For these modes, the electric field points in the direction of the axes of the rods, and so we need only consider light with electric field polarized in the y-direction. This is true for both absorbance and emission calculations. For absorbance, we illuminate the slab with y-polarized light; for emission, we allow only

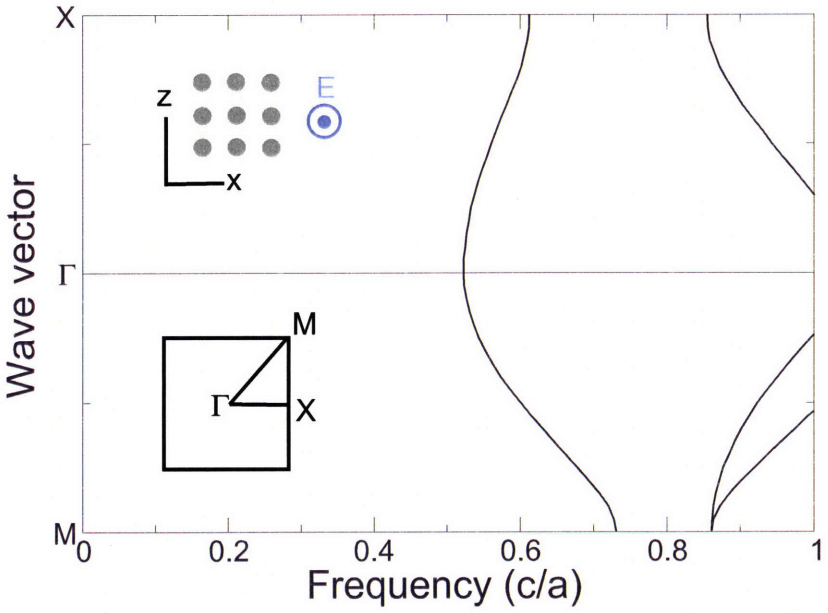

Figure 6-1: (Color) Bandstructure for a 2D-periodic array of perfect metal rods of radius $0.2a$. We show bands along Γ-X and Γ-M. The resolution is 40 grid points per a. We consider only TM modes, for which the electric field is polarized along the axes of the rods. We notice large band gaps in the system where light is forbidden from propagating, specifically from 0 to $0.52c/a$ and from $0.72c/a$ to $0.86c/a$.

thermal fluctuations ($\mathbf{K}$) in the y-direction.

We start by calculating the bandstructure for such a system of perfect metal rods of radius $0.2a$, where a is the lattice constant, as shown in Fig. 6-1. We use a resolution of 40 grid points per a, which is sufficient for a system with this level of spatial complexity. We plot the bands from Γ-X and from Γ-M in the first Brillouin zone. We see clearly the existence of a large photonic band gap from 0 to $0.52c/a$, and also from $0.72c/a$ to $0.86c/a$. This gives us a good guide with which to interpret the absorbance/emissivity spectra that we present next.

In Fig. 6-2, we compare the absorption and thermal emission spectra from a 2D-periodic slab of metal rods for TM modes. Absorbance was calculated with normally incident and outgoing waves. Notice that for these absorbance and emittance calcu-

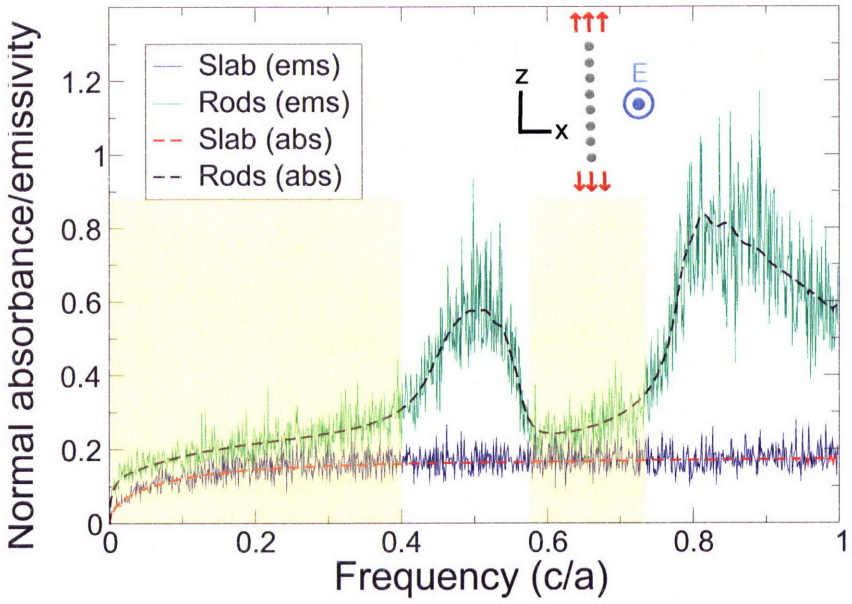

Figure 6-2: (Color) Comparison between absorption and thermal emission (averaged over 40 runs) from a 2D-periodic PhC slab of metal rods and a uniform slab, for TM modes at normal incidence. For the slab of rods, we use a long computational cell of 1x8 rods. For the metal, we use the Drude model with parameters $\epsilon_\infty = 1$, $\gamma = 0.3(2\pi c/a)$, $4\pi\sigma = 10(4\pi^2 c^2/a^2)$. We see good agreement between the emissivity (green and blue solid lines) and the absorptivity (black and red dashed lines). We notice also that the emissivity of a 2D slab of rods exceeds that of a uniform slab at all frequencies. The greatest enhancement comes from the non-gapped regions, where the enhancement can be as high as a factor of 4. Translucent yellow shading indicates regions of pseudogap for such a slab of imperfect metal rods, inferred from the absorption/emission spectrum.

lations, we used a *slab* of *imperfect* metal rods, i.e. ones that have absorptive losses. This is an important point because a perfect metal absorbs nothing and therefore emits nothing. Thus, we cannot directly compare Figs. 6-1 and 6-2 since the bandstructure in Fig. 6-1 was calculated for an *infinitely large* array of *perfect* metal rods. However, the bandstructure does give us a very good guide with which to interpret the emission spectra. In Fig. 6-2, we see high absorption/emission in the frequency ranges $0.4 - 0.6c/a$ and $0.8 - 1c/a$, from which we can infer that the band gaps are located in frequency ranges $0 - 0.4c/a$ and $0.6 - 0.8c/a$, approximately. We indicate these regions with a translucent yellow shading. We expect low absorption for band gap regions because the light is forbidden from propagating in the bulk of the photonic crystal, but we expect high absorption for non-gapped regions (i.e. regions with bands) because the light is able to penetrate the bulk of the system and be absorbed by the material.

We see excellent agreement between emissivity and absorbance, as predicted by Kirchhoff's law. There are a couple of interesting points worth mentioning: (i) the PhC slab emits more than the uniform slab at every frequency between 0 and 1 (we will explain this in the next section), and (ii) the fluctuations in emissivity are proportional to emissivity itself, as expected according to the discussion in Section 6.2.4.

6.5 3D-periodic woodpile structure

The first 3D-periodic structure we consider is the woodpile[74]. Pioneering work on thermal emission and the nature of the band gap for this structure was done by Lin *et al.*[44, 41, 22, 45, 42, 46]. We choose this particular structure because of the absence of linear bands at frequencies close to zero and the existence of a cut-off at $0.4c/a$ (there is a band gap in range $0 - 0.4c/a$). As a result, the structure behaves like a metal at low frequencies, with $\omega_p \approx 0.4c/a$.

The structure is made of metal rods with square cross section of width $0.25a$ arranged so that the rods are orthogonal to each other in adjacent layers. These

layers follow an ABCD pattern, such that C is the same as A shifted by half a lattice constant, and the same is true for D and B (B is the same as A rotated by 90 degrees). It turns out that such a structure can be described by a body-centered cubic lattice whose basis consists of two rods, one on top of the other, forming a 'plus' pattern. (One can also describe it as a stretched face-centered cubic lattice with a 'cross' for a basis, but the ratio of the z-length to the x- or y- length of the unit cell would be different, leading to an effectively orthorhombic lattice.)

In a general 3D-periodic system, there are no mirror planes of symmetry that would allow us to separate the modes into TM and TE modes. This means that it is not possible, in general, to excite perpendicular and transverse polarizations separately; the different polarizations are coupled together. Therefore, it is necessary to use all three directions (x, y and z) for polarizations in our simulations: all three must also be turned on for absorbance and for emittance calculations.

Fig. 6-3 shows the bandstructure for a 3D-periodic woodpile structure of perfect metal rods of width $0.25a$ and square cross section. We plot the bands from Γ-X and Γ-Z, since the Z-direction is distinct from the X-direction as a result of the basis of rods (though in the body-centered cubic *lattice*, they are equivalent directions). We see that there is a photonic band gap in the region $0 - 0.42c/a$. Above $0.42c/a$, there are bands which permit propagation of light through the photonic crystal.

In Fig. 6-4, we see a comparison between emissivity and absorptivity of the 3D-periodic woodpile structure as a function of frequency. The jagged lines (green and blue) correspond to emissivity, while the dashed lines (black and red) correspond to absorptivity. We show absorptivity and emissivity spectra for both the woodpile and the uniform slab. The agreement is excellent. Furthermore, we note that the emissivity of the woodpile structure exceeds that of the uniform slab at all frequencies, but especially at frequencies above the photonic band gap of the system. (We indicate the pseudogap for the metallic woodpile slab with a translucent yellow color.)

These observations can be explained by considering the structure as being equivalent to a uniform metal slab, with a plasmon frequency ($\omega_p \equiv \sqrt{4\pi\sigma}$) equal to the upper bound of the band gap. In such a situation, we can derive expressions for the

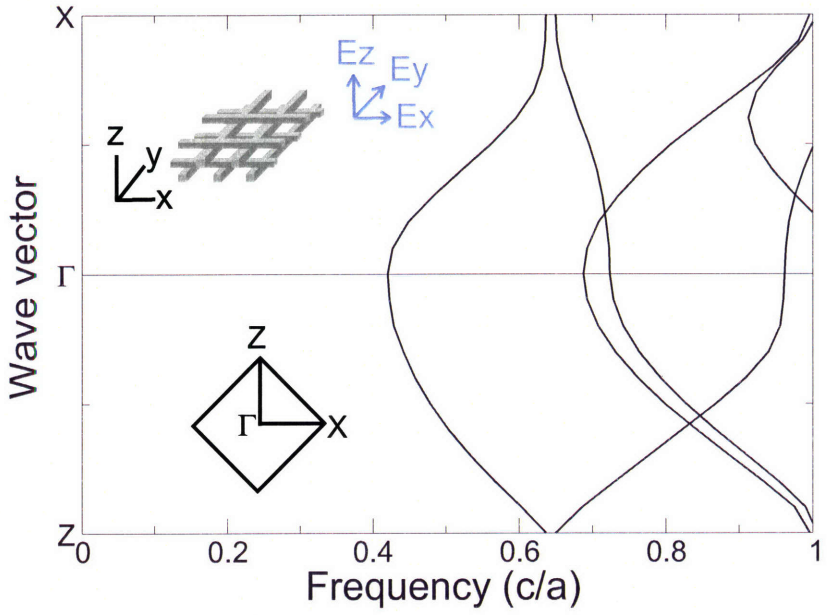

Figure 6-3: (Color) Bandstructure for a 3D-periodic woodpile structure made of perfect metal rods with square cross section of width $0.25a$. We show bands along Γ-X and Γ-Z. The resolution is 30 grid points per a. We consider modes with all polarizations. We notice a large band gap in the system where light is forbidden from propagating, specifically from 0 to $0.42c/a$.

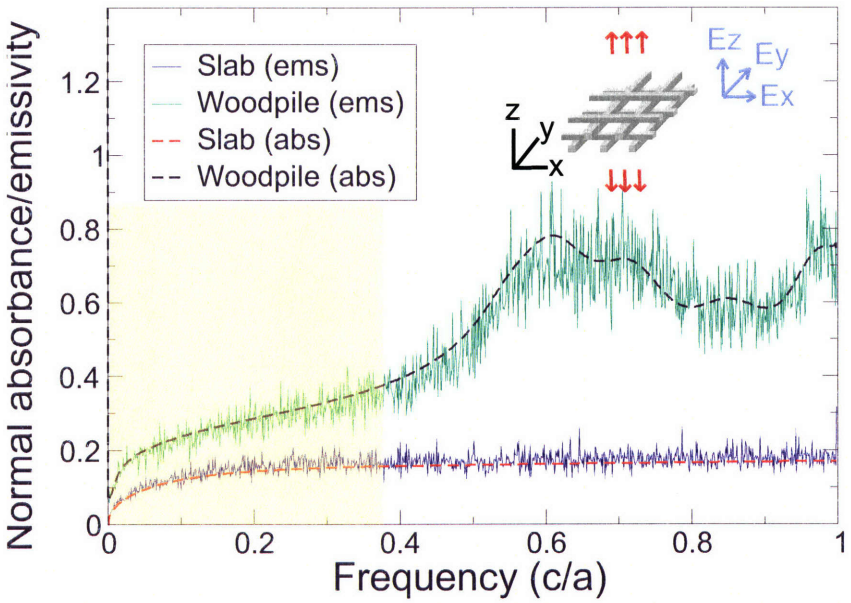

Figure 6-4: (Color) Comparison between absorption and thermal emission (averaged over 40 runs) from a slab of 3D-periodic woodpile made of metal rods, at normal incidence. We use a long computational cell with two unit cells of the woodpile structure in the z-direction. For the metal, we use the Drude model with parameters $\epsilon_\infty = 1$, $\gamma = 0.3(2\pi c/a)$, $4\pi\sigma = 10(4\pi^2 c^2/a^2)$. The frequency resolution is $0.001c/a$. We see good agreement between the emissivity (green and blue solid lines) and the absorptivity (black and red dashed lines). We notice also that the emission of the woodpile structure exceeds that of a uniform slab at all frequencies. The greatest enhancement comes from the non-gapped region above $0.4c/a$, where the enhancement can be as high as a factor of 4. Translucent yellow shading indicates regions of pseudogap for such a woodpile slab structure made of imperfect metal rods, inferred from the absorption/emission spectrum.

absorbance of the slab in two regimes: $\omega \ll \gamma \ll \omega_p$ and $\gamma \ll \omega \ll \omega_p$. This we do by calculating the reflectance using $R = [(n-1)^2 + k^2]/[(n+1)^2 + k^2]$ where n and k are the real and imaginary parts of the refractive index, defined by $\epsilon = (n + ik)^2$, and ϵ is the Drude dielectric function. Once we have the reflectance, we can obtain the absorbance by $A = 1 - R$. There is no transmission because the thickness of the slab is much greater than the penetration depth of the structure. If we perform this calculation for A in the low frequency regime, such that $\omega \ll \gamma \ll \omega_p$, we find that $A \approx \sqrt{8\omega\gamma}/\omega_p$. This explains the square-root dependence on frequency at extremely low frequencies. For the intermediate frequency regime, described by $\gamma \ll \omega \ll \omega_p$, we find that $A \approx 2\gamma/\omega_p$, which is independent of frequency. This explains the 'plateau' region of the absorption spectrum, where frequency dependence is almost flat. Finally, we note that the effective penetration depth of the photonic crystal slab is larger than that of the uniform metal slab, because the photonic crystal contains both metal and air while the uniform slab contains only metal. A larger penetration depth corresponds to a smaller effective ω_p (since penetration depth goes as $1/\omega_p$). Therefore, we expect a larger absorbance for the photonic crystal slab than the uniform metal slab in both the low and intermediate frequency regimes, and this is indeed what we observe.

Above the band gap, the photonic crystal has bands which allow light to propagate through the bulk of the structure. Now, light emitted from deep inside the structure can escape and contribute to the emissivity of the crystal. This explains the significant enhancement of emission over that from a uniform slab at frequencies above that of the pseudogap region. The emissivity of a uniform slab is limited to contributions from within about one penetration depth of the surface of the metal; light emitted from the bulk cannot escape because there are no propagating modes available to transport the light to the surface. Emissive contributions from the bulk of the structure are the reason that the emissivity from the non-gapped region of a photonic crystal slab is significantly higher than that from a uniform metal slab.

6.6 3D-periodic metallodielectric structure

The next structure we consider is a 3D-periodic metallodielectric structure made of metal spheres embedded in a Teflon background ($\epsilon = 2.1$), as studied by Fan, Villeneuve and Joannopoulos[20]. In direct contrast to the woodpile structure investigated in the previous section, this metallodielectric structure *does* have linear bands at low frequencies. While the woodpile exhibited metallic behavior at low frequencies, here we expect to see uniform dielectric behavior in that same frequency range. Whereas the woodpile structure had a band gap from 0 to $0.42c/a$, the metallodielectric structure has propagating bands for all frequencies except for a small gap from $0.54c/a$ to $0.63c/a$. We will see dramatic differences between the emissivity of this structure and that of the woodpile.

The bandstructure of this metallodielectric structure is shown in Fig. 6-5. The metal spheres have radius $0.177a$ (where a is the lattice constant) and are arranged in a diamond structure. We show the bands from Γ-X and Γ-L. The structure has a complete band gap between 0.54 and $0.63c/a$.

Fig. 6-6 shows the results of comparing the absorptivity spectrum with the emissivity, calculated for a slab of the 3D-periodic metallodielectric structure using stochastic electrodynamics. Once again, there is good agreement between emissivity and absorptivity. This time, we used a lower frequency resolution ($\Delta\omega = 0.01c/a$) in order to reduce computation time. It is clear that the emission spectra are smoother here than in Fig. 6-4, but notice that the size of the emissivity fluctuations (vertical fluctuations on the graph) are comparable to those in Fig. 6-4. This is because in both Fig. 6-4 and Fig. 6-6, the emissivity spectra were averaged over 40 runs, and, as we have already observed, the only way to reduce the size of the thermal fluctuations and increase convergence is to average over a larger ensemble of runs.

We notice that for a large range of frequencies ($\sim 0.4-1.0c/a$) the emissivity of the photonic crystal far exceeds that of the uniform metal slab. This we already explained in the previous section in terms of emissive contributions from the bulk of the photonic crystal being allowed to escape because of the existence of propagating bands at those

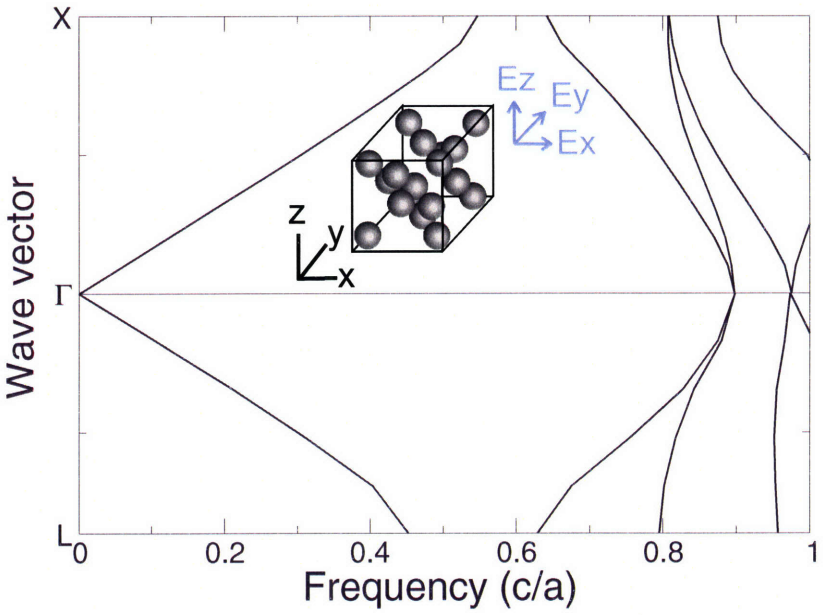

Figure 6-5: (Color) Bandstructure for a 3D-periodic metallodielectric structure made of perfect metal spheres of radius $0.177a$ in a background of Teflon ($\epsilon = 2.1$). We show bands along Γ-X and Γ-L. The resolution is 32 grid points per a. We consider modes with all polarizations. We notice a complete band gap in the system where light is forbidden from propagating, specifically from $0.54c/a$ to $0.63c/a$.

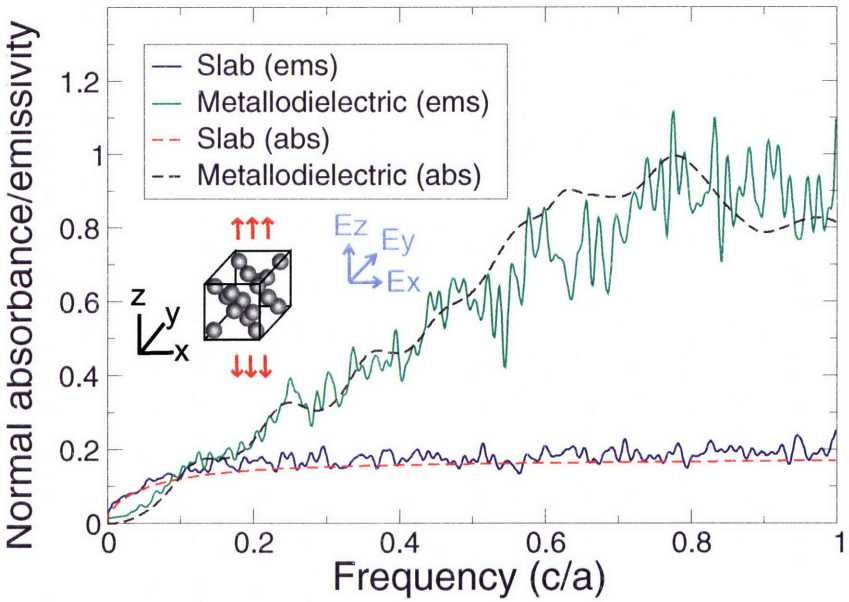

Figure 6-6: (Color) Comparison between absorption and thermal emission (averaged over 40 runs) from a slab of 3D-periodic metallodielectric structure made of metal spheres in a Teflon background, at normal incidence. We use a long computational cell with two unit cells of the metallodielectric structure in the z-direction. For the metal, we used the Drude model with parameters $\epsilon_\infty = 1$, $\gamma = 0.3(2\pi c/a)$, $4\pi\sigma = 10(4\pi^2 c^2/a^2)$. Here, we use a lower frequency resolution of $0.01c/a$ in order to decrease the duration of each run. We see good agreement between the emissivity (green and blue solid lines) and the absorptivity (black and red dashed lines). We notice also that the emission of the metallodielectric structure exceeds that of a uniform slab at all frequencies above $0.1c/a$. The greatest enhancement comes from the non-gapped region around $0.8c/a$, where the enhancement can be as high as a factor of 6. Note that the emissivity in that region is close to unity. Note also that the decreased run time leads to lower frequency resolution, as evidenced by the smoother spectrum. However, the size of the fluctuations remains unchanged (compare with Fig. 6-4), since is determined by the number of runs used in ensemble-averaging.

frequencies. The gapped region in this structure is so narrow $(0.54 - 0.63c/a)$ that the dip in emissivity one would expect to see in that region is not noticeable. What is interesting is that for frequencies below $0.1c/a$, the emissivity of the photonic crystal is actually *lower* than that of the uniform slab. This requires some explanation.

At low frequencies, the photonic crystal behaves effectively like a uniform dielectric. We can see this from the bandstructure, which shows roughly linear bands in the region $0 - 0.4c/a$. Such uniform dielectric behavior can be modeled by the Drude dielectric function with an oscillator frequency that is much higher than the frequency regime we are interested in, i.e. we are working in the low-loss, dielectric-like regime given by $\omega \ll \gamma \ll \omega_0$. In this regime, the imaginary part of the dielectric function (see Eq. (6.6)), which is given by $\mathrm{Im}(\epsilon) = 4\pi\sigma\gamma\omega/[(\omega_0^2 - \omega^2)^2 + \gamma^2\omega^2]$, is approximately linear in ω. The a.c. conductivity of the structure is given by $\omega\epsilon_0\mathrm{Im}(\epsilon)$, which goes as ω^2. Thus, the absorbance of the system, which is proportional to the integral of the a.c. conductivity over the volume of the structure, scales as ω^2 in the low frequency regime. This is precisely what we see in Fig. 6-6, and explains why the emissivity of the photonic crystal slab is lower than that for a uniform metal slab for $\omega \to 0$.

As Figs. 6-4 and 6-6 demonstrate, we have successfully verified Kirchhoff's law numerically for two very different 3D-periodic photonic crystal structures.

6.7 Effect of surface termination

One may wonder whether details of the absorption and emission spectra of a structure are affected by the surface termination one chooses. By surface termination, we refer to the plane in the periodic structure at which we terminate the PhC slab. Our choice of this termination may well have an effect on the surface modes that can be excited by incident light. The absorption/reflection/transmission caused by the bulk of the structure remain unchanged, because we keep the same thickness of bulk structure in the PhC slab. We can imagine a window as wide as the thickness of the slab, moving downwards in the z-direction across such a periodic structure of infinite extent; as the window moves, it reveals a slab of material with a different surface termination.

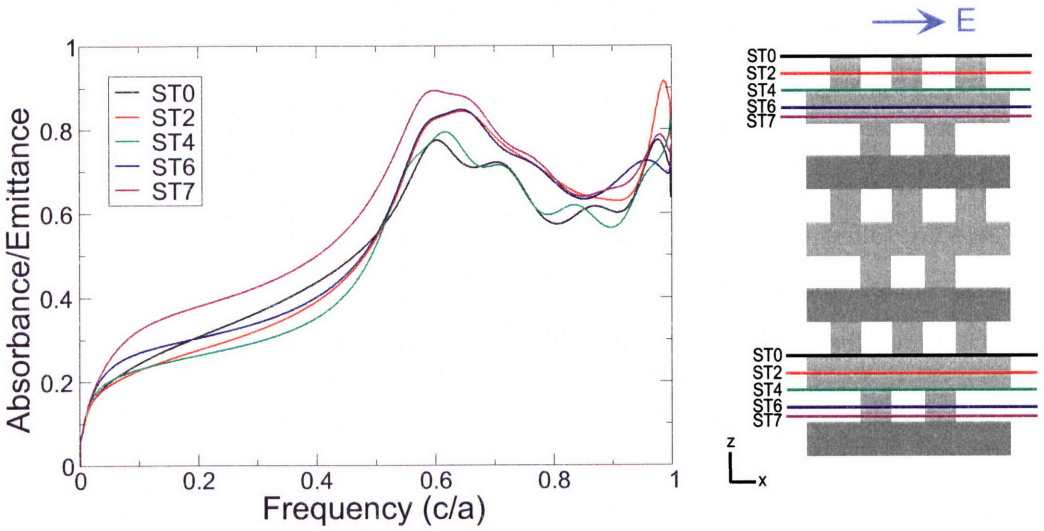

Figure 6-7: (Color) Absorbance/emittance spectrum for a woodpile PhC slab made of imperfect metal rods for 5 different surface terminations. Light polarized along x is incident from the top of the cell. We use a long computational cell with two unit cells of the woodpile structure in the z-direction. For the metal, we used the Drude model with parameters $\epsilon_\infty = 1$, $\gamma = 0.3(2\pi c/a)$, $4\pi\sigma = 10(4\pi^2 c^2/a^2)$. The inset is a schematic (lengths not to scale) indicating the surface terminations chosen. For all calculations, we keep the thickness of the slab to about two unit cells, so changing the surface termination amounts to shifting the structure within a two-unit-cell-thick slab 'mask' which remains stationary as the structure is shifted, such that the total amount of material is kept constant. For instance, for 'ST0', the structure used is that between the two black lines, while for 'ST6', it is what lies between the two blue lines. 'ST7' appears to have the highest absorption/emission at all frequencies.

Fig. 6-7 shows how absorbance/emittance of x-polarized light changes with surface termination in the case of the 3D-periodic woodpile slab structure. We indicate in the inset the different ways in which the slab structure can be 'terminated'. The number following the letters 'ST' indicate the position of the surface termination plane in relation to the structure. For example, 'ST2' is halfway down the first layer of blocks, and 'ST7' is three-quarters of the way down the second layer of blocks. It is remarkable how big a difference in absorption/emission can arise as a result of changing the surface termination. For example, 'ST7' seems to lead to the highest absorbance at all frequencies investigated, whereas 'ST4' has lower absorbance than almost all the other terminations.

In the band gap region ($0 - 0.4c/a$), the light incident from the top of the cell is only able to penetrate the top surface; it is forbidden from propagating through the bulk of the crystal. Effectively, the incident light sees only the top surface, and any absorption/emission in the structure takes place near that surface. Thus, the absorption/emission spectra within the band gap are more sensitive to surface termination than that lying above the gap, for which absorption and emission are dominated by the bulk of the structure. This explains why the curves are more distinct in the band gap region than above it.

We notice also that above the band gap, the red and blue curves overlap significantly, as do the black and green curves. This requires some explanation.

We see from the schematic in Fig. 6-7 that the red and blue ('ST2' and 'ST6') terminations are very similar, the only difference being that the blue structure is the same as the red structure rotated by 90 degrees about the z-axis. In fact, such a rotation maps the red onto the blue, and vice versa. In terms of surface terminations, they are the same: the termination that red has at the top of the slab is what blue has at the bottom, so that what the red structure emits from the top surface is what the blue structure emits from the bottom surface. Thus, we expect to see very similar absorbance/emittance spectra for the red and blue structures above the gap, and this is indeed what we see: the red and blue curves overlap significantly at frequencies above $0.5c/a$. The small differences comes from the fact that in the

absorption calculation in Fig. 6-7, the light is incident from the top; this means that the top surface has a greater contribution to absorption than the bottom surface (even though both surfaces contribute because the bulk is transmitting above the gap), and causes the spectra to be polarization-sensitive, since the top surfaces of the red and blue structures are different.

At first glance, one may be tempted to think that the black and green ('ST0' and 'ST4') terminations are related to each other in the same way. However, that is not the case: a 90 degree rotation will *not* map the black structure onto the green structure. Thus, as far as x-polarized light is concerned, they are irreducibly different surface terminations, in that one is orthogonal to the other. The curves show this clearly: the black and green curves are quite close together, but not as close together as the red and blue curves. And once again, the difference is most pronounced in the band gap region, where surface contributions dominate.

This information can be very useful in tailoring thermal emission properties of such woodpile slab structures, and more generally, photonic crystal slabs. By choosing a favorable surface termination, we can get over 20% enhancement in absorption/emission in certain frequency ranges over a randomly chosen surface termination.

6.8 Conclusion

We outlined in detail the theory and implementation of stochastic electrodynamics following the Langevin approach and performed direct calculations of thermal emission for 2D- and 3D-periodic photonic crystal slabs via an FDTD algorithm. We demonstrated that emissivity and absorptivity are equal for a 2D-periodic structure of metal rods, a 3D-periodic woodpile structure and a 3D-periodic metallodielectric structure, by showing that such photonic crystal systems emit as much radiation as they absorb, for every frequency, up to statistical fluctuations. We also studied the effect of surface termination on absorption and emission spectra from these systems, and found that subtle changes in surface termination can have significant effects on emissivity. In terms of applications, the stochastic electrodynamic framework de-

scribed in this work has many potential uses, including direct calculations of thermal emission in non-equilibrium systems, and systems with short thermalization times. One can also use this methodology to verify Kirchhoff's law numerically for finite-sized (non-slab) thermal objects. The results on surface termination can be used to enhance thermal emission for many such photonic crystal systems.

Chapter 7

Conclusion

In this thesis, we studied point defect geometries in inverted opal photonic crystals that can be fabricated by means of colloidal self-assembly, and discovered a way of introducing a triply degenerate defect mode into the band gap. We demonstrated a physically intuitive framework within which the thermal behavior of 1D- and 2D-periodic metallic photonic crystal slabs can be understood. We found a few structures that have strong emission peaks with high emissivity that can be used as building blocks for designing high-emission photonic crystal structures. These peaks can be shifted at will by changing the lattice constant of the structure or by changing the operating temperature. We developed an analytic model that allows us to understand how the significant enhancement of thermal emission via Q-matching, which has been possible in 1D systems only, can be extended to 2D systems by means of Fano resonances. Properties of these spectra can be controlled by changing the geometrical parameters of the photonic crystals. We described the theory and implementation of stochastic electrodynamics following the Langevin approach and performed direct calculations of thermal emission for 2D- and 3D-periodic photonic crystal slabs via an FDTD algorithm. We showed that emissivity and absorptivity are equal for a 2D-periodic structure of metal rods, a 3D-periodic woodpile structure and a 3D-periodic metallodielectric structure, up to statistical fluctuations. We also studied the effect of surface termination on absorption and emission spectra from these systems. In summary, this thesis has proposed a new class of point defects, provided a physi-

cally intuitive framework for understanding thermal phenomena in photonic crystals, suggested structures for enhancing thermal emission, explained anomalous thermal behavior related to Fano resonances, and demonstrated how a direct thermal emission calculation can be done for 3D-periodic photonic crystals.

Although we studied a wide range of phenomena, this thesis is far from being a complete catalog of thermal effects or point defect geometries in photonic crystal systems. There are many open questions that can be addressed and new directions in which this research can be taken. For instance, one could investigate other classes of defects, whether they be of the point or line variety, in systems subject to fabrication constraints. Such work is important because the cost of fabrication remains a serious roadblock to widespread adoption of this versatile technology, and a defective understanding of the physics can be costly. One could optimize the designs suggested in this thesis, and perhaps propose new ones, for enhancing thermal emission in certain frequency ranges. In particular, it would be interesting to study 3D-periodic photonic crystal geometries that enhance thermal radiation. More work could be done on Fano resonances and the anomalous thermal behavior they exhibit. Our ability to perform direct thermal emission calculations for general photonic crystal systems opens up exciting possibilities for non-equilibrium systems[80, 5], finite-sized objects, and non-linear materials. Kirchhoff's law comes with a caveat for non-linear or fluorescent materials: under such circumstances, light can be absorbed at one frequency and emitted at another, so that emissivity and absorptivity are not equal for particular frequencies, but *are* equal when integrated over all frequencies. It would be intriguing to simulate such systems numerically with the stochastic electrodynamic framework described, and to incorporate non-linear effects such as the Pockels or the Kerr effects that can lead to apparent 'violations' of Kirchhoff's law. The goal of this work is to present the basic physical principles that underlie many of these interesting phenomena in a clear and illuminating manner, and to act as a springboard for further study. We hope that this thesis will ignite the interest of the reader in these topics. Thermal emission from photonic crystals is a hotbed of interdisciplinary research, and people working in this radiant field can look forward to a bright future.

Bibliography

[1] G. S. Arnold. Absorptivity of several metals at 10.6 μm: empirical expressions for the temperature dependence computed from drude theory. *Appl. Opt.*, 23:1434, 1984.

[2] J. Arriaga, A. J. Ward, and J. B. Pendry. Order-n photonic band structures for metals and other dispersive materials. *Phys. Rev. B*, 59:1874, 1999.

[3] N. W. Ashcroft and N. D. Mermin. *Solid State Physics.* Harcourt, 1976.

[4] V. N. Astratov et al. Interplay of order and disorder in the optical properties of opal photonic crystals. *Phys. Rev. B*, 66:165215, 2002.

[5] H. P. Baltes. On the validity of kirchhoff's law of heat radiation for a body in a nonequilibrium environment. *Progress in Optics*, XIII, 1976.

[6] A. Blanco et al. Large-scale synthesis of a silicon photonic crystal with a complete three-dimensional bandgap near 1.5 micrometres. *Nature*, 405:437–439, 2000.

[7] M. Boroditsky, R. Vrijen, T. F. Krauss, R. Coccioli, R. Bhat, and E. Yablonovitch. Spontaneous emission extraction and purcell enhancement from thin-film 2-d photonic crystals. *J. Lightwave Technol.*, 17:1096, 1999.

[8] F. Bresson et al. Simplified sedimentation process for 3d photonic thick layers/bulk crystals with a stop-band in the visible range. *Appl. Surf. Sci.*, 217:281–288, 2003.

[9] K. Busch and S. John. Photonic band gap formation in certain self-organizing systems. *Phys. Rev. E*, 58:3896–3908, 1998.

[10] W. D. Callister. *Fundamentals of Materials Science and Engineering: An Interactive e-Text.* Wiley, 2000.

[11] I. Celanovic, D. Perreault, and J. Kassakian. Resonant-cavity enhanced thermal emission. *Phys. Rev. B*, 72:075127, 2005.

[12] D. L. C. Chan, E. Lidorikis, and J. D. Joannopoulos. Point defect geometries in inverted opal photonic crystals. *Phys. Rev. E*, 71:056602, 2005.

[13] D. Chub, D. Woldrof, A. Muelenberg, and R. DiMatteo. Semiconductor silicon as selective emitter. In *TPV Generation of Electricity 5th Conference, American Institute of Physics*, 2003.

[14] C. M. Cornelius and J. P. Dowling. Modification of planck blackbody radiation by photonic band-gap structures. *Phys. Rev. A*, 59:4736, 1999.

[15] A. R. Cowan, P. Paddon, V. Pacradouni, and J. F. Young. Resonant scattering and mode coupling in two-dimensional textured planar waveguides. *J. Opt. Soc. Am. A*, 18:1160, 2001.

[16] S. Enoch, J.-J. Simon, L. Escoubas, Z. Elalmy, F. Lemarquis, P. Torchio, and G. Albrand. Simple layer-by-layer photonic crystal for the control of thermal emission. *Appl. Phys. Lett.*, 86:261101, 2005.

[17] A. A. Erchak, D. J. Ripin, S. Fan, P. Rakich, J. D. Joannopoulos, E. P. Ippen, G. S. Petrich, and L. A. Kolodziejski. Enhanced coupling to vertical radiation using a two-dimensional photonic crystal in a semiconductor light-emitting diode. *Appl. Phys. Lett.*, 78:563, 2001.

[18] S. Fan. Sharp asymmetric line shapes in side-coupled waveguide-cavity systems. *Appl. Phys. Lett.*, 80:908, 2002.

[19] S. Fan and J. D. Joannopoulos. Analysis of guided resonances in photonic crystal slabs. *Phys. Rev. B*, 65:235112, 2002.

[20] S. Fan, P. R. Villeneuve, and J. D. Joannopoulos. Large omnidirectional band gaps in metallodielectric photonic crystals. *Phys. Rev. B*, 54:11245, 1996.

[21] S. Fan, P. R. Villeneuve, J. D. Joannopoulos, and H. A. Haus. Loss-induced on/off switching in a channel add/drop filter. *Phys. Rev. B*, 64:245302, 2001.

[22] J. G. Fleming, S. Y. Lin, I. El-Kady, R. Biswas, and K. M. Ho. All-metallic three-dimensional photonic crystals with a large infrared bandgap. *Nature*, 417:52, 2002.

[23] M. Florescu, H. Lee, A. J. Stimpson, and J. Dowling. Thermal emission and absorption of radiation in finite inverted-opal photonic crystals. *Phys. Rev. A*, 72:033821, 2005.

[24] G. Gilat and L. J. Raubenheimer. Accurate numerical method for calculating frequency-distribution functions in solids. *Phys. Rev.*, 144:390–395, 1966.

[25] J.-J. Greffet, R. Carminati, K. Joulain, J.-P. Mulet, S. Mainguy, and Y. Chen. Coherent emission of light by thermal sources. *Nature*, 416:61, 2002.

[26] J.-J. Greffet and M. Nieto-Vesperinas. Field theory for generalized bidirectional reflectivity: derivation of helmholtz's reciprocity principle and kirchhoff's law. *J. Opt. Soc. Am. A*, 15:2735, 1998.

[27] T. D. Happ, M. Kamp, and A. Forchel. Coupling of point-defect microcavities in two-dimensional photonic-crystal slabs. *J. Opt. Soc. Am. B*, 20:373–378, 2003.

[28] H. A. Haus. *Waves and Fields in Optoelectronics.* Prentice-Hall, 1984.

[29] E. Hecht. *Optics.* Addison-Wesley, 3rd edition, 1998.

[30] J. D. Joannopoulos. Self-assembly lights up. *Nature*, 414:257–258, 2001.

[31] J. D. Joannopoulos, R. D. Meade, and J. N. Winn. *Photonic Crystals: Molding the Flow of Light.* Princeton, 1995.

[32] J. D. Joannopoulos, P. R. Villeneuve, and S. Fan. Photonic crystals: putting a new twist on light. *Nature*, 386:143–149, 1997.

[33] S. John and K. Busch. Photonic bandgap formation and tunability in certain self-organizing systems. *J. Lightwave Technology*, 17:1931–1943, 1999.

[34] P. M. Johnson, A. F. Koenderink, and W. L. Vos. Ultrafast switching of photonic density of states in photonic crystals. *Phys. Rev. B*, 66:081102(R), 2002.

[35] S. G. Johnson and J. D. Joannopoulos. *Photonic Crystals: The Road from Theory to Practice.* Kluwer, 2002.

[36] C. Kittel. *Introduction to Solid State Physics.* Wiley, 7th edition, 1996.

[37] A. F. Koenderink, L. Bechger, H. P. Schriemer, A. Lagendijk, and W. L. Vos. Broadband fivefold reduction of vacuum fluctuations probed by dyes in photonic crystals. *Phys. Rev. Lett.*, 88:143903, 2002.

[38] M. Laroche, R. Carminati, and J.-J. Greffet. Coherent thermal antenna using a photonic crystal slab. *Phys. Rev. Lett.*, 96:123903, 2006.

[39] B. J. Lee, C. J. Fu, and Z. M. Zhang. Coherent thermal emission from one-dimensional photonic crystals. *Appl. Phys. Lett.*, 87:071904, 2005.

[40] B. Li et al. Photonic band gap in (pb,la)(zr,ti)o_3 inverse opals. *Appl. Phys. Lett.*, 82:3617, 2003.

[41] S.-Y. Lin, J. G. Fleming, E. Chow, J. Bur, K. K. Choi, and A. Goldberg. Enhancement and suppression of thermal emission by a three-dimensional photonic crystal. *Phys. Rev. B*, 62:R2243–R2246, 2000.

[42] S.-Y. Lin, J. G. Fleming, and I. El-Kady. Experimental observation of photonic-crystal emission near a photonic band edge. *Appl. Phys. Lett.*, 83:593, 2003.

[43] S.-Y. Lin, J. G. Fleming, and I. El-Kady. Three-dimensional photonic-crystal emission through thermal excitation. *Opt. Lett.*, 28:1909, 2003.

[44] S. Y. Lin, J. G. Fleming, D. L. Hetherington, B. K. Smith, R. Biswas, K. M. Ho, M. M. Sigalas, W. Zubrzycki, S. R. Kurtz, and J. Bur. A three-dimensional photonic crystal operating at infrared wavelengths. *Nature*, 394:251, 1998.

[45] S. Y. Lin, J. Moreno, and J. G. Fleming. Three-dimensional photonic-crystal emitter for thermal photovoltaic power generation. *Appl. Phys. Lett.*, 83:380, 2003.

[46] S.-Y. Lin, J. Moreno, and J. G. Fleming. Response to "comment on 'three-dimensional photonic-crystal emitter for thermal photovoltaic power generation"'. *Appl. Phys. Lett.*, 84:1999, 2004.

[47] J. R. Link and M. J. Sailor. Smart dust: Self-assembling, self-orienting photonic crystals of porous Si. *P. Natl. Acad. Sci. USA*, 100:10607–10610, 2003.

[48] C. Luo, A. Narayanaswamy, G. Chen, and J. D. Joannopoulos. Thermal radiation from photonic crystals: A direct calculation. *Phys. Rev. Lett.*, 93:213905, 2004.

[49] L. Martin-Moreno, F. J. Garcia-Vidal, and A. M. Somoza. Self-assembled triply periodic minimal surfaces as molds for photonic band gap materials. *Phys. Rev. Lett.*, 83:73–75, 1999.

[50] M. Meier, A. Mekis, A. Dodabalapur, A. Timko, R. E. Slusher, and J. D. Joannopoulos. Laser action from two-dimensional distributed feedback in photonic crystals. *Appl. Phys. Lett.*, 74:7, 1999.

[51] A. Mekis, A. Dodabalapur, R. E. Slusher, and J. D. Joannopoulos. Two-dimensional photonic crystal couplers for unidirectional light output. *Opt. Lett.*, 25:942, 2000.

[52] H. J. Monkhorst and J. D. Pack. Special points for brillouin-zone integrations. *Phys. Rev. B*, 13:5188–5192, 1976.

[53] B. A. Munk. *Frequency Selective Surfaces Theory and Design.* Wiley, New York, 2000.

[54] A. Narayanaswamy and G. Chen. Thermal emission control with one-dimensional metallodielectric photonic crystals. *Phys. Rev. B*, 70:125101, 2004.

[55] M. A. Ordal, R. J. Bell, Jr. R. W. Alexander, L. L. Long, and M. R. Querry. Optical properties of fourteen metals in the infrared and far infrared: Al, co, cu, au, fe, pb, mo, ni, pd, pt, ag, ti, v and w. *Appl. Opt.*, 24:4493, 1985.

[56] E. D. Palik. *Handbook of Optical Constants.* Academic Press, Inc., 1985.

[57] B. A. Parviz, D. Ryan, and G. M. Whitesides. Using self-assembly for the fabrication of nano-scale electronic and photonic devices. *IEEE T. Adv. Packaging*, 26:233–241, 2003.

[58] S. Peng and G. M. Morris. Resonant scattering from two-dimensional gratings. *J. Opt. Soc. Am. A*, 13:993, 1996.

[59] M. Planck. On the law of distribution of energy in the normal spectrum. *Annalen der Physik*, 4:553, 1901.

[60] R. D. Pradhan, J. A. Bloodgood, and G. H. Watson. Photonic band structure of bcc colloidal crystals. *Phys. Rev. B*, 55:9503–9507, 1999.

[61] M. U. Pralle, N. Moelders, M. P. McNeal, I. Puscasu, A. C. Greenwald, J. T. Daly, E. A. Johnson, T. George, D. S. Choi, I. El-Kady, and R. Biswas. Photonic crystal enhanced narrow-band infrared emitters. *Appl. Phys. Lett.*, 81:4685, 2002.

[62] M. H. Qi et al. A three-dimensional optical photonic crystal with designed point defects. *Nature*, 429:538–542, 2004.

[63] L. J. Raubenheimer and G. Gilat. Accurate numerical method of calculating frequency distribution functions in solids. ii. extension to hcp crystals. *Phys. Rev.*, 157:586–599, 1967.

[64] F. Reif. *Fundamentals of Statistical and Thermal Physics.* McGraw-Hill, 1965.

[65] O. E. Rogach et al. Self-organization of uniform silica globules into the three-dimensional superlattice of artificial opals. *Mat. Sci. Eng. B - Solid*, 64:64–67, 1999.

[66] S. M. Rytov. *Theory of Electric Fluctuations and Thermal Radiation.* Academy of Sciences Press, Moscow, Russia, english translation 1959 edition, 1953.

[67] Y. Saado, M. Golosovsky, D. Davidov, and A. Frenkel. Tunable photonic band gap in self-assembled clusters of floating magnetic particles. *Phys. Rev. B*, 66:195108, 2002.

[68] H. Sai, T. Kamikawa, Y. Kanamori, K. Hane, H. Yugami, and M. Yamaguchi. Thermophotovoltaic generation with microstructured tungsten selective emitters. In *Proceedings of the Sixth NREL Conference on Thermophotovoltaic Generation of Electricity*, pages 206–214, 2004.

[69] H. Sai, H. Yugami, Y. Akiyama, Y. Kanamori, and K. Hane. Spectral control of thermal emission by periodic microstructured surfaces in the near-infrared region. *J. Opt. Soc. Am. A*, 18:1471, 2001.

[70] M. Scalora, M. J. Bloemer, A. S. Pethel, J. P. Dowling, C. M. Bowden, and A. S. Manka. Transparent, metallo-dielectric, one-dimensional, photonic band-gap structures. *J. Appl. Phys.*, 83:2377, 1998.

[71] H. P. Schriemer, H. M. van Driel, A. F. Koenderink, and W. L. Vos. Modified spontaneous emission spectra of laser dye in inverse opal photonic crystals. *Phys. Rev. A*, 63:011801(R), 2000.

[72] M. Soljacic, M. Ibanescu, S. G. Johnson, Y. Fink, and J. D. Joannopoulos. Optimal bistable switching in nonlinear photonic crystals. *Phys. Rev. E*, 66:055601, 2002.

[73] Marin Soljacic, Elefterios Lidorikis, Lene Vestergaard Hau, and J. D. Joannopoulos. Enhancement of microcavity lifetimes using highly dispersive materials. *Phys. Rev. E*, 71:026602, 2005.

[74] H. S. Sözüer and J. P. Dowling. Photonic band calculations for woodpile structures. *J. Mod. Opt.*, 41:231, 1994.

[75] A. Taflove and S. C. Hagness. *Computational Electrodynamics: The Finite-Difference Time-Domain Method.* Artech House, Norwood, MA, 2000.

[76] Y. A. Vlasov, X.-Z. Bo, J. C. Sturm, and D. J. Norris. On-chip natural assembly of silicon photonic bandgap crystals. *Nature*, 414:289–293, 2001.

[77] Yu. A. Vlasov et al. Manifestation of intrinsic defects in optical properties of self-organized opal photonic crystals. *Phys. Rev. E*, 61:5784–5793, 2000.

[78] Z. Wang, C. T. Chan, W. Zhang, N. Ming, and P. Sheng. Three-dimensional self-assembly of metal nanoparticles: Possible photonic crystal with a complete gap below the plasma frequency. *Phys. Rev. B*, 64:113108, 2001.

[79] J. H. Weaver, C. G. Olson, and D. W. Lynch. Optical properties of crystalline tungsten. *Phys. Rev. B*, 12:1293, 1975.

[80] M. A. Weinstein. On the validity of kirchhoff's law for a freely radiating body. *Am. J. Phys.*, 28:123, 1960.

[81] Y. Xu, Y. Li, R. K. Lee, and A. Yariv. Scattering-theory analysis of waveguide-resonator coupling. *Phys. Rev. E*, 62:7389, 2000.

[82] E. Yablonovitch. Inhibited spontaneous emission in solid-state physics and electronics. *Phys. Rev. Lett.*, 58:2059, 1987.

[83] M. F. Yanik, S. Fan, and M. Soljacic. High-contrast all-optical bistable switching in photonic crystal microcavities. *Appl. Phys. Lett.*, 83:2739, 2003.

[84] M. F. Yanik, S. Fan, M. Soljacic, and J. D. Joannopoulos. All-optical transistor action with bistable switching in a photonic crystal cross-waveguide geometry. *Opt. Lett.*, 28:2506, 2003.

[85] V. Yannopapas, N. Stefanou, and A. Modinos. Effect of stacking faults on the optical properties of inverted opals. *Phys. Rev. Lett.*, 86:4811–4814, 2001.